Study on thin film fabrication process and electrode reaction analysis for high efficiency solid oxide fuel cell

Yoichiro Tsuji

目次

CHAPTER 1. GENERAL INTRODUCTION **5**

1.1 BACKGROUND 5

1.2 SOLID OXIDE FUEL CELLS 5

1.3 OXIDE ION DIFFUSION 6

1.3.1 Point defects *6*

1.3.2 Oxide ion diffusion *8*

1.4 ELECTROLYTE MATERIALS 8

1.4.1 Fluorite-structured electrolytes *9*

1.5 CATHODE MATERIALS 10

1.6 ELECTRODE REACTION MECHANISM 11

1.6.1 Elementary reaction on cathode reaction *12*

1.6.2 Rate determined step *12*

1.7 ISSUES FOR SOLID OXIDE FUEL CELLS 13

1.8 OUTLINE OF THE PRESENT THESIS 14

REFERENCES 16

CHAPTRE 2. ELECTRODEPOSITION OF THIN YTTRIA-STABILIZED ZIRCONIA LAYERS USING GLOW-DISCHARGE PLASMA **26**

2.1. INTRODUCTION 26

2.2. EXPERIMENT 27

2.2.1. Apparatus *27*

2.2.2. Deposition procedure *28*

2.2.3. Analytical procedures *28*

2.3. RESULTS 28

2.3.1. Deposition of thin film layers containing yttrium *28*

2.3.2 Characterization of deposited layer *29*

2.4. DISCUSSION 30

2.4.1. Probable model for the growth of YSZ layer *30*

2.4.2. Voltage loss through the dc circuit *32*

2.4.3. Current efficiency of oxide deposition *32*

2.4.4. Anodic reactions in the EVD process *32*

2.5. CONCLUSION 33

ACKKNOWLEDGMENTS 33

REFERENCES 33

CHAPTER 3. PREPARATION OF THIN YTTRIA-STABILIZED ZIRCONIA FILMS BY VAPOR-PHASE ELECTROLYTIC DEPOSITION 42

3.1. INTRODUCTION 42

3.2. EXPERIMENTAL 43

3.2.1. Materials *43*

3.2.2. Vapor-phase electrolytic deposition (VED) *43*

3.2.3. Measuring techniques *44*

3.3. RESULTS AND DISCUSSION 44

3.3.1. Preparation of YSZ thin films by the CVD process *44*

3.3.2. Preparation of YSZ thin films by the VED process *45*

3.4. CONCLUSION 46

ACKNOWLEDGEMENT 46

REFERENCES 46

CHAPTER 4. INVESTIGATION OF CATHODIC REACTION IN SOLID OXIDE FUEL CELLS BY OPERANDO X-RAY ABSORPTION SPECTROSCOPY **55**

4.1. INTRODUCTION 55

4.2. EXPERIMENTAL 56

4.2.1. Preparation of thin-film electrodes *56*

4.2.2. High temperature electrochemical operando XAS apparatus *56*

4.2.3. Operando XAS measurements *57*

4.3. RESULTS AND DISCUSSION 57

4.3.1. Operando XAS measurements *57*

4.3.2. Electrochemical reactions on LSC, LSCF, and LSM *58*

4.4. CONCLUSION 62

ACKNOWLEDGEMENT 62

REFERENCES 62

CHAPTER 5. SURFACE ANALYSIS OF LANTHANUM STRONTIUM COBALT OXIDES UNDER CATHODIC POLARIZATION AT HIGH TEMPERATURE THROUGH *OPERANDO* TOTAL-REFLECTION X-RAY ABSORPTION AND X-RAY FLUORESCENCE SPECTROSCOPY **85**

5.1. INTRODUCTION 85

5.2. EXPERIMENTAL 86

5.2.1. Sample preparation *86*

5.2.2. Electrochemical testing *87*

5.2.3. Operando XAS and XRF analysis *87*

5.3. RESULTS AND DISCUSSION 88

5.4. CONCLUSION 91

ACKNOWLEDGEMENT 91

REFERENCES 91

CHAPTER 6. GENERAL CONCLUSION 110

ACKNOWLEDGMENT 113

Chapter 1. General Introduction

1.1 Background

In recent years, environmental issues such as water and air pollution, acid rain, and greenhouse gas emissions have become major global issures. The most serious one is global warming caused by emissions of greenhouse gases (e.g., carbon dioxide, methane, and nitrous oxide). Carbon dioxide is one of the most influential greenhouse gases and its emissions come from fossil fuels such as coal, oil and natural gas [1]. To build a sustainable society, it is necessary to control the rate of global warming by reducing CO_2 emissions and finally bring it to substantially zero. For this reason, current power generation systems require technological development in terms of the following issues:

1) Highly efficient energy conversion systems
2) Lower cost and widely available renewable energy
3) Carbon dioxide storage and reuse

To meet these requirements, many researchers are studying new clean energy devices (e.g., lithium ion batteries, solar power generation, and fuel cells) [2-4]. In these devices, energy is generated by electrochemical reactions. Among them, fuel cells are attracting a great deal of attention as highly efficient power generation devices. A fuel cell consists of an electrical conductor as electrodes and a hydrogen or oxide ion conductor as an electrolyte. Fuel cells reduce emissions of carbon dioxide and other greenhouse gases because they can generate electricity from fuel in a vey efficient manner and output only water during power generation. Therefore, in this study, we describe research aimed at improving power generation efficiency of fuel cells.

1.2 Solid oxide fuel cells

There are several types of fuel cells: polymer electrolyte fuel cells (PEFCs), phosphoric acid fuel cells (PAFCs), molten carbonate fuel cells (MCFCs), solid oxide fuel cells (SOFCs), and alkaline fuel cells (AFCs). Among them, SOFCs have the highest power generation efficiency and various advantages such as fuel flexibility, high reliability, and simplicity of system. As a result, SOFC technology has attracted a great deal of attention for distributed power plants and has now begun to spread to household and industrial use as a cogeneration system that generates heat and electricity. SOFCs are the one of the most efficient devices invented to convert chemical fuels directly into electricity [5]. The exhaust heat from SOFCs can also be used to transform hydrocarbons into fuel [6-8]. This enables SOFC systems to perform energy conversions with high efficiency.

The basic ideas and materials for SOFCs were proposed by Nernst et al. [9,10] at the end of the 19th century. However, significant progress has been made in theory and experimentation in the past 100 years.

Figure 1.1 shows the operating principle of a SOFC [11]. Ceramics such as yttria-stabilized zirconia,

which function as oxide ion conductors at temperatures from 873 to 1273 K, are used as the solid oxide electrolyte. Oxygen is converted to oxide ions at the cathode and then transported through the ceramic electrolyte to the fuel-rich porous anode where the oxide ions react with hydrogen to form H_2O as shown in Figure 1.1. The specific reaction formula is described below.

At the cathode, oxygen gas is reduced as follows, forming oxide ions:

$$O_2 + 4e^- \rightarrow 2O^{2-} \quad (1.1)$$

At the anode, hydrogen gas is oxidized to H_2O as shown below:

$$2H_2 + 2O^{2-} \rightarrow 2H_2O + 4e^- \quad (1.2)$$

Overall, hydrogen and oxygen produce H_2O as follows:

$$O_2 + 2H_2 \rightarrow 2H_2O \quad (1.3)$$

The overall driving force in SOFCs is the gradient of oxygen chemical potential that exists between a cathode with a high oxygen partial pressure and an anode with a low oxygen partial pressure. A typical single-celled SOFC with air as the oxidizer typically reaches a maximum open circuit voltage of 1.2 V, depending on the temperature, system pressure, and fuel composition. This voltage is clearly insufficient for practical applications. To generate a sufficiently high voltage and power, multiple single cells must be connected in series and/or in parallel, using interconnections and/or cell-cell connectors. Like batteries, each SOFC component exhibits internal resistance to electronic or ionic current flows, often expressed as voltage loss. Thus, the cell voltage is the circuit voltage minus the individual voltage loss of each cell component. Oxygen must move through the electrolyte in the form of oxide ions and the electrolyte must be dense enough to suppress the cross leak of oxygen gas.

To achieve high performance and low operating temperatures, SOFC electrolytes are composed of thin films formed on a support such as an electrode, interconnector, or inert insulator. Various cell shapes have been developed, but the most common is flat or tubular (including cylindrical flat plate).

1.3 Oxide ion diffusion

1.3.1 Point defects

Ionic and electronic defects are caused by an excess of defects in natural components, not by the introduction of foreign species [8]. For example, this occurs in the oxide when there is interaction with the adjacent phase oxygen, as shown in Figure 1.2. At sufficiently high temperatures, the exact position of the phase diagram can be continuously adjusted by changing the oxygen content of the gas phase. Such phase widths are often very small and the resulting change is almost negligible in terms of the total mass or phase energy, although the change in defect density and the associated properties can be immeasurable. Therefore, in MO_2 with n-type conduction, the conductivity decreases significantly as the partial pressure of the surrounding oxygen increases.

$$\frac{1}{2}O_2 + V_O^{\cdot\cdot} + 2e' \leftrightarrow O_O \quad (1.4)$$

In this case, the introduced oxygen occupies oxygen vacancies in the lattice. It is incorporated in the form of O^{2-}, this requires electrons. These are available in MO_2 in the form of conduction electrons.

The actual velocity parameter described below is the mobility u of defect k. It is proportional to the defect diffusion coefficient and also to the jump frequency or jump rate constant. These are activated through the transition barrier as in Eq. (1.5);

$$\frac{D}{RT} = \frac{u}{zF} \tag{1.5}$$

Where D, z, F represent the diffusion coefficient, ion valence, the Faraday constant, respectively. The Boltzmann term is proportional to the attempt frequency and corresponds to the number of successful jumps. Typical attempt frequencies on the order of 10^{13} s^{-1} are often identified by the Debye frequency [12] due to lack of detailed insights. The slight difference in the T dependence of u and D reflected by equation 1.5 can usually be ignored; however, it has already been ignored at k_0 in equation (1.6) below:

$$\tilde{k} = k_0 \exp\left(-\frac{\Delta G}{RT}\right) \propto \exp\left(-\frac{\Delta H}{RT}\right) \tag{1.6}$$

There are three basic jump mechanisms [13]: in the case of the vacancy mechanism shown in Figure 1.3 (a), a normal particle (A_A) hops into a vacancy with an effective charge number Zv opposite to the ionic charge of particle A. This leaves a vacant position (V_A^{Zv}) as shown below:

$$A_A(x) + V_A^{Zv}(x') \leftrightarrow V_A^{Zv}(x) + A_A(x') \tag{1.7}$$

This mechanism works stochastically in the absence of correlation and an external driving force. For example, if the hole is substantially positively charged and an external electric field is applied, the hole moves to the negative side. This mass transport can be explained by considering the actual trajectory of the substantial number of A-particles involved.

Two mechanisms are important for the movement of interstitial particles. In the first, the defect jumps directly from one intrusion site to the next intrusion site as in Figure 1.3 (b), where

$$A_i^{Zi}(x) + V_i(x') \leftrightarrow V_i(x) + A_i^{Zi}(x') \tag{1.8}$$

In the second, A_i^{Zi} phases an adjacent regular particle A into an empty interstitial atom and takes its former place (Figure 1.3 (c)), where

$$A_i^{Zi}(x) + A_A(x^*) + V_i(x') \leftrightarrow V_i(x) + A_A(x^*) + A_i^{Zi}(x') \tag{1.9}$$

For closely packed large ions, the second mechanism is expected to be associated with a lower transition barrier than the direct penetration mechanism that displaces the adjacent A particles shown in Figure 1.3. Electrochemical information is then transmitted from particle to particle, and the single substantive particle under consideration does not travel a large distance because of the vacancy mechanism [14].

Of course, it is possible to maintain the ion flux within a solid when the equivalent electron flux

passes through an external circuit. This is the principle of steady-state conductivity experiments.

1.3.2 Oxide ion diffusion

Solid oxides with a high ion conductivity are attracting considerable attention because they can be used in applications such as SOFCs, sensors, catalysts, and batteries. Oxide ion (O^{2-}) conductors such as zirconia solid solutions [15], ceria solid solutions, and lanthanum gallate compounds [16] have been studied extensively. The development of electrolyte and electrode materials requires a better understanding of the mechanism of ionic conduction; for this, an understanding of crystalline structures at the high temperatures at which these materials function most efficiently [17-26] is very important. Detailed structural analysis makes it possible to observe the structural obstacles and diffusion paths of mobile ions in ionic and mixed conductors [17-26].

Doped lanthanum gallium materials such as $(La_{1-x}Sr_x)(Ga_{1-y-z}Mg_yCo_z)O_{3-\delta}$, which are lanthanum strontium cobaltite and lanthanum strontium cobaltite ferrites with perovskite structure, are promising for use in SOFC as electrolyte and cathode materials, respectively [27-29]. The Oxide ions in the cubic $Pm\bar{3}c$ phase show a highly anisotropic distribution corresponding to high anisotropy among atomic displacement parameters. The most prominent feature is the oxide ion diffusion path. This is along the [110], [011], and [101] directions and forms a three-dimensional network of paths. The diffusion path does not follow the edge of the BO_6 [= $(Ga_{0.8}Mg_{0.15}Co_{0.05})O_{5.6}$] octahedron along the [110] direction, but maintains a constant distance from the B site cation, and the arc display its shape. The characteristics of this curve are consistent with the results obtained by the calculation method [30, 31] and the potential map [32] obtained using the probability density function method. Here, for the first time, Yashima et al. obtained the diffusion path from the nuclear density distribution and demonstrated its temperature dependence [33].

1.4 Electrolyte materials

The SOFC electrolyte must be stable in both reducing and oxidizing environments and must have sufficient high ionic conductivity and low electronic conductivity at the cell operating temperature. In addition, the material must be able to be formed into a thin and strong film that does not leak gas. To date, stable zirconia especially yttria-stabilized zirconia with a fluorite structure has been the most preferred electrolyte for SOFC. Other fluorite oxide ion conductors such as doped ceria have also been proposed as SOFC electrolyte materials, especially for operations at low temperatures (873–1073 K). Recently, other materials including perovskites and hexagonal oxides have been found to have a good ionic conductivity.

1.4.1 Fluorite-structured electrolytes

Oxide ion conduction was first observed by Nernst [9] in ZrO_2 containing 15 wt% Y_2O_3 (yttria stabilized zirconia, YSZ) in the 1890s. Bauer et al. [34] built the first SOFC using this electrolyte.

Figure 1.4 shows the fluorite oxide YSZ. The fluorite structure is a face-centered cubic arrangement of cations; the anions occupy all tetrahedral sites, resulting in numerous octahedral interstitial voids. Therefore, this structure is quite open and rapid ion diffusion is expected. At high temperatures, zirconia has a fluorite structure; at low temperatures, it is stabilized by adding divalent or trivalent cations such as Ca^{2+} or Y^{3+}. Oxide ion conduction is provided by oxide ion vacancies. Inherent defects are corrected by the thermodynamic equilibrium of pure compounds, while external defects are established by the presence of heterovalent dopants. To maintain electrical neutrality, soluble heterovalent ions in ionic compounds are compensated for by increasing the concentration of ionic defects [35]. In the case of ZrO_2 and CeO_2, the conductivity is very low due to the low concentration of oxide ion vacancies. However, the conductivity increases when dopants such as yttria are added. The dissolution of yttria in the fluorite phase ZrO_2 can be described by the following defect equation in Kröger-Vink notation [36]:

$$Y_2O_3 \xrightarrow{ZrO_2} 2Y'_{Zr} + 3O_O^X + V_O^{\cdot\cdot} \qquad (1.10)$$

Each time an yttria molecule is added, one oxygen vacancy is created. The vacancy contribution is given simply from the neutral electrical conditions. In this case, 2 $[Y_{Zr}']$ = $[Vo^{\cdot\cdot}]$, which means that the vacancy concentrations are linearly dependent on the dopant level. Ionic conductivity σ can be expressed as follows:

$$\sigma = en\mu \qquad (1.11)$$

where n is the number of mobile oxide ion vacancies, μ their mobility, and e the charge. For oxide ion conductors such as doped zirconia and ceria, Eq. (1.10) results in Eq. (1.11) with the fraction of mobile oxide ion vacancies, $[V_O^{\cdot\cdot}]$, and the fraction of unoccupied oxide ion vacancies, $[V_O^{\cdot\cdot}]^{-1}$. To move through the crystal, ions must be able to move into an unoccupied equivalent site with a minimum of hindrance, thus

$$\sigma = \frac{A}{T}\frac{\left[V_O^{\cdot\cdot}\right]}{\left[V_O^{\cdot\cdot}\right]} exp\left(\frac{E_a}{RT}\right) \qquad (1.12)$$

where E_a is the activation energy for conduction, R is the gas constant, T is absolute temperature, and A is the pre-exponential factor [37]. The conductivity of doped zirconia and ceria varies as a function of dopant concentration and reaches a maximum at a specific concentration. However, this maximum occurs at much lower concentration than that expected given Eq. (1.12).

Based on the comments of Nowick [37] and Kilner et al. [38] who emphasized the importance of defect pairs that form due to interaction between the oxide ion vacancies, $V_o^{\cdot\cdot}$, and aliovalent cations,

M_{Ce}', in CeO_2:

$$V_O^{\cdot\cdot} + M_{Ce}' = \left(V_O^{\cdot\cdot} M_{Ce}'\right) \tag{1.13}$$

and

$$V_O^{\cdot\cdot} + 2M_{Ce}' = \left(V_O^{\cdot\cdot} 2M_{Ce}'\right) \tag{1.14}$$

Manning et al. [39] suggested that ($V_o^{\cdot\cdot}M_{Ce}'$) is more likely to occur because of the expected random distribution of M_{Ce}'. Kilner and Brook [40] have shown that the effect of the binding enthalpy of an associated ion can significantly affect the population of free vacancies at low temperatures. At these lower temperatures, the association is almost complete such that

$$\left[V_O^{\cdot\cdot} M_{Ce}'\right] \gg \left[V_O^{\cdot\cdot}\right] \tag{1.15}$$

and

$$\left[V_O^{\cdot\cdot}\right] = \frac{B}{T} exp\left(-\frac{E_a}{RT}\right) \tag{1.16}$$

where E_a is the association binding energy and B is a constant. Kilner [41] has noted that both calculated and experimental data for the association enthalpies could be correlated with the ionic radius of the dopant.

1.5 Cathode materials

SOFC cathodes must have a lot of properties, including high conductivity, high catalytic activity for oxygen reduction, and stability with other cell components. In the early stages of SOFC development, platinum was used as the cathode because no other suitable material was available. However, platinum is expensive and is not practical for use in commercial SOFCs, which requires a reduction in the unit price of electricity to be viable. Inexpensive perovskite [42] has the necessary properties and has, as a result, attracted a lot of interest. $LaCoO_3$ has been tested by Tedmon et al. [43] and the initial performance in the cell was good. Figure 1.5 shows the cathode material $LaBO_3$ (B is a transition metal) with a perovskite structure. However, due to the reaction with the YSZ electrolyte, serious deterioration occurred as the operating time was extended. Lanthanum manganite ($LaMnO_3$) based materials then became the focus of study for cathodes. Although the degradation of the lanthanum manganite cathode was less severe, some potential reactions with YSZ were observed, especially at higher cell manufacturing temperatures [44].

The defect structure of perovskite oxides affects their crystal structure and thermodynamic, physical, and chemical properties. Oxygen nonstoichiometry is known as an important defect structure in SOFC perovskite oxides. Oxygen nonstoichiometry was measured by the thermodynamic gravimetry of typical perovskite oxides [45]. Most perovskite oxides are dominated by oxygen

vacancy defects. The number of oxygen vacancies depends on the formation energy of oxygen vacancies and, as a result, different indefinite oxygen ratios are generated. Furthermore, the charge compensation mechanism is strongly related to oxygen vacancy concentrations. For example, strontium-doped lanthanum cobaltite LSC, exhibits a higher oxygen vacancy concentration than undoped lanthanum cobaltite, $LaCoO_3$ [46]. If lanthanum is doped with strontium, the neutral electrical condition is expressed by the following Kröger–Vink notation:

$$\left[Sr'_{La}\right] + \left[Co'_{Co}\right] = 2\left[V_O^{\cdot\cdot}\right] + \left[Co_{Co}^{\cdot}\right] \tag{1.17}$$

Therefore, the decrease in charge caused by doping divalent strontium into trivalent lanthanum must be compensated for by the formation of oxygen vacancies or an increase in the average valence of Co. Charge compensation due to changes in the average valence of Co is described by the following equation:

$$\left[Sr'_{La}\right] + \left[Co'_{Co}\right] = 2\left[V_O^{\cdot\cdot}\right] + \left[Co_{Co}^{\cdot}\right] \tag{1.18}$$

The compensation for oxygen deficiency can be explained as follows:

$$\mathrm{SrO} \rightarrow Sr'_{La} + O_O^{\times} + \frac{1}{2}V_O^{\cdot\cdot} \tag{1.19}$$

The type of compensation that is dominant depends on the energy of the oxygen deficiency formation, but both compensations can actually occur with strontium doping. Changes in oxygen partial pressure and temperature can also cause oxygen non-stoichiometry, as shown below:

$$V_O^{\cdot\cdot} + \frac{1}{2}O_2(g) + Co_{Co}^{\times} \leftrightarrow O_O^{\times} + Co_{Co}^{\cdot} \tag{1.20}$$

One of the important properties of SOFC materials, the oxide ion diffusivity and oxygen catalytic activity of perovskite oxides, is provided by the non-stoichiometry of oxygen. For many perovskite oxides, electrical conductivity is also related to oxygen non-stoichiometry, because the concentration of hole or electron depends on oxygen nonstoichiometry as described in Eq. (1.20).

Lanthanum strontium manganite, commonly used as a SOFC cathode, exhibits its own oxygen nonstoichiometry. The oxygen nonstoichiometry of lanthanum strontium manganite indicates an oxygen excess region and an oxygen vacancy region [47]. In the vacancy region, the defect structure behaves the same way as other perovskite oxides do; however, in the oxygen excess region, there is no place for the excess oxygen in the perovskite and the oxygen excess scenario will not work elsewhere. Neutron diffraction analysis shows that the A site has vacancies in the oxygen-rich lanthanum strontium manganite and the B site is almost filled [48].

1.6 Electrode reaction mechanism

This research focuses on the oxygen reaction electrode of SOFCs. In a SOFC, the oxygen electrode

corresponds to the cathode where oxygen reduction proceeds. In the following manuscript, the cathode is used as the SOFC oxygen electrode. This section describes some of the factors that govern the cathodic reaction.

1.6.1 Elementary reaction on cathode reaction

At the cathodes, oxygen is converted to oxide ions via the charge transfer process. The cathode reactions involve many elementary reaction processes. Figure 1.6 shows the schematic view for the cathode reaction. Porous electrodes that have large enough regions for oxygen reduction reactions are conventionally used as cathodes. The following describes the elementary reaction steps for cathode reactions;

1) Gas diffusion of oxygen molecules in the gas phase

$$O_2(gas) \rightarrow O_2(gas) \tag{1.21}$$

2) Surface adsorption of oxygen molecules on the cathodes

$$O_2(gas) \rightarrow O_{2\,ad}(electrode\ surface) \tag{1.22}$$

3) Dissociation of adsorbed oxygen molecules into adsorbed atoms

$$O_{2\,ad}(electrode\ surface) \rightarrow 2O_{ad}(electrode\ surface) \tag{1.23}$$

4) Surface diffusion of adsorbed oxygen atoms to the triple phase boundary(TPB)

$$2O_{ad}(electrode\ surface) \rightarrow 2O_{ad}(TPB) \tag{1.24}$$

5) Charge transfer reaction of oxygen atoms into oxide ions at the reaction site

$$2O_{ad}(electrode\ surface/TPB) + 4e \rightarrow 2O^{2-} \tag{1.25}$$

6) Incorporation of oxide ions into the electrolyte

$$O^{2-} + V_O^{\cdot\cdot} \rightarrow O_O^X \tag{1.26}$$

It is commonly believed that oxygen reduction at the cathodes occurs in the order of 1) - 2) - 3) - 4) - 5) - 6) (TPB reaction dominated), or 1) - 2) - 3) -5) -6) (bulk pass).

1.6.2 Rate determined step

As shown in Figure 1.6, oxygen reduction at the cathode involves several processes the driving forces for which are usually caused by the difference in chemical potential. Each elemental reaction causes an energy loss called "overvoltage" or "polarization". This is one of the problems of the actual operation of SOFC. Therefore, understanding the reaction mechanism of the electrode is important. Several researches have studied electrode reaction mechanisms; however, consensus on the mechanism has not yet been achieved [49]. This is because the reaction sites are not uniform, especially in the case of porous electrodes, which are distributed three-dimensionally around the TPB. The complex factors of electrode reactions and model electrode processes need to be simplified.

Useful porous electrodes limit practical quantitative analysis. Consider high density electrode/

electrolyte systems to simplify the reaction process. Figure 1.7 (a) shows the key reaction steps of the oxygen reduction charge transfer process at a high-density cathode. Based on the assumption of local equilibrium, the difference in oxygen potential between the electrode/electrolyte interface and the gas phase causes an overvoltage E, as explained below.

$$E = \frac{1}{2F}\left(\mu_{O,int} - \mu_{O,gas}\right) \tag{1.27}$$

where F, $\mu_{O,int}$ and $\mu_{O,gas}$ represent the Faraday constant, oxygen chemical potential at the electrode/electrolyte interface, and at the gas phase, respectively [50]. The origin of oxygen potential shift at the dense electrode is considered a surface reaction, bulk diffusion, or reaction at the interface. Figure 1.7 (b) shows the oxygen potential profile for various rate determined steps. When surface processes such as oxygen adsorption or dissociation are slow, oxygen potential changes at the electrode surface drastically. In contrast, if the bulk transport though the electrode is slow, the potential changes gradually inside the electrode. The boundary transfer limitation generates the potential drop at the electrode/electrolyte interface. The knowledge of the oxygen potential profile is useful for analyzing the electrode reaction mechanism.

However, measuring the oxygen potential under SOFC operating conditions is very difficult as these devices operate at high temperatures and in various atmospheres. A well-defined high-density electrode electrochemical impedance spectroscopy is commonly used to analyze the rate determination step of an electrode reaction. For LSC electrodes, some researchers reported major contributions from surface reactions [51-54]. In contrast, results from lanthanum strontium manganite high density electrodes implied limitations on bulk transport [55-59]. This type of electrochemical measurement however can indirectly estimate the reaction mechanism based on the relationship between the voltage representing energy and the current representing velocity. In this case, different interpretation results and interpretation ambiguities for different reaction models remain in the constructed electrode reaction model.

In order to directly observe the chemical potential of oxygen under SOFC operating conditions, the development of new measurement techniques is strongly required. However, SOFC performs in-situ measurements at high temperatures, various atmospheres, and overvoltages, which make it difficult to run measuring instruments. Recently, several field methods have been developed to perform measurements under device operating conditions [60,61].

1.7 Issues for solid oxide fuel cells

Although SOFC has potential as a highly efficient power generation system, several obstacles must be overcome before it can be put into practical use. SOFC is expected to generate high-efficiency power, but thermal power generation, which is the current centralized power plant, is also efficient at higher temperatures and combined use. Therefore, it is necessary to further improve SOFC power

generation efficiency.

The main causes of SOFC voltage loss are electrolyte IR loss and cathode reaction resistance.

The IR loss of the electrolyte can be improved by increasing electrolyte conductivity and reducing the film thickness. Various processes have been studied to achieve a thin film. However, as the film is made thinner, it loses the capacity to endure denseness, and oxygen gas leaks, leading to a reduction in power generation efficiency. Therefore, in principle, there is a need for a process for creating thin films while ensuring denseness.

On the other hand, many studies to reduce reaction resistance at the cathode have been conducted, in which several materials were prepared and tested for their performance. In other words, there is no design guide for the development of high-performance electrode materials, likely because it is difficult to improve the reaction rate due to a very complicated electrode reaction mechanism. As mentioned above, the SOFC cathodic reaction is strongly related to the steps of electron conduction, ion diffusion, and rate determination. Invesigating these conduction mechanisms and electrode reaction mechanisms would make for an interesting study. In the future, it will be necessary to establish material designs for high performance electrodes based on these scientific studies. In addition, we believe that such basic research causes breakthroughs over the long-term.

1.8 Outline of the present thesis

This paper outlines the research on new thin film fabrication processes that enable low resistance of oxide ion conductive electrolytes, and the local structures of various oxide materials for cathodes.

The overview describes the various SOFC electrolyte and electrode materials, their defect chemistry, and the oxide ion conduction and electrode reaction mechanisms. SOFC is attracting attention as a clean power generation technology that converts fossil fuel into electric power with high efficiency. In the theory of power generation, we will explain the relationship between oxide ion conduction and local structure. The cathode reaction mechanism at the electrode/electrolyte interface and its rate-limiting step are also explained.

Part I focuses on YSZ as the SOFC electrolyte and describes the development of a thin film fabrication for the reduction of IR loss of the electrolyte.

Chapters 2 and 3 describe the principles of new YSZ thin film manufacture, the development of manufacturing equipment, and the physical properties and electrochemical characteristics of the YSZ thin film created by this process. The new process is a thin film fabrication process via gas phase electrolysis that uses gas phase plasma as an electrolyte.

Part II focuses on $LaSrBO_3$ (B = Co, Fe, Mn), the SOFC cathode material, and describes the local structure and oxide ion diffusion with oxygen vacancy formation.

In Chapter 4, $La_{0.6}Sr_{0.4}FeO_{3-\delta}$, $La_{0.6}Sr_{0.4}Co_{0.8}Fe_{0.2}O_{3-\delta}$, and $La_{0.9}Sr_{0.1}MnO_{3-\delta}$ with various oxygen vacancies controlled by oxygen partial pressure are listed. The local structure of the cathode material

is measured by in situ depth resolved XANES. The rate-determining step of the cathode reaction is discussed based on the measurement results of the oxygen chemical potential at the electrode/electrolyte interface and the interior of the electrode. Chapter 5 measures in situ total reflection XAFS and XRF (fluorescence X-ray analysis) of $La_{0.6}Sr_{0.4}CoO_{3-\delta}$. As a result, the compositional change of the electrode surface is clarified, and it was linked with electrode activity change. The possibility of the activity improvement through surface modification is also shown.

Finally, the general conclusions obtained from this study regarding SOFC of higher efficiency are presented.

REFERENCES

[1] J. Hansen, M. Sato, R. Ruedy, K. Lo, D. W. Lea, M. Medina-Elizade, *Proceedings of the National Academy of Sciences of the United States of America,* **103**, (39), 14288 (2006).

[2] P. P. Edwards, V. L. Kuznetsov, W. I. F. David, *Philosophical Transactions of the Royal Society a-Mathematical Physical and Engineering Sciences*, **365**, (1853), 1043 (2007).

[3] M. Z. Jacobson, W. G. Colella, D. M. Golden, *Science*, **308**, (5730), 1901 (2005).

[4] Q. Schiermeier, J. Tollefson, T. Scully, A. Witze, O. Morton, *Nature*, **454**, 816 (2008).

[5] B. C. H. Steele, A. Heinzel, *Nature*, **414**, (6861), 345 (2001).

[6] R. J. Gorte, S. Park, J. M. Vohs, C. H. Wang, *Adv. Mate.*, **12**, (19), 1465 (2000).

[7] E. P. Murray, T. Tsai, S. A. Barnett, *Nature*, **400**, (6745), 649 (1999).

[8] S. D. Park, J. M. Vohs, R. J. Gorte, *Nature*, **404**, (6775), 265 (2000).

[9] W. Nernst, *Z. Electrochem.*, **6**, 41 (1899).

[10] W. Nernst, US Patent 685730, 1899.

[11] S. C. Singhal, K. Kendal, *High Temperature and Solid Oxide Fuel Cells*. Elsevier Science: Amsterdam, (2003).

[12] B. C. H. Steele, *Solid State Ionics*, **129**, 95 (2000).

[13] H. Scmalzried, "Solid State Reaction", ed. VCH, Weinheim, Berlin (1982).

[14] H. Yahiro, Y. Eguchi, K. Eguchi, H. Arai, *J. Appl. Electrochem.*,**18**, 527 (1988).

[15] H. Yahiro, K. Eguchi, H. Arai, *Solid State ionics*, **36**, 71 (1989).

[16] V. Butler, C. R. A. Catlow, B. E. F. Femder, J. H. Harding, *Solid State Ionic*, **5**, 109 (1981).

[17] M. Yashima, D. Ishimura, *Chem. Phys. Lett.,* **378**. 395 (2003).

[18] M. Yashima, D. Ishimura, *Appl. Phys. Lett.,* **87**, 221909 (2005)

[19] H. Inaba, H. Tagawa, *Solid State Ionics*, **83**,1 (1996).

[20] M. Yahisma, K. Nomura, H. Kageyama, Y. Miyazaki, N. Chitose, K. Adachi, *Chem. Phys. Lett.,* **380**, 391 (2003).

[21] R. Ali, M. Yashima, F. Izumi, *Chem. Mater.,* **19**, 3260 (2007).

[22] M. Yashima, T. Tsuji, *J. Appl. Crystallogr.,* **40**, 1166 (2007).

[23] M. Yashima, T. Kamioika, *Solid State Ionics*, **178**, 1939 (2008).

[24] M. Yahisma, *Solid State Ionics*, **179**, 797 (2008).

[25] M. Yashima, M. Enoki, T. Wakita, R. Ali, Y. Matsushita, F. Izumi, T. Ishihara, *J. Am. Chem. Soc.,* **130**, 2762 (2008).

[26] R. Ali, M. Yashima, M. Tanaka, H. Yoshioka, T. Morim, S. Sasaki, *J. Solid State Chem.,* **164**, 51 (2002).

[27] O. Yamamoto, Y. Takeda, R. Kannno, M. Noda, *Solid State Ionics,* **22**, 241 (1987).

[28] J. Mizusaki, Y. Mima, S. Yamauchi, K. Fukui, H. Tagawa, *J. Solid State Chem.,* **80**, 102 (1989).

[29] S. B. Adler, J. A. Lane, B. C. H. Steele, *J. Electrochem. Soc.,* **143**, 3554 (1996).

[30] M. S. Islam, *J. Mater. Chem.*, **10**, 1027 (2000).

[31] M. S. Khan, M. S. Islam, D. R. Bates, *J. Phys. Chem. B.*, **102**, 3099 (1998).

[32] M. Lerch, H. Boysen, T. Hansen, *J. Phys. Chem. Solids.*, **62**, 445 (2001).

[33] M. Yashima, M. Mori, T. Kamiyama, K. I. Oikawa, A. Hoshikawa, S. Torii, K. Saitoh, K. Tsuda, *Chem. Phys Lett.*, **375**, 240 (2003).

[34] E. Baur, H. Preis, *Z. Electrochem.*, **43**, 727 (1937).

[35] E. Koch, C. Wagner, *Z. Phys. Chem.*, **B38**, 295 (1937).

[36] F. Kroger, H. J. Vink, *Solid State Physics*, Vol. 3, eds. F. Seitz and D. Turnbull, Academic Press, New York (1965).

[37] J. A. Kilner, *Solid State Ionics*, **129**, 13 (2000).

[38] Y. Arachi, H. Sakai, O. Yamamoto, Y. Takeda, N. Imanishi, *Solid State Ionics*, **121**, 133 (1999).

[39] S. Nakayama, M. Sakamoto, M. Higuchi, K. Kodaira, M. Sato, S. Kakita, T. Suzuki, K. Itoh, *J Eur. Ceram. Soc.*, **19**, 507 (1999).

[40] M. Higuchi, S. Masubuchi S. Nakayama, S. Kikkawa, K. Kodaira, *Solid State Ionics,* **174**, 73 (2004).

[41] S. Nomura, *Magnetic Oxides and Related Oxides,* **4**, 368 (1978).

[42] S. Nakayama, M. Higuchi, Y. Kondo, M. Sakamoto, *Solid State Ionics*, **170**, 219 (2004).

[43] L. Leon-Reina, E. R. Losilla, M. M. Lara, M. C. Martin-Sedeno, S. Bruque, P. Nunez, D. V. Sheptyakov, M. A. G. Aranda, *Chem. Mater.*, **17**, 596 (2005).

[44] C. S. Tedmon, H. S. Spacil, S. P. Mitoff, *J. Electrochem Soc.*, **116**, 1170 (1969).

[45] S. K. Lau, S, C. Singhai, "Potential electrode/electrolyte interactions in solid oxide fuel cells", *Corrosion*, **85**, 1 (1985).

[46] J. Mizusaki, *Solid State Ionics*, **52**, (1-3), 79 (1992).

[47] J. Mizusaki, Y. Mima, S. Yamauchi, K. Fueki, H. Tagawa, *J. Solid StateChem.*, **80**, (1), 102 (1989).

[48] J. Mizusaki, N. Mori, H. Takai, Y. Yonemura, H. Minamiue, H. Tagawa, M. Dokiya, H. Inaba, K. Naraya, T. Sasamoto, T. Hashimoto, *Solid State Ionics,* **129**, (1-4), 163 (2000).

[49] J. F. Mitchell, D. N. Argyriou, C. D. Potter, D. G. Hinks, J. D. Jorgensen, S. D. Bader, *Phys. Rev. B.*, **54**, (9), 6172 (1996).

[50] S. B. Adler, *Chem. Rev.*, **104**, (10), 4791 (2004).

[51] T. Kawada, J. Suzuki, M. Sase, A. Kaimai, K. Yashiro, Y. Nigara, J. Mizusaki, K. Kawamura, H. Yugami, *J. Electrochem. Soc.*, **149**, (7), E252 (2002).

[52] A. Endo, H. Fukunaga, C. Wen, K. Yamada, *Solid State Ionics*, **135**, (1-4), 353 (2000).

[53] A. Ringuede, J. Fouletier, *Solid State Ionics*, **139**, (3-4), 167 (2001).

[54] P. J. Gellings, H. J. M. Bouwmeester, "*The CRC Handbook of Solid State Electrochemistry.*" CRC Press: New York, 1997.

[55] Y. L. Yang, C. L. Chen, S. Y. Chen, C. W. Chu, A. J. Jacobson, *J. Electrochem. Soc.*, **147**, (11),

4001 (2000).

[56] A. Endo, M. Ihara, H. Komiyama, K. Yamada, *Solid State Ionics*, **86-88**, 1191 (1996).

[57] T. Ioroi, T. Hara, Y. Uchimoto, Z. Ogumi, Z. Takehara, *J. Electrochem. Soc.*, **144**, (4), 1362 (1997).

[58] T. Ioroi, T. Hara, Y. Uchimoto, Z. Ogumi, Z. Takehara, *J. Electrochem. Soc.*, **145**, (6), 1999 (1998).

[59] J. Mizusaki, T. Saito, H. Tagawa, *J. Electrochem. Soc.*, **143**, (10), 3065 (1996).

[60] H. Huwe, M. Froba, *J. Synchrotro Rad.*, **11**, 363 (2004).

[61] B. Yildiz, K. C. Chang, D. Myers, J. D. Carter, H. You, *7th European SOFC Forum*, B06 (2006).

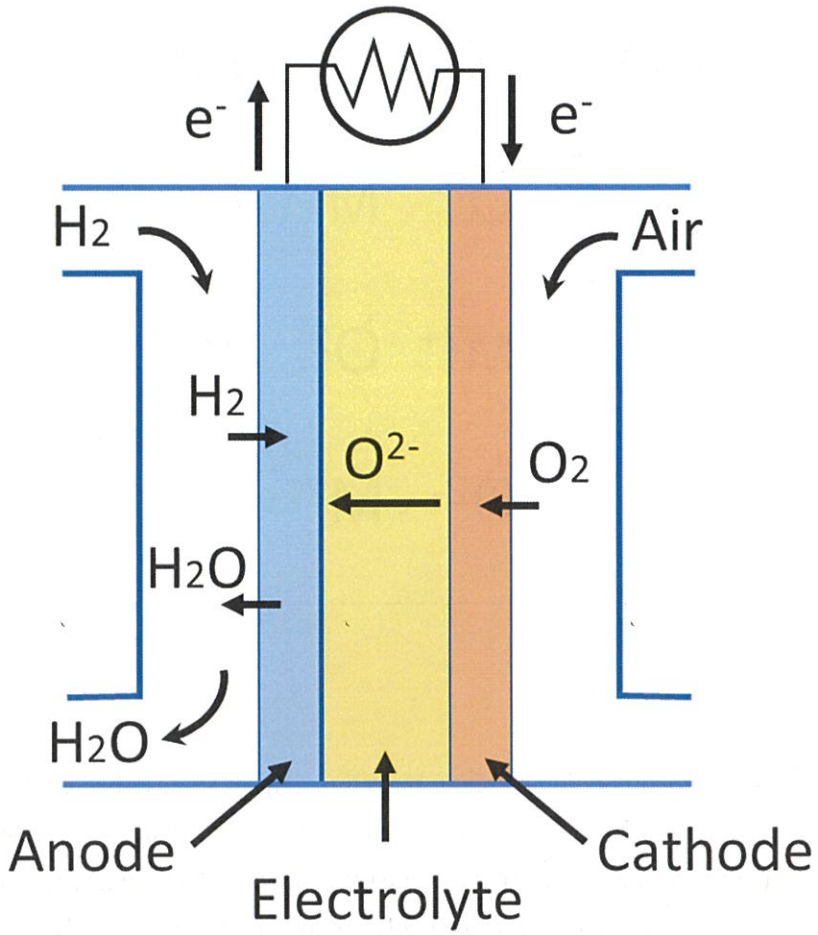

Figure 1.1 Diagrammatic representation of solid oxide fuel cell.

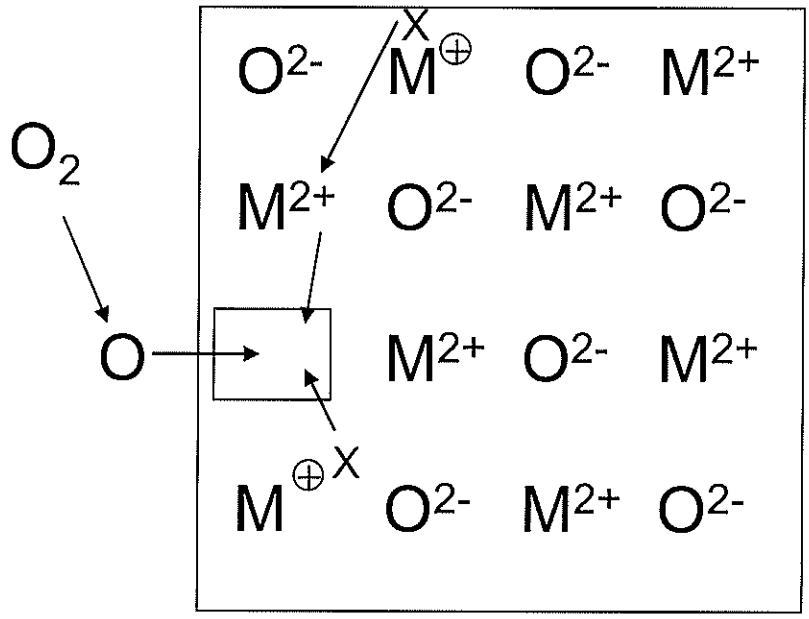

Figure 1.2 Oxygen incorporation resulting from the jump of an adsorbed oxygen particle into a vacant oxygen site along with the uptake of two electrons. In the figure, the excess electron states correspond to monovalent metal ions. It is assumed that the absorbed oxygen is in the neutral state before passing into the vacancy, but this is generally not the case mechanistically.

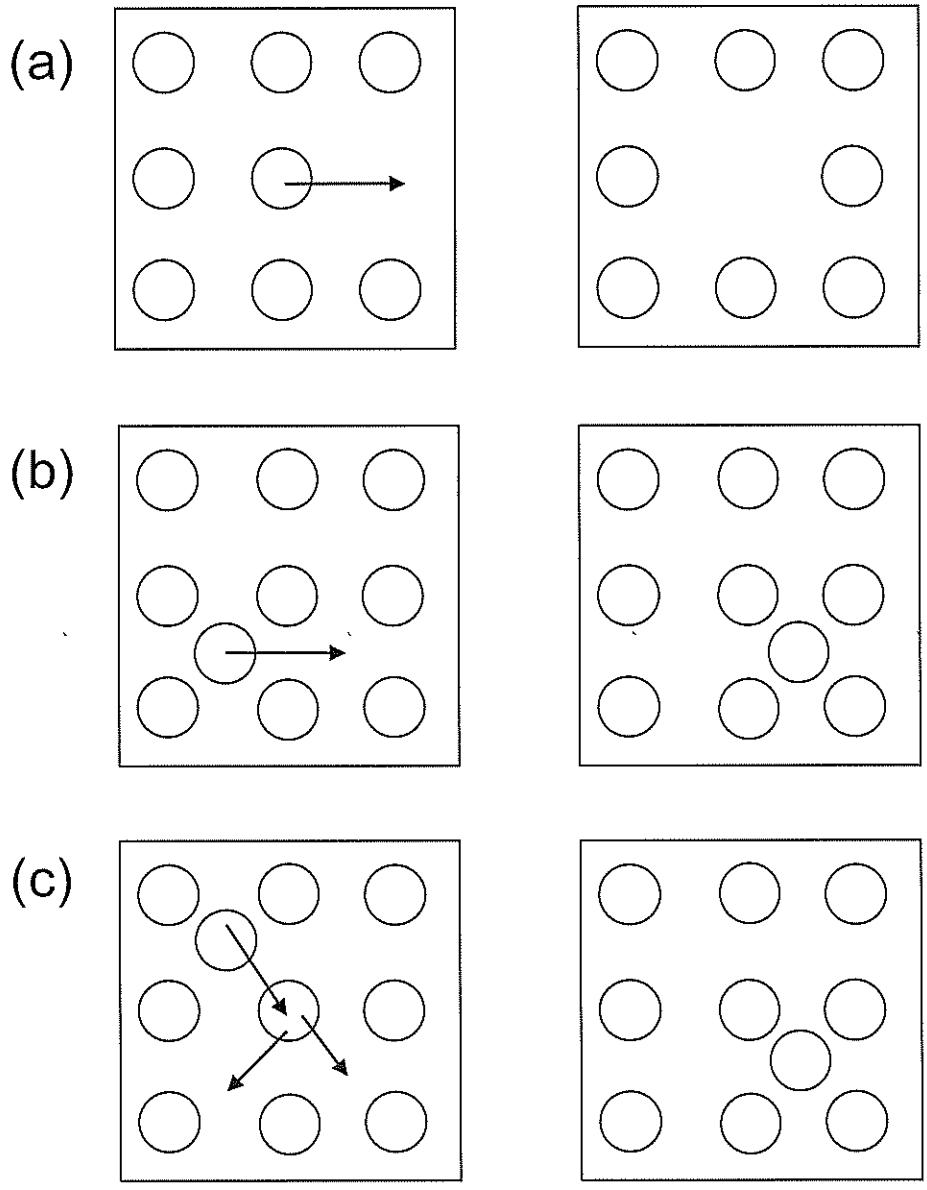

Figure 1.3. Elementary jump mechanisms in crystals: (a) vacancy mechanism, (b) direct interstitial mechanism, and (c) indirect interstitial mechanism.

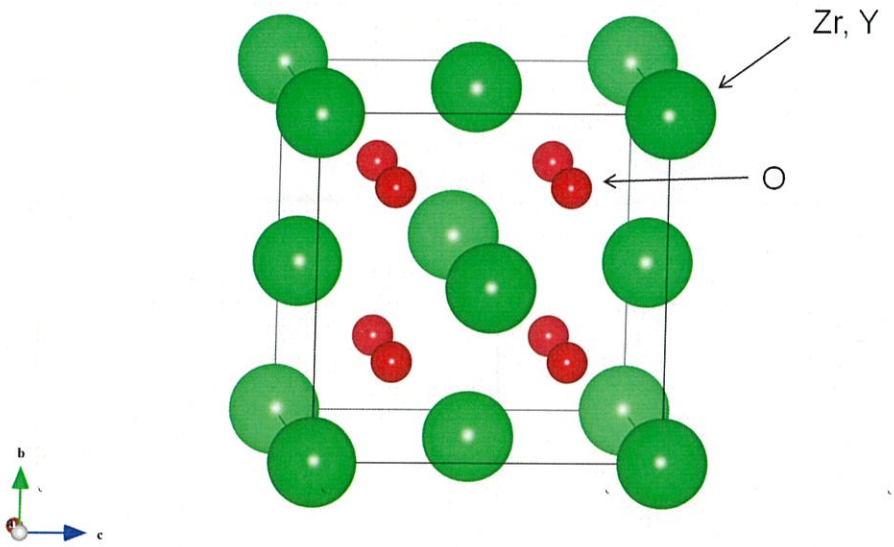

Figure 1.4. Schematic view of fluorite-type structure of yttria stabilized zirconia (YSZ).

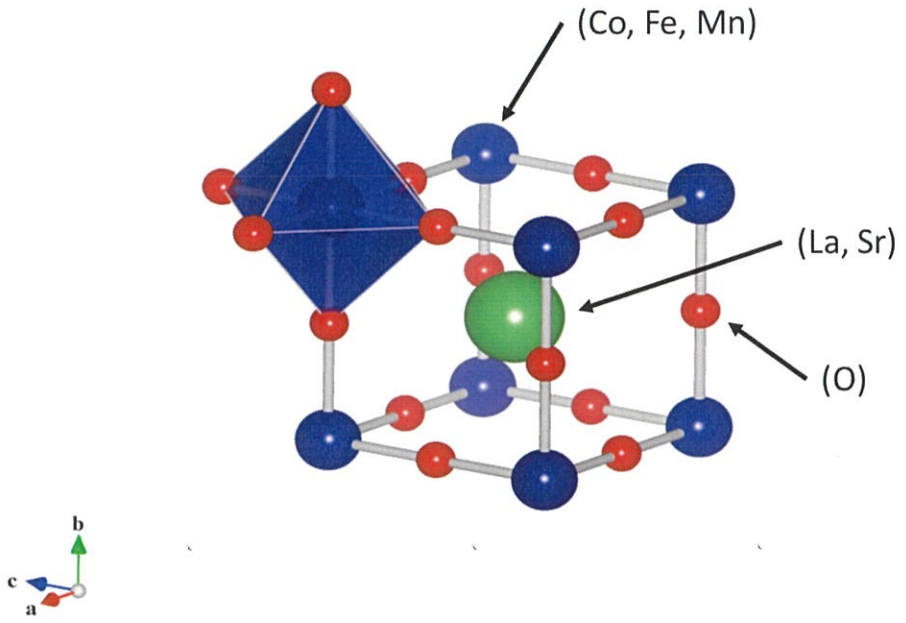

Figure 1.5. Unit cell of perovskite oxides. It consists of La/Sr-site (2a-site), B-site (2b-site) (B = Co, Fe, or Mn) and O-site (*6e*-site).

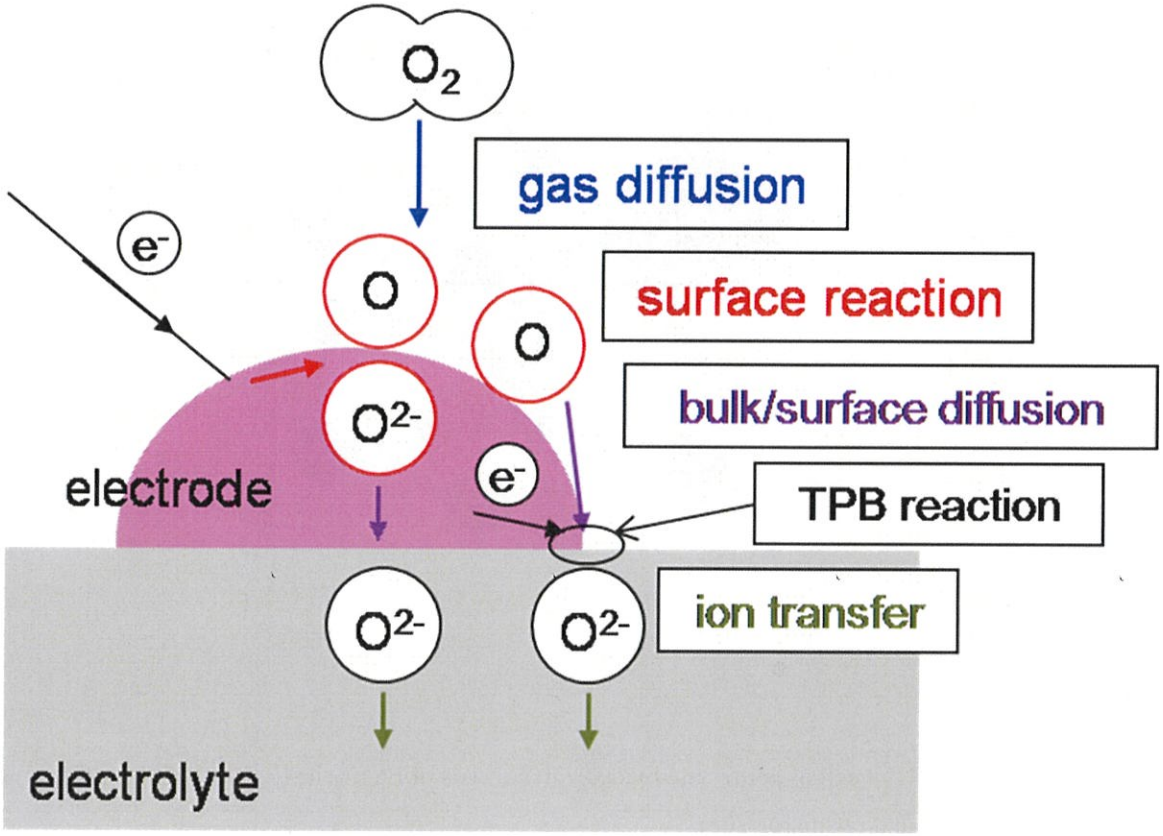

Figure 1.6. Schematic view of cathode reaction. Oxygen is diffused to the electrode surface. At the electrode surface, oxygen molecules are absorbed and dissociated. Absorbed oxygen atoms react with electrons at the triple phase boundary or the electrode surface. Oxide ions diffuse through electrode and electrolytes.

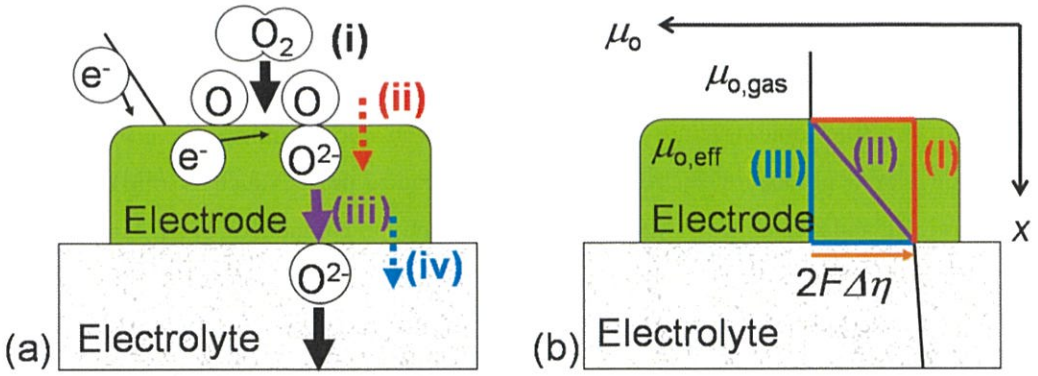

Figure 1.7. (a) Schematic illustration of elementary electrode reactions at the dense electrode/electrolyte interface for high-temperature electrochemical devices. Components (i), (ii), (iii), and (iv) represent the gas diffusion, surface reactions, bulk diffusion, and boundary transfer, respectively. (b) Schematic illustration of oxygen chemical potential profiles around dense electrodes. When voltage is applied to the electrodes, the oxygen chemical potential at the electrode/electrolyte interface shifts. (I), (II), and (III) correspond to the oxygen potential changes when the rate-determining step is the surface reaction, bulk diffusion, and boundary transfer, respectively.

Chaptre 2. Electrodeposition of Thin Yttria-stabilized Zirconia Layers Using Glow-discharge Plasma

2.1. Introduction

The fabrication of thin layers of ionically conductive oxides such as ZrO_2-based solid-solution, stabilized zirconia (the cubic structure phase is stabilized even at low temperature) is important for the successful development of solid electrolytes for electrochemical devices such as solid oxide fuel cells [1,2], sensors [3], and steam electrolyzers [4]. However, the ionic conductivity of stabilized zirconia is somewhat low for use as an electrolyte, typically 1-50 X 10^{-2} S cm^{-1} even at 1000 °C. For practical applications in electrochemical devices, reduction of the resistance of the stabilized zirconia electrolyte will be necessary. One way to reduce the operating resistance is to prepare the electrolyte in the form of a thin film. However, it is not easy to produce thin (μm scale), pinhole-free (gas tight) yttria-stabilized zirconia (YSZ) films with high reliability, and a number of preparation methods have been devised and investigated. These include chemical-vapor deposition (CVD) [5-7], plasma spraying [8,9], rf sputtering [10,11], and electrochemical-vapor deposition (EVD) [12,13]. In this paper, we propose a new method for the preparation of thin yttria-stabilized zirconia (YSZ) films. This new technology is based on electrolytic deposition using a glow-discharge plasma as the conductive medium.

Gaseous plasmas have recently been suggested as candidates for use in electrochemical systems [14,15]. However, the use of a plasma as a medium for conducting electrochemical investigations is difficult, since the charge carriers in plasma consist not only of ionic species, but also of electrons and, as a result, electronic conduction could occur at the interface between a plasma and a solid electrode [16,17].

The three main types of stable plasma are hot plasma, arc plasma, and glow-discharge plasma (also known as low-temperature or nonequilibrium plasma). The temperature of hot plasma (more than a few million degrees) is too high for the investigation of chemical reactions. Previous studies utilizing plasma in electrochemical studies have used a powered electrode in arc plasma as the site of electrochemical reaction [14,15]. However, the temperature of electrodes on which arc discharge occurs is known to become very high, making it difficult to use them as sites for chemical reactions. With glow-discharge plasma, while the temperature of the powered electrode is much lower, the electrode is attacked by accelerated cations, leading to emission of electrons, as well as cathode fall formation. Thus, in this study, in order to eliminate the complexities associated with using a powered electrode to conduct chemical reactions, a third electrode was introduced into the plasma as a site for conducting electrochemical reactions. The introduction of a separate working electrode also allows the potential of the working electrode to be controlled independent of the plasma parameters. A glow-discharge plasma was used in the present work because of its relatively low temperature, compared with arc-

discharge plasma. Under certain conditions, the conductivity of glow-discharge plasma can be as high as 10^{-3} S cm^{-1} [16].

The principle of this new electrodeposition technology (VED) is outlined in Fig. 2.1. The YSZ layer (C in Fig. 2.1) was grown on the surface of a calcia-stabilized zirconia (CSZ) substrate (B) under a dc current flowing through the circuit consisting of porous Pt/oxide/plasma/Pt. The CSZ substrate separates the reactor into two compartments, one containing water vapor (G), and the other in which an rf glow discharge is generated (D). A porous platinum layer (A) is deposited beforehand on the surface of the CSZ which contacts the compartment containing water vapor. Water is cathodically reduced at the interface between this porous Pt electrode (A) and the ionically conductive CSZ (B), forming H_2 and O^{2-}. The O^{2-} is directed to the CSZ surface facing against the plasma under the influence of a potential gradient across the CSZ induced by an applied dc bias. After reaching the interface, the O^{2-} contacts and reacts with $ZrCl_4$ and YCl_3 (which are contained in the glow-discharge plasma) to form YSZ and Cl^-. The dc circuit is completed by charge carried through the conductive plasma to a second platinum electrode (E) located in the plasma.

2.2. Experiment

2.2.1. Apparatus

The apparatus used for deposition of YSZ layers is shown schematically in Fig. 2.2. The reactor was constructed of two tubes, an external quartz glass tube (5 in Fig. 2.2) and an alumina tube (6 in Fig. 2.2). The alumina tube formed an inner compartment to which water vapor was supplied, and the space between the alumina tube and the quartz tube formed an outer compartment in which glow-discharge plasma was generated. These two compartments were exhausted separately by two rotary pumps.

A nonporous calcia-stabilized-zirconia (CSZ) tube (Nippon Kagaku Togyo Co., Ltd., 10 mm o.d., 2 mm wall thickness) was used as the substrate for the deposition of YSZ layers. This tube was inserted (cemented) between two pieces of the inner alumina tubing. The outer surface of the CSZ tube was used directly as the substrate for oxide electrodeposition. A porous platinum layer was sintered on its inner surface (2' in Fig. 2.2). The temperature of the substrate was kept at 1100 °C by an electric furnace surrounding the outside of the quartz glass tube. Two platinum rings (2 in Fig. 2.2) were placed in the outer compartment surrounding the alumina tube. One of the platinum rings was connected to the rf source via a matching network and the other was grounded. The porous platinum layer was connected to the dc power source (negative terminal). The grounded platinum ring was also used as a counter electrode to complete a dc circuit.

Anhydrous $ZrCl_4$ (Wako Pure Chemicals) and anhydrous YCl_3 (Aldrich 99.9%) were used as the metal sources for the oxide deposition process. Crucibles containing the chlorides were set in two side arms connected to the quartz glass tube. The side arms were heated separately by two small

furnaces: The $ZrCl_4$ was kept at 280 °C, and the YCl_3 was kept at 790 °C. The resulting metal chloride vapor was carried by Ar gas [99,9%, 20 cm^3 (STP) min^{-1}] and introduced into the outer compartment, over the outside surface of the CSZ substrate. The Ar gas also served as a plasma-assisting gas for the generation of glow-discharge plasma.

Water for the cathode reaction was supplied to the inner compartment by bubbling Ar gas [5 cm^3 (STP) min^{-1}] through a thermostated humidifier kept at 30 °C.

2.2.2. Deposition procedure

After the system had reached the desired temperature, the respective source gases were introduced into the two compartments. The pressure in the outer compartment was set at 1.5 Torr by controlling a throttle valve. The pressure of the inner compartment was not monitored but it was estimated as being a little higher than that in the outer compartment from an evacuation test (conducted by connecting only one rotary pump to the inner alumina tube, which was left open at one end). The plasma was generated by two platinum rings (rf electrode and grounded electrode). After the gas pressure had stabilized, the rf power (13.5 MHz, 100 W) was turned on, and then a dc bias of 130 V was applied between the porous platinum electrode (cathode) and the grounded platinum ring electrode (anode). The deposition was carried out for 1-2 h.

2.2.3. Analytical procedures

The YSZ films formed by VED were examined by scanning electron microscopy (SEM) (Hitachi model S51), electron probe microanalysis (EPMA) (Horiba model EMAX-1770), electron spectroscopy for chemical analysis (ESCA) (Shimadzu model ESCA-850), and x-ray diffraction (Shimadzu XD-5A). Yttrium contents in the deposited films were calculated from the results of EPMA and ESCA measurements. Film thicknesses were determined from SEM micrographs of film cross sections

2.3. Results

2.3.1. Deposition of thin film layers containing yttrium

As shown in Fig. 2.3, upon application of 130 V dc bias, dc current passed through the dc circuit. The current density initially dropped from 7 to about 2 mA cm^{-2} within 20 min, and then remained almost constant (very slow decrease with time). The low-current densities, obtained despite the high applied voltage, can be attributed to the high resistance of the bulk plasma and the ion sheath formed at the oxide-plasma interface (see Sec. 2.4.). The reason for the initial rapid decrease in the dc current is not yet clear.

After a reaction for 2 h at 130 V, the CSZ substrate was cooled to room temperature under Ar atmosphere and then analyzed by EPMA (elemental analysis). The EPMA spectrum for the substrate

after the reaction is shown in Fig. 2.4(a). The spectrum shows strong yttrium K_α and K_β peaks, while only a small calcium K_α peak (from the CSZ substrate) is visible. These results show that the CSZ substrate was covered by an yttrium-containing layer. As a basis for comparison, another run was carried out under the same conditions, but without applying the dc bias. The yttrium peaks in the EPMA spectrum [see Fig. 2.4(b)] were negligible for this latter run without dc bias. These results indicate that deposition of yttrium, i.e., deposition of YSZ, occurred only when a dc bias was applied. Furthermore, the fact that yttrium was not deposited without a dc bias implies that deposition by the process known as electrochemical-vapor deposition (EVD) [12,13] was negligible. Under the conditions used in the present work, the rate-controlling step of the EVD process is electron transport in the stabilized zirconia, and thus the rate of EVD was inversely proportional to the thickness of the stabilized zirconia [18]. As a result, the large thickness of the CSZ substrate used in this study likely rendered the driving force for EVD negligible.

As further confirmation of the necessity of passing a dc current through the dc bias circuit in order to deposit an yttrium-containing layer, the relative amounts of yttrium deposited on the substrate were compared with those expected from the current distribution in the reactor. Since the porous platinum electrode and the counter electrode were not positioned parallel to one another in the reactor (see Fig. 2.2), the dc current distribution was asymmetric, as in conventional liquid-electrolyte electrolyzers. Furthermore, since the conductivity of glow-discharge plasma is lower than that of conventional liquid electrolytes [the conductivity of a glow-discharge plasma of hydrogen has been reported as 6 mS cm^{-1} (Ref. 16)), the ohmic resistance between the counter (grounded) electrode and the substrate was likely significantly higher at positions farther from the counter electrode. Consequently, the dc current at the CSZ substrate likely decreased with increasing distance from the counter electrode. If the current flowing in the reactor directly corresponds to deposition of the yttrium-containing layer, then the distribution in the current should have resulted in a corresponding distribution of the deposition rate; the farther from the counter electrode, the slower the rate of deposition should have been [19]. Accordingly, as a measure of the deposition rate, the yttrium content of a film was analyzed by ESCA combined with repeated argon etching. The average amount of deposited yttrium of the half of the sample closest to the counter electrode was twice as high as that of the half of the sample farthest from the counter electrode. These results indicate that the currents flowing at the substrate do indeed correspond to the deposition of the yttrium-containing layer.

2.3.2 Characterization of deposited layer

After the deposition process, the substrate was cooled to room temperature under argon atmosphere and then analyzed.

The x-ray-diffraction pattern of the deposited layer (Fig. 2.5) corresponds to that of cubic zirconia. However, in every peak of the x-ray-diffraction pattern, a shoulder or splitting was observed. The x-

ray-diffraction pattern of YSZ is similar to that of CSZ, except that it shifts to a slightly lower angle [20]. Thus, the x-ray-diffraction pattern of the deposited film corresponds to that expected for a thin layer of cubic YSZ on a CSZ substrate.

The yttrium content of the YSZ layer was estimated as 6-10 mol % by ESCA measurements.

Depth profiles for calcium and yttrium obtained by EPMA are shown in Fig. 2.6, which shows that the peak strength of calcium K_α line in the deposited YSZ film is very weak, which is the level of magnitude of background of continuous x-rays. Furthermore, ESCA measurements of the surface of the YSZ film revealed that a Ca is peak was not detected. These facts indicate that calcium was not present in the deposited film. Taking the resolution of EPMA measurements into consideration, the distributions of the peaks for both yttrium and calcium at the film/substrate interface were sharp enough to conclude that the YSZ film was not formed by exchange of calcium from the CSZ substrate with yttrium. This conclusion also is supported by the x-ray-diffraction measurements, since the peaks of the x-ray spectrum were not broadened after reactions, but were separated into two or had a shoulder. Since x-ray-diffraction patterns of YSZ and CSZ (substrate) are very similar to each other, the peaks to assignable to YSZ and CSZ were not completely separated and appeared as shoulders.

Scanning electron micrographs of the fracture cross section and the surface of the deposited film are shown in Figs. 2.7(a) and 2.7 (b), respectively. Figure 2.7(a) indicates that a film of about 3 μm thickness was deposited on the CSZ substrate and the thickness is uniform. Figure 2.7(b) shows that in spite of the presence of many small facets of approximately 1 μm, the surface of the deposited YSZ film is free from pinholes, at least within the scale of SEM observation. The current efficiency for the deposition was calculated from this apparent average thickness and the charge passed, assuming that the YSZ formation proceeded via a four-electron process (see following section). The current efficiency thus calculated was 40%.

2.4. Discussion

2.4.1. Probable model for the growth of YSZ layer

As described in the previous sections, an YSZ layer was deposited on the CSZ substrate. It was confirmed that the dc current flowing through the dc circuit was essential for the growth of the YSZ layer. The circuit shown in Fig. 2.1 considered Cu/Pt (H_2O) /CSZ-YSZ/plasma (MCl_x) /Pt/Cu. Copper and platinum are electronic conductors, and both CSZ and YSZ are fairly good ionic conductors at the elevated temperature used in this work. The fact that a cubic yttria-stabilized-zirconia layer was deposited on the surface of a nonporous substrate contacting a gas phase which did not contain any source of oxygen indicates that oxygen was supplied through the oxide substrate. Furthermore, the fact that YSZ formation was observed solely under the application of a dc bias, i.e., when a dc current was passed, suggests that the oxygen was supplied in the form of O^{2-} ions, which were transported through

the ionically conductive oxide layer.

When a de bias is applied, some electrode reactions must take place at the Pt (electronic conductor)-CSZ (ionic conductor) interface in order to permit the passage of dc current, i.e., some cathodic reduction must occur at the interface. The reduction of water is the most probable cathodic reaction (see Fig. 2.1),

$$H_2O + 2e^- = H_2 + O^{2-} \quad (2.1)$$

The released O^{2-} migrates toward the oxide/plasma interface through the oxide layer under the driving force of the electric field generated by the applied dc bias. When O^{2-} reaches the oxide-plasma interface, O^{2-} is exposed to the plasma which contains $ZrCl_4$ and YCl_3. YSZ can then be formed as follows:

$$ZrCl_4 + 2O^{2-} = ZrO_2 + 4Cl^-, \quad (2.2)$$

$$2YCl_3 + 3O^{2-} = Y_2O_3 + 6Cl^-. \quad (2.3)$$

The charge carrier changes from O^{2-} in the oxide phase to Cl^- in the gas phase. Therefore, the phenomena that occur at the oxide-plasma interface are analogous to reactions occurring at the interface between two immiscible electrolyte solutions when the charge carriers are different in the two phases [21]. Since the deposit YSZ is an oxide-ion conductor, the deposition process continues, and the YSZ layer grows continuously. The Cl^- ions released by reactions (2.2) and (2.3) move into the bulk plasma.

A variety of species were present in the plasma. Since argon was used as the plasma-assist gas in the present study, the cations existing in the plasma were mainly Ar^+ but cations formed from metal halides, such as $ZrCl_3^+$, YCl_2^+, and others also may have been present. Anions formed by electron attachment to metal chlorides and neural species formed from metal chlorides in activated states also may have existed in the plasma. Since the CSZ substrate is negatively biased, an ion sheath is formed on the oxide surface [17] (see below), and anions and electrons are rejected from the surface due to a strong electric field of the ion sheath. Neutral species and cations, which are accelerated by the electric field through the ion sheath, may react with O^{2-} at the interface. If Ar^+ were to react with O^{2-}, oxygen atoms would be formed,

$$2Ar^+ + O^{2-} = 2Ar + O. \quad (2.4)$$

Oxygen atoms formed in the manner would immediately react with metal chlorides to form oxides, possibly in the vapor phase,

$$ZrCl_4 + 2O = ZrO_2 + 4Cl, \quad (2.5)$$

$$2YCl_3 + 3O = Y_2O_3 + 6Cl. \quad (2.6)$$

Reactions of O^{2-} with metal chloride cations and neutral activated metal chlorides would yield oxides in a manner similar to that shown in Eqs. (2.2) and (2.3) except that the negative charge of O^{2-} would be partly neutralized by the positive charge of the metal chloride cations.

2.4.2. Voltage loss through the dc circuit

As shown in Fig. 2.3, the magnitude of the dc current was small despite a high applied dc bias (130 V). The voltage required to drive the electrochemical reactions was less than several volts, and the conductivity of the substrate CSZ and the deposited YSZ were relatively high compared with the conductivity of the plasma. Therefore, the high resistance through the dc circuit can be mostly ascribed to the low conductivity of the plasma phase. The main charge carrier in plasma is electrons since their mobility is much higher than that of ionic species. The cationic species, which are generated by electron collisions and by Penning dissociation by excited species, serve to maintain macroscopic electroneutrality in the bulk plasma. In the plasma utilized in the present investigation, however, electron density likely was lowered by the combination of electrons with the electronegative metal chlorides [22,23], resulting in a low bulk plasma conductivity.

Significant voltage losses also can be ascribed to ion sheath and electron sheath formation [17], The potential drop through ion sheathes can reach several tens of volts. In the present system, dc current flowed through the ion sheath formed on the oxide surface. Evaluation of potential drop through the ion sheath is currently being conducted.

2.4.3. Current efficiency of oxide deposition

While the oxide layer can be considered to be primarily an oxide (O^{2-}) conductor, the possibility of some electronic conduction through the oxide layer cannot be excluded. Such electronic conduction leads to a current leakage, which does not result in the production of any oxide. Any electronic conduction would therefore decrease the current efficiency.

Cations are transported and accelerated toward the negatively biased electrode under the potential field prevailing in the sheath, as is often the case with electrodes for plasma generation. When the cations have a high energy (potential or kinetic energy), they etch the electrode surface ("etching" phenomena). This etching also decreases the current efficiency of oxide deposition.

If reactions (2.5) and (2.6) proceeded in the vapor phase, the oxides formed in the vapor phase would not contribute to the growth of the oxide layer, and the current efficiency for solid oxide deposition would be reduced.

2.4.4. Anodic reactions in the EVD process

Since an ionic conductor was incorporated into the dc circuit, some anodic reactions had to take place in order to form a closed circuit for the external dc bias. Possible anodic reactions are oxidation of the anode metal resulting in metal chloride formation, and chlorine production on the anode. Furthermore, since plasma is conductive toward electrons, it also is conceivable that the anodic reactions could take place in the bulk plasma. The anodic reactions in the present system are not clear yet.

2.5. Conclusion

The electrochemical deposition of yttria-stabilized zirconia films in a dc circuit containing a glow-discharge plasma as a conductive medium was demonstrated. Although some points (e.g., anodic reactions) still remain to be clarified, it has been confirmed that an electrolytic process can be made to occur in such a system. Electrochemical systems using glow-discharge plasma are of interest not only because of their numerous potential applications, but also because of their importance to the theoretical understanding of electrified interfaces. The operating variables for this process (bias voltage and external current) are easily controlled for vapor-phase processes, such as those that are widely investigated for the preparation of functional thin films for semiconductors, oxide superconductors, and fuel cells.

Ackknowledgments

This work was partly supported by Grants-in-Aid for Scientific Research from the Ministry of Education, Science, and Culture of Japan (Grants No. 02203114 and No. 02650585). The useful discussions and suggestions of Dr. James T. Hinatsu are gratefully acknowledged.

REFERENCES

[1] N. J. Maskalick and C. C. Sun, *J. Electrochem. Soc.* **118**, 1386 (1971).

[2] A. O. Isennberg, *Solid State Ionics* **3/4**, 431 (1981).

[3] Y. Miyahara, K. Tsukuda, and H. Miyagi, *J. Appl. Phys.* **63**, 2431 (1988).

[4] E. J. L. Schouler, M. Kleitz, E. Forest, E. Fernandez, and P. Fabry, *Solid State Ionics* **5**, 559 (1981).

[5] J. Minet, F. Langlais, and R. Naslain, *J. Less-Common Met.* **132**, 273 (1987).

[6] Yamane and T. Hirai, *J. Cryst. Growth* **94**, 880 (1989).

[7] Y. Takiahashi, T. Kawae, and M. Nasu, *J. Cryst. Growth.* **74**, 408 (1986).

[8] G. Chiodelli, A. Magistris, M. Scagliotti, and F. Parmigiani, *J. Mater. Sci.* **23**, 1159 (1988).

[9] M. Scagliotti, F. Parmigiani, G. Samoggia, G. Lanzi, and D. Richon, *J. Mater. Sci.* **23**, 3764 (1988).

[10] A. Negishi, K. Nozaki, and T. Ozawa, *Solid State Ionics* **3/4**, 247 (1981).

[11] N. Nakagawa, H. Yoshioka, C. Kuroda, and M. Ishida, *Solid State Ionics* **35**, 249 (1989).

[12] A. O. Isemberg, ECS Symp., Electrode Materials, Processes Energy Conversion and Storage, 1977, Vol. 77-6, p. 572.

[13] M. F. Carolan, and I. N. Michaels, *Solid State Ionics* **25**, 207 (1987).

[14] K. Kawabuchi and S. Magari, *J. Appl. Phys.* **50**, 6222 (1979).

[15] A. K. Vijh, *Modern Aspects of Electrochemistry,* edited by I. O'M. Bockris, B. E. Conway, and R. E. White (Plenum, New York, 1986), Vol.17, Cbap.1.

[16] A. von Engel, *Electric Plasmas: Their Nature and Use* (Taylor & Francis, London, 1983).

[17] B. Chapman, *Glow Discharge Processes* (Wiley, New York, 1980), Chap. 3.

[18] "W. H. Rhodes and R. E. Carter, *J. Am. Ceram. Soc.* **49**, 244 (1966).

[19] J. Newman, *Electrochemical Systems* (Prentice-Hall, Englewood Cliffs, NJ, 1973), Chap. 21.

[20] Powder Diffraction File, cards no. 30-1468 and no. 26-341, Joint Committee on Powder Diffraction Standards, Swarthmore, PA.

[21] Samec, V. Merecek, J. Koryta, and M. W. Khalil, *J. Appl. Phys.* **83**, 393 (1977).

[22] R. A. Gottscho and C. E. Gaeb, *IEEE Trans. Plasma Sci.* **PS-14**, 92 (1986).

[23] G. L. Rogotf, J. M. Kramer, and R. B. Piejale, *IEEE Trans. Plasma Sci.* **PS-14**, 103 (1986).

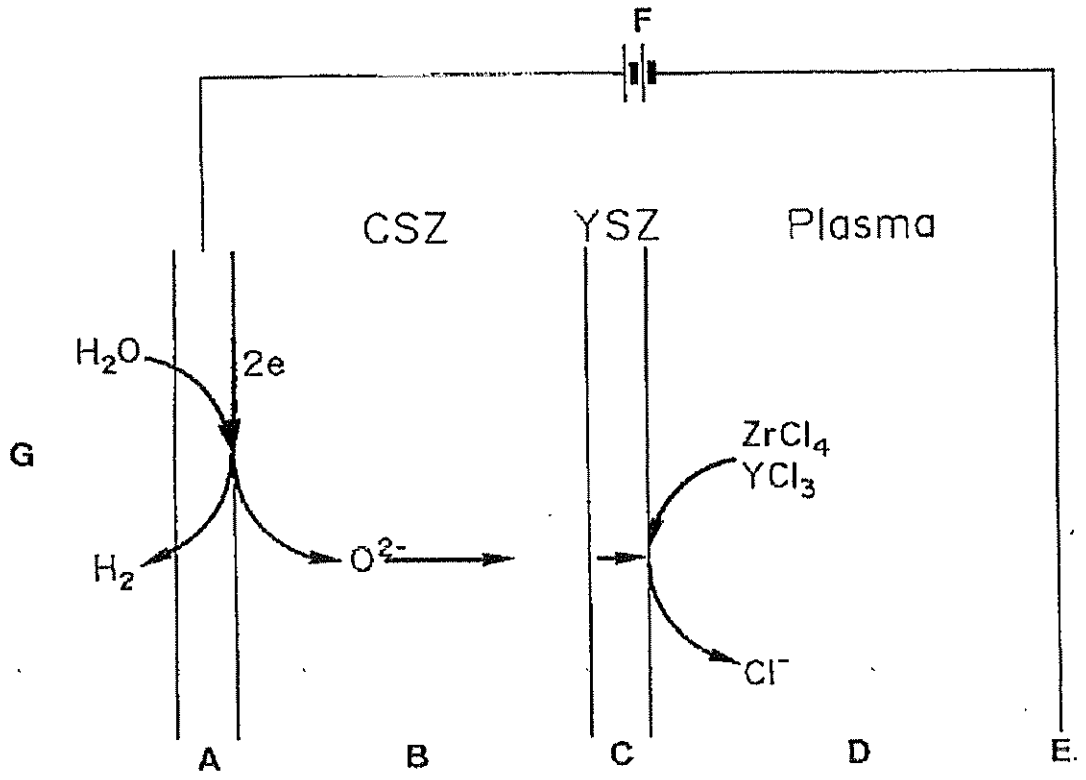

Figure. 2.1. Principle of YSZ layer deposition using a glow-discharge plasma as a conductive medium under an applied de bias voltage through a dc circuit. A: Porous platinum layer; B: nonporous CSZ substrate; C: growing YSZ layer; D: argon glow-discharge plasma containing $ZrCl_4$ and YCl_3 vapors; E: counter electrode (platinum); F: dc power source; G: argon containing water vapor.

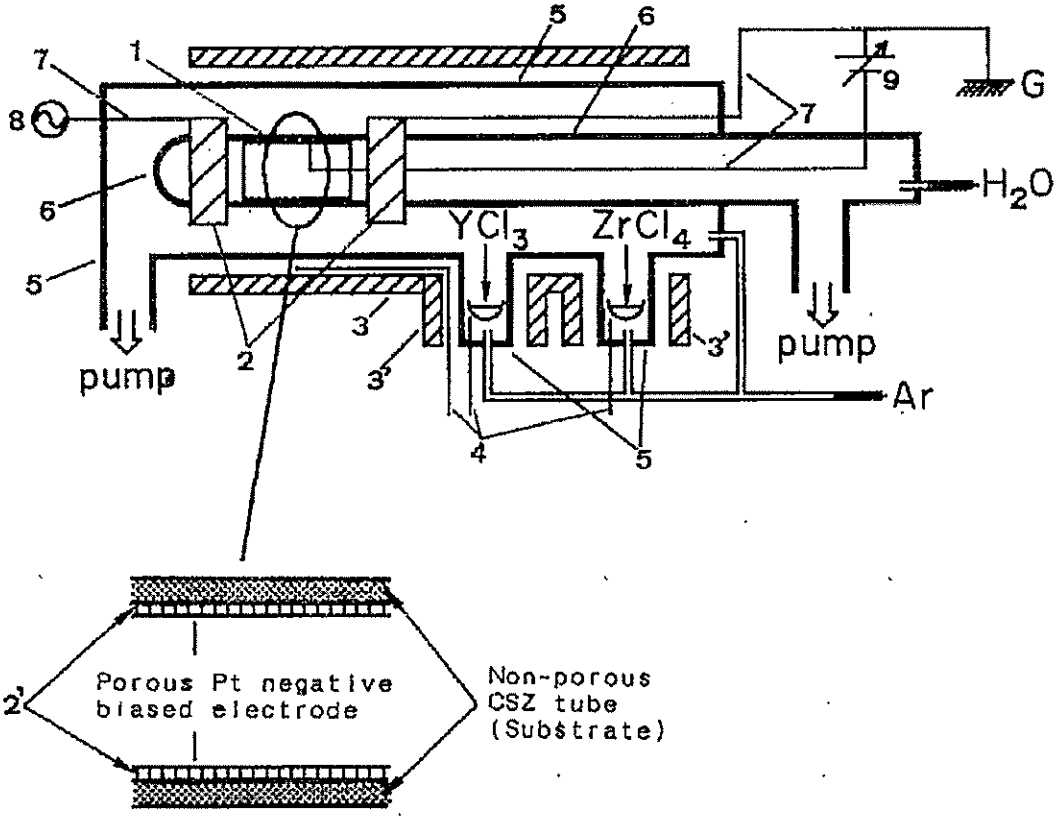

Figure. 2.2. Schematic of apparatus for vapor-phase oxide deposition (VED). 1: Calcia-stabilized zirconia (CSZ substrate); 2: Pt ring electrodes; 2': porous Pt electrode deposited on the CSZ substrate; 3: main furnace; 3': small furnaces; 4: thermocouples; 5: quartz glass tube; 5': side arms of quartz tube; 6: alumina tube; 7: Pt lead; 8: rf power supply; 9: dc power supply.

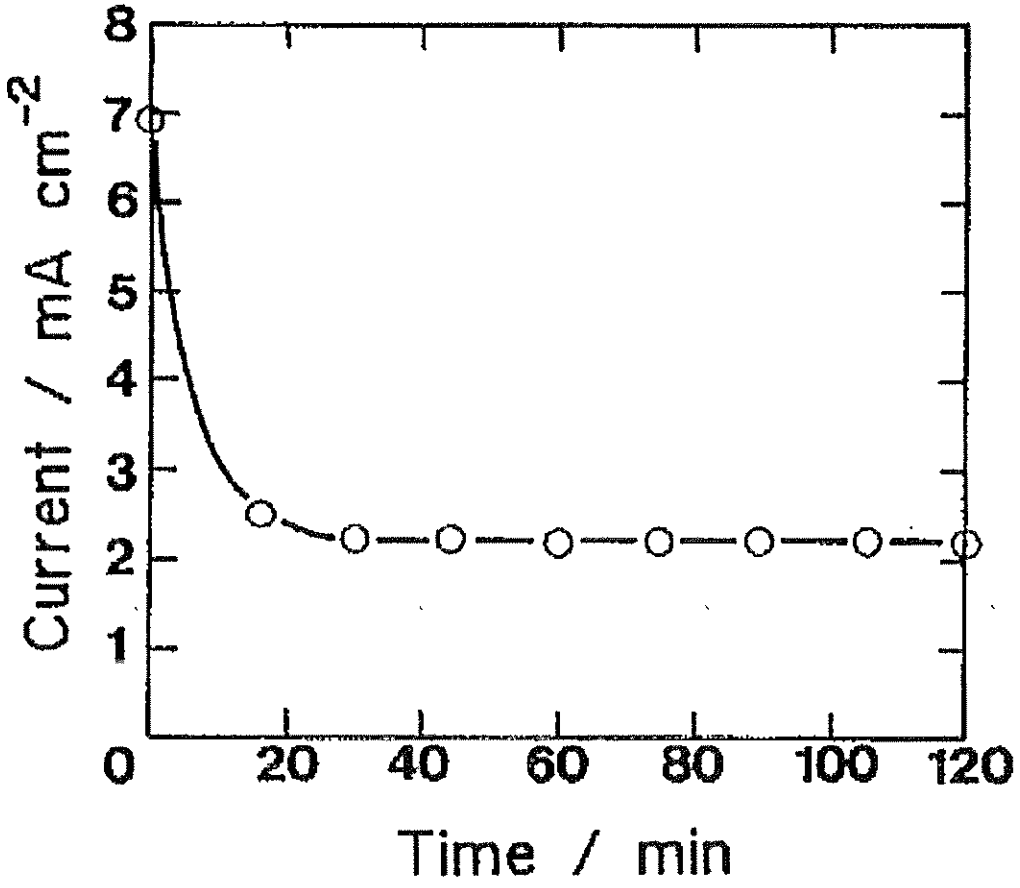

Figure. 2.3. Variation of current density with time. VED reactor conditions: pressure of outer compartment of the reactor is 1.5 Torr; if power is 100 W; dc voltage is 130 V; substrate temperature is 1100 °C; temperature of $ZrCl_4$ source is 280 °C; temperature of YCl_3 source is 790 °C; temperature of H_2O source is 30 °C.

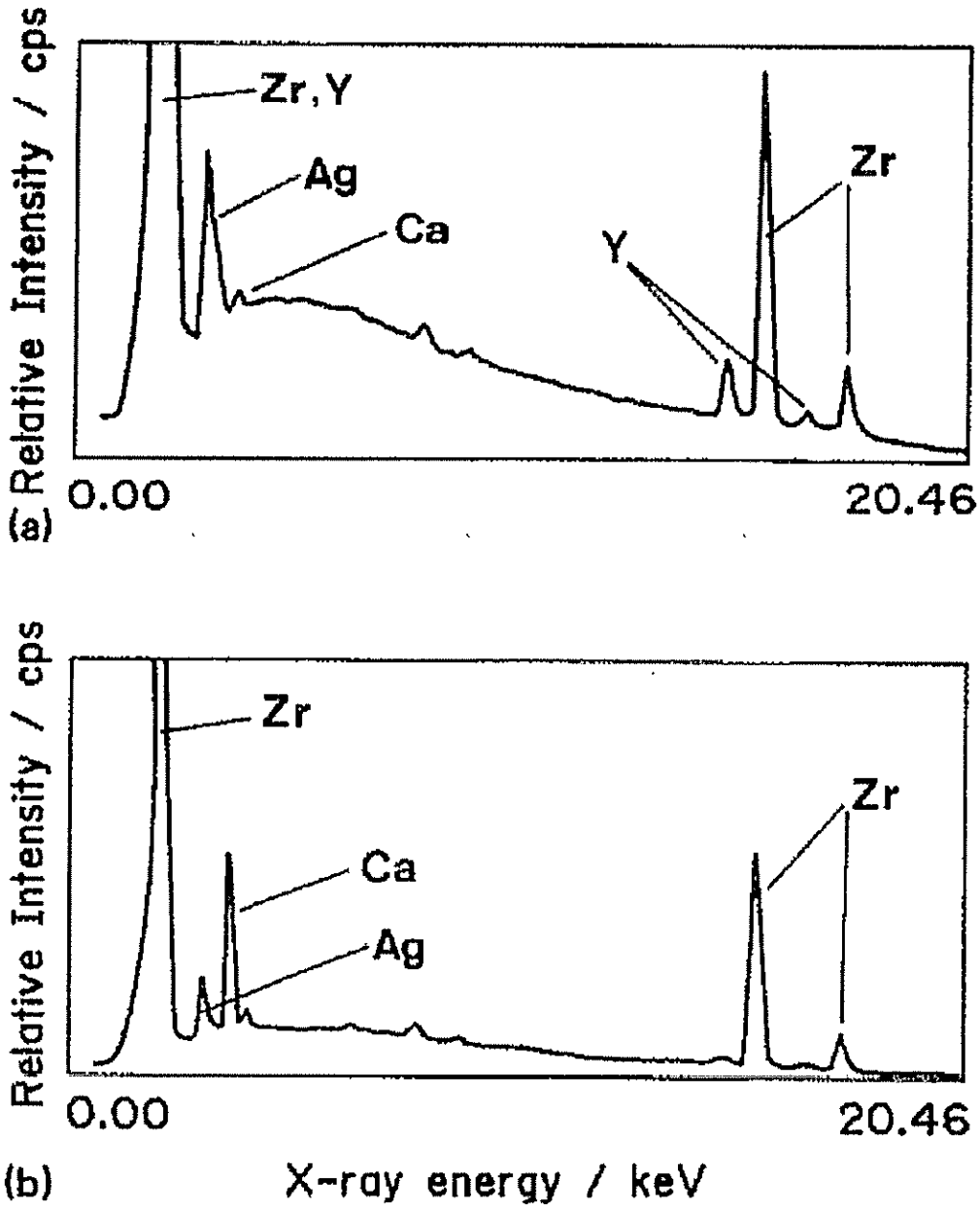

Figure. 2.4. EPMA spectra of a substrate after VED (a) with dc bias of 130 V, and (b) without dc bias.

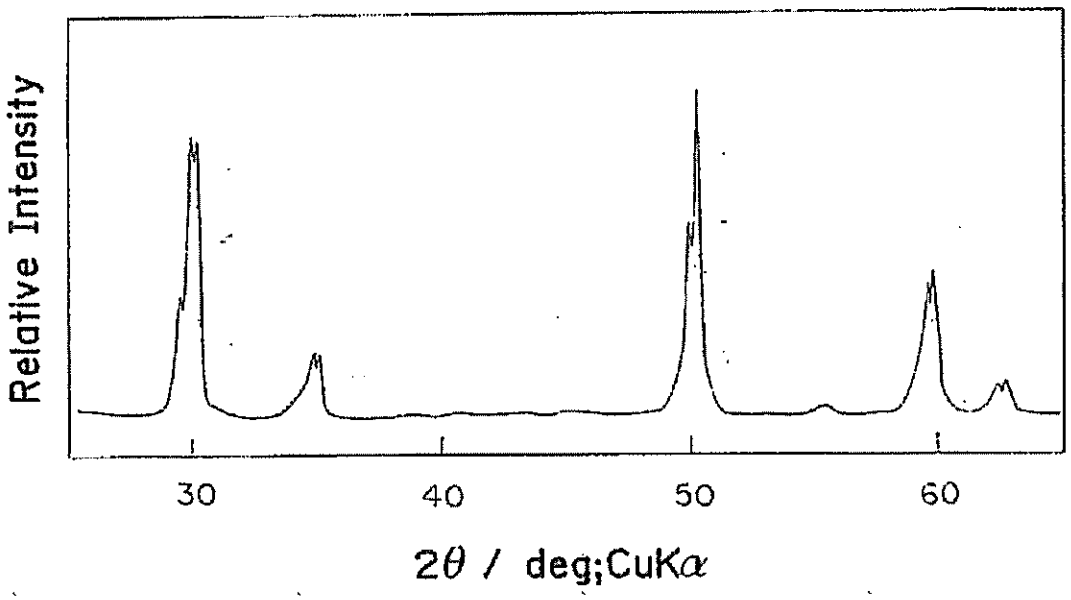

Figure. 2.5. X-ray-diffraction pattern of the substrate of Fig. 2.4(a).

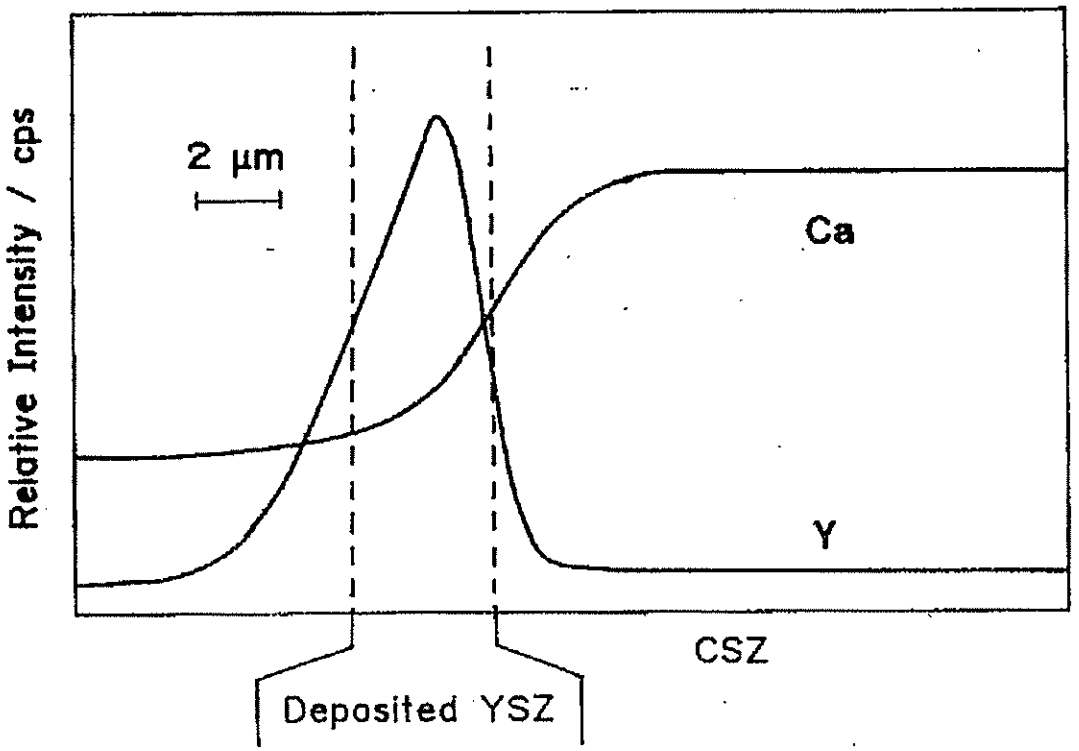

Figure. 2.6. Depth profile of Ca and Y in the YSZ film deposited on CSZ substrate.

Figure. 2.7. SEM micrograph of (a) fracture cross section and (b) surface of YSZ thin film on CSZ.

Chapter 3. Preparation of Thin Yttria-stabilized Zirconia Films by Vapor-phase Electrolytic Deposition

3.1. Introduction

The fabrication of thin layers of ionically conductive oxides such as stabilized zirconia is important for the successful development as an electrolyte for various electrochemical devices, e.g. SOFCs [1,2], sensors [3], and steam electrolyzers [4]. Ionic conductivities of stabilized zirconia are typically 1-50x 10^{-2} S cm^{-1} at 1000° C. For its practical application to electrochemical devices as an electrolyte, it is necessary to decrease its operating practical resistance. Thin films will meet this requirement. It is not easy, however, to form a thin pinhole-free (gastight) stabilized zirconia film with a high reliability. A number of technologies have been devised and investigated to produce thin films of stabilized zirconia. These include CVD [5-7], plasma-spraying [8,9], RF-sputtering [10,11], and electrochemical vapor deposition (EVD) [12,13]. However, each of these technologies has difficulty; pore and void formation in the deposited film, slow depositions rate, damage on the substrate, or others.

We have been developed a new technique, vapor-phase electrolytic deposition (VED) [14] in order to prepare uniform ionically conductive oxides. In this work, we report on an application of the VED method to preparation of gas tight thin films of ionically conductive oxides [yttria-stabilized zirconia (YSZ)] on a porous substrate. The principle of VED, which has been described in detail in a previous report [14], is an electrolysis using low temperature plasma as a conductive fluid.

The VED technique is resembling the EVD method. Fig. 3.1 shows the principle of the EVD and the VED. In the EVD (Fig. 3.1a), the motive force for the reaction is dependent on the difference in the oxygen activity at the two gaseous phases which contact the growing YSZ film [12,13]. This activity difference causes a potential field, which accelerate the transport of oxide ion, O^{2-}, through the growing oxide. This movement disturbs the electro-neutrality in the oxide and leads to charge distributions. In order to keep the electro-neutrality inside the YSZ layer, electron must move to the reverse direction against the unfavorable potential field to keep the oxide growth. At the steady state, the magnitude of two fluxes directing reverse directions to each other has to be equal. Therefore, in the EVD process, the deposition rate is determined by an electron flux in the oxide layer. Therefore, it is difficult to control the deposition rate.

In addition to electron and oxide ion, metal cation and positive hole may contribute to the electric conduction. In the case of high oxygen partial pressure, positive holes (h) are produced by following eq. (3.1) [15]:

$$O_2 + 2V_O^{\cdot\cdot} = 2O_O + 4\mathrm{h} \qquad (3.1)$$

where $V_O^{\cdot\cdot}$ is the oxygen vacancy. In the system adopted in this work, oxygen partial pressure is relatively low, so positive hole conduction is inferred to do only a minor contribution. On the other hand,

electron conduction appears in the low oxygen partial pressure region by following eq. (3.2) [15]:

$$2O_O = O_2 + 2V_O^{\cdot\cdot} + 4e \qquad (3.2)$$

However, since the flux of electron is still low under the conditions of low oxygen partial pressure, electron conduction is rate limiting step of the EVD process [16].

Furthermore, cations may contribute to the conduction in the oxide. The diffusion coefficients of metal cations are 10^5 times smaller than that of oxide anion at 2000°C [17]. At 1000°C, the difference becomes much larger, so the transportation of metal cation is not important.

On the other hand, in the VED (Fig. 3.1b), the electron transport through the growing film is not required and motive force for the oxide ion transport, i.e., the potential field throughout the growing oxide, is supplied by an applied dc bias voltage. The dc current density will give the magnitude of the oxide ion (O^{2-}) flux through the oxide film which corresponds to the deposition rate of the oxide layer. If electron conduction participates to the same direction to some extent, the current efficiency will decrease.

However, in the VED, the reactor becomes more complicated than that for EVD and sputtering of the growing film might take place due to high energy particles formed in the plasma.

3.2. Experimental

3.2.1. Materials

Anhydrous $ZrCl_4$ (Wako Chemical Company, extra pure grade) and anhydrous YCl_3 (Aldrich Chemical Company, extra pure grade) were used without further purification. A porous calcia-stabilized zirconia (CSZ) tube (Nippon Kagaku Togyo Co., Ltd, 3 mm thickness, 13 mm outer diameter, 3 cm length, 28% porosity) was used as a substrate. Platinum paste (Tokuriki Chemical Laboratory, No. 8103) was used for deposition of porous platinum electrode on the porous CSZ substrate.

3.2.2. Vapor-phase electrolytic deposition (VED)

The apparatus used for the VED has been described in the previous paper [14]. Since a porous CSZ tube deposited with porous platinum electrode on its outer surface was used as a substrate in this work, the apparatus was slightly modified for attachment of the porous substrate. A schematic diagram of the part of an apparatus for depositing YSZ film by VED is shown in Fig. 3.2. The reactor was constructed of two tubes, which were evacuated separately to prevent source gases from mixing. The $ZrCl_4$ and YCl_3 vapors were introduced in the outer quartz glass tube. Source chlorides, $ZrCl_4$ and YCl_3, were heated separately at the fixed temperature, 280°C and 820°C, respectively. Ar gas (50 cm^3(STP) /min) was introduced in the outer quartz glass tube as a carrier gas of the source chlorides, Ar gas (10 cm^3(STP)/min) saturated with H_2O at 10°C was introduced in the inner alumina tube. The reactor chamber containing the substrate, which was cemented at the middle of the alumina tube, was maintained at 1100°C.

RF power (13.56 MHz) was applied between two inner electrodes (El and E2) to generate low temperature plasma. This low temperature plasma behaves as a conductive fluid. Dc bias between the grounded electrode (E2) and the porous platinum electrode deposited on the porous CSZ substrate (E3) was applied to impel the electrochemical processes in the vapor phase. In this case, conductivity between E2 and E3 was sustained by the low temperature plasma.

When the porous platinum electrode deposited on the porous CSZ substrate was not covered with the YSZ layer, the dc current between E2 and E3 was carried mainly by electrons in the plasma. As the result, the YSZ layer did not grow. It was necessary preceding to application of the dc voltage to cover the porous electrode (E3) with an electronically nonconductive film for the film growth by a VED process.

At the first step, a CVD process was carried out without applications of RF power and dc bias in order to close pores of E3 and to cover E3 with YSZ layer. In the CVD process, $ZrCl_4$ and YCl_3 were directly contacted with H_2O and they react each other (eqs. (3.3) and (3.4)) to form YSZ film.

$$ZrCl_4 + 2H_2O = ZrO_2 + 4HCl, \quad (3.3)$$

$$YCl_3 + 3H_2O = Y_2O_3 + 6HCl\ . \quad (3.4)$$

At the next step, RF power of 100 W were supplied between E 1 and E2 and dc bias of 65 V was applied between E2 and E3 (negative). The VED was carried out under these conditions at a pressure of 2.5 Torr in the outer compartment in order to easily generate low temperature plasma.

3.2.3. Measuring techniques

The ionic conductivities of the YSZ film were determined from ac impedance measurements carried out using a vector impedance meter. A thin layer of platinum was deposited on the YSZ thin film in order to carry out ac impedance measurement. The surface and fracture cross-section of the YSZ film were observed by scanning electron microscope (Hitachi S-51).

X-ray diffraction measurements were performed with a Shimadzu model XD-5A.

3.3. Results and discussion

3.3.1. Preparation of YSZ thin films by the CVD process

The CVD process was carried out at various pressure in the outer compartment without RF power and dc bias. The pressure in the outer compartment was changed and the surface of the porous platinum electrode (E3) was examined by SEM.

Fig. 3.3 shows scanning electron micrographs of the surface of (a) the porous CSZ substrate deposited with porous platinum electrode and (b) the product *at* 2 Torr in the outer compartment for two hours. Observation of the micrograph of Fig. 3.3b reveals that the surface is still porous and that the base porous platinum electrode was not covered completely by YSZ. In the lower range of the pressure (below 1.5 Torr), the product of CVD was not observed.

In the CVD process, the pressure difference on either side of the substrate is very important. In the case that the inner pressure of the substrate was very high, no deposition of porous films was obtained. It is necessary to keep the pressure difference to be almost zero in the CVD process.

Fig. 3.4 shows the scanning electron micrographs of the surface and fracture cross-section of YSZ film prepared by CVD method at 5 Torr in the outer compartment for two hours. Under these conditions, the pressure difference between inner and outer side of the porous substrate was small and a YSZ film was deposited on the outer surface of the substrates, because H_2O diffuses in the pore of the substrate faster than the chlorides [13]. In the system of $ZrCl_4$ - YCl_3 - H_2O under atmospheric pressure using quartz glass as substrates, YSZ films prepared by CVD had an orientation that (100) plane was parallel to the surface of the substrate [6]. From the micrographical view of the surface, the crystal did not have any preferential orientation and the Pt electrode was covered well by YSZ layer. It was also confirmed by X-ray diffraction.

Without dc bias, deposition by the EVD process had to take part in the film growth. The film thickness was about 3 μm. Therefore, the deposition rate of YSZ film by CVD-EVD process in this condition was estimated to be 1.5 μm h^{-1}.

3.3.2. Preparation of YSZ thin films by the VED process

YSZ films were prepared using the VED method. At first Pt electrode was covered by YSZ film by the CVD-EVD process at 5 Torr of the outer compartment as described above for one hour. Next dc voltage was applied between electrodes E2 and E3 under RF plasma generation at 100 W and YSZ grew by the VED process. At this step pressure was reduced to 2.5 Torr because the RF plasma was not stable at 5 Torr.

Scanning electron micrographs of YSZ film deposited by successive CVD-EVD (1 h) and VED (1.5 h) processes are shown in Fig. 3.5. The surface morphology was not so different from the ones obtained by the CVD-EVD process. However, it looks that the surface of Fig. 3.5 seems to be smoother than that of Fig. 3.4. The grain size was about 5 μm. From the cross-section view, film thickness was about 12μm. Therefore, the deposition rate by VED process was 7 μm h^{-1} assuming that the thickness of deposited YSZ film by the CVD-EVD process at 5 Torr for one hour prior to VED was 1.5 μm h^{-1}. These facts indicate that the deposition rate of the VED process is about 4 times faster than the CVD-EVD process under present conditions.

Fig. 3.6 is an X-ray diffraction pattern of the deposited film. The X-ray diffractions of cubic zirconia and Pt porous electrode were identified. Due to the large thickness of the porous platinum layer of about 30 μm, the X-ray diffraction peak of the porous CSZ tube of the substrate was not detected. This fact indicates that the thin film prepared by VED method is yttria-stabilized zirconia. Furthermore, ESCA spectra showed that the YSZ contained about 7-9% Y_2O_3.

Fig. 3.7 exhibits plots of conductivity of YSZ films prepared by the VED method (a) together with a

sintered pellet (b) [18] against temperature. Conductivity values were calculated from ohmic resistance without correction of ohmic drop at electrode and lead wire. Conductivity values were very close to ones of sintered pellet. From the slope of the plot, activation energy was calculated to be 19.3 Kcal/mol.

Gas (Ar) leak was examined by applying the pressure difference of 500 mm H_2O between inside and outside of the YSZ thin film and gas permeating the YSZ films was measured by a gas flow meter using a soap film. The gas leak was not detected. (Its detection limit was estimated to be 10^{-12}-10^{-13} m^2 s^{-1} Pa^{-1}.) This result indicates the YSZ thin film was pinhole-free.

3.4. Conclusion

VED method is found to be capable and applicable for preparing YSZ films. The deposited film is pinhole-free and exhibited the conductivity comparable to that of the sintered YSZ. The deposition rate is still low, but it is expected to be accelerated by optimizing the plasma conditions, applied dc bias, and the reactor construction. Further, this technique will be applied to other oxide systems where the products are ionically conductive under preparation conditions.

Acknowledgement

This work was supported by Grant-in-aid for Scientific Research from the Ministry of Education, Science and Culture in Japan (Grant No. 02203114).

REFERENCES

[1] N.J. Maskalick and C.C. Sun, *J. Electrochem. Soc.* **118** 1386 (1971).

[2] A.O. Isenberg, *Solid State Ionics* **3/4** 431 (1981).

[3] Y. Miyahara, K. Tsukada and H. Miyagi, *J. appl. Phys.* **63** 2431 (1988).

[4] E.J.L. Schouler, M. Kleitz, E. Forest, E. Fernandez and P. Fabry, *Solid State Ionics* **5** 559 (1981).

[5] J. Minet, F. Langlais and R. Naslain, *J. Less-Common Met.* **132** 273 (1987).

[6] H. Yamane and T. Hirai, *J. Crystal Growth* **94** 880 (1989).

[7] Y. Takahashi, T. Kawae and M. Nasu, *J. Crystal Growth* **74** 409 (1986).

[8] G. Chiodelli, A. Magistris, M. Scagliotti and F. Parmigiani, *J. Mater. Sci.* **23** 1159 (1988).

[9] M. Scagliotti. F. Parmigiani, G. Samoggia, G. Lanzi and D. Richon, *J. Mater. Sci.* **23** 3764 (1988).

[10] A. Negishi, K. Nozaki and T. Ozawa, *Solid State Ionics* **3/ 4** 443 (1981).

[11] N. Nakagawa, H. Yoshioka, C. Kuroda and M. Ishida, *Solid State Ionics* **35** 249 (1989).

[12] I. O. Isemberg, ECS Symp. Electrode Materials, Processes Energy Conver. Storage **77-6** 572 (1977).

[13] M.F. Carolan and J.N. Micheals, *Solid State Ionics* **25** 207 (1987).

[14] Z. Ogumi, Y. Tsuji, Y. Uchimoto and Z. Takehara, *J. Appl. Phys.* **72** 1577 (1992).

[15] K. Kiukkola and C. Wagner, *J. Electrochem. Soc.* **104** 379 (1957).

[16] U.B. Pal and S.C. Singhal, in: Proc. First Intern. Symp. on SOFC **89-11** 41 (1989).

[17] W.H. Rhodes and R.E. Carter, *J. Am. Ceram. Soc.* **49** 244 (1966).

[18] J.M. Dixon, L.D. Lagrange, U. Merten, C.F. Miller and J.T. Porter, *J. Electrochem. Soc.* **110** 276 (1963).

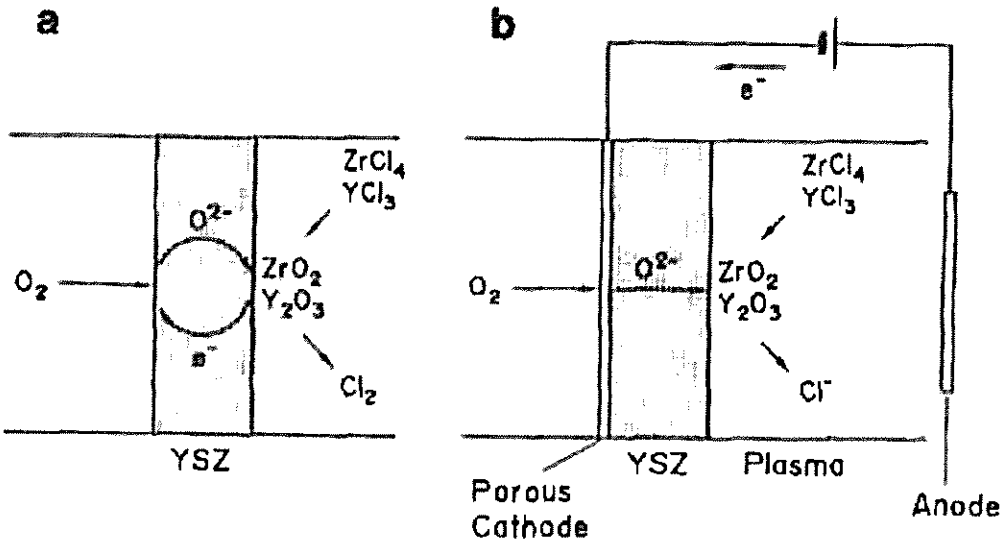

Fig. 3.1. Principles of electrochemical vapor deposition (EVD) and vapor-phase electrolytic deposition (VED)

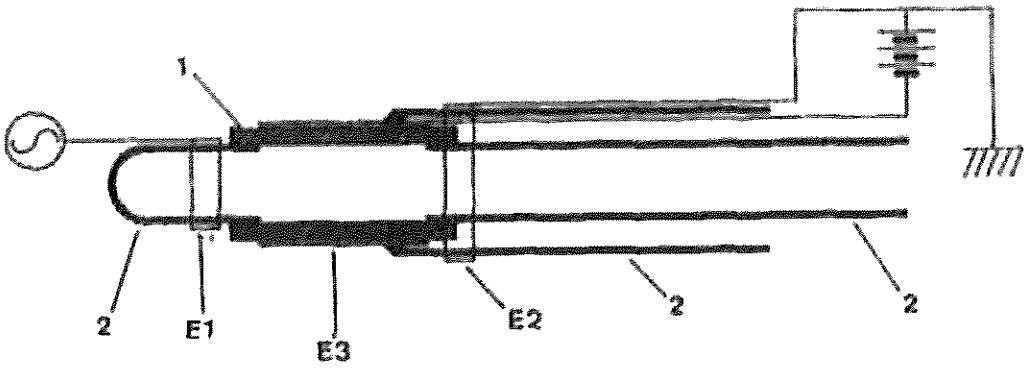

Fig. 3.2. A schematic diagram of the parts of apparatus for VED method using porous CSZ tube as a substrate: 1, porous CSZ tube; El, RF electrode: E2, grounded electrode (anode for dc); E3, porous platinum electrode (cathode for dc); 2, alumina tubes.

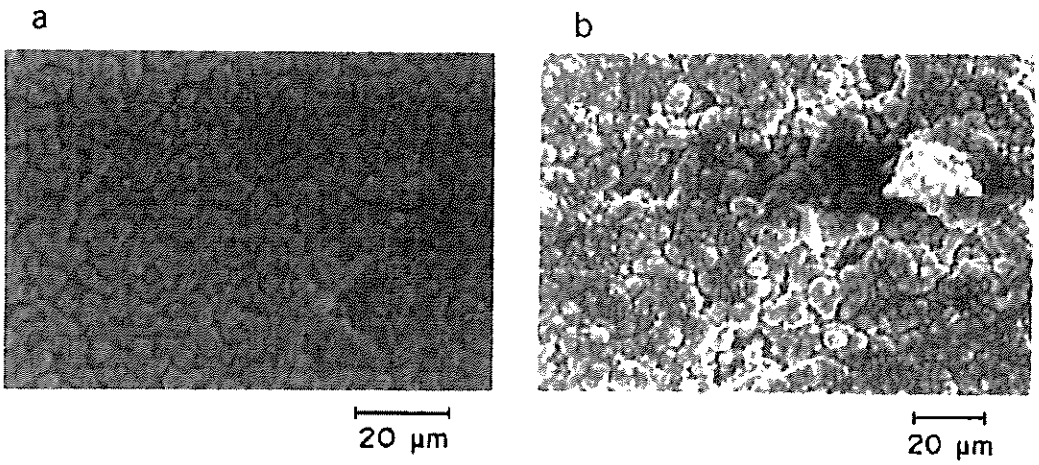

Fig. 3.3. Scanning electron micrographs of surface of (a) porous CSZ substrate deposited with platinum and (b) the substrate after CVD process at 2 Torr in outer compartment for two hours.

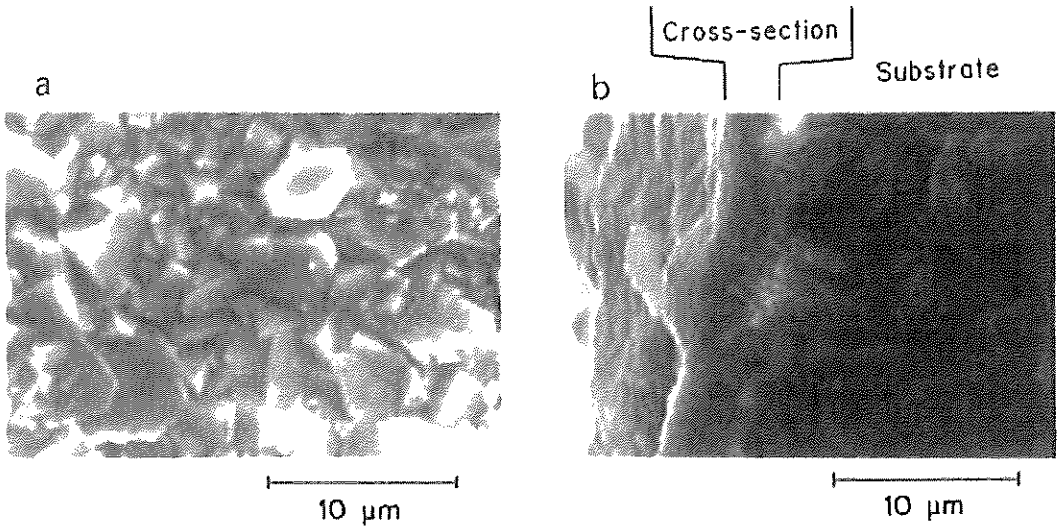

Fig. 3.4. Scanning electron micrographs of (a) surface and (b) fracture cross-section of porous CSZ substrate deposited with platinum after CVD process at 5 Torr in outer compartment for two hours.

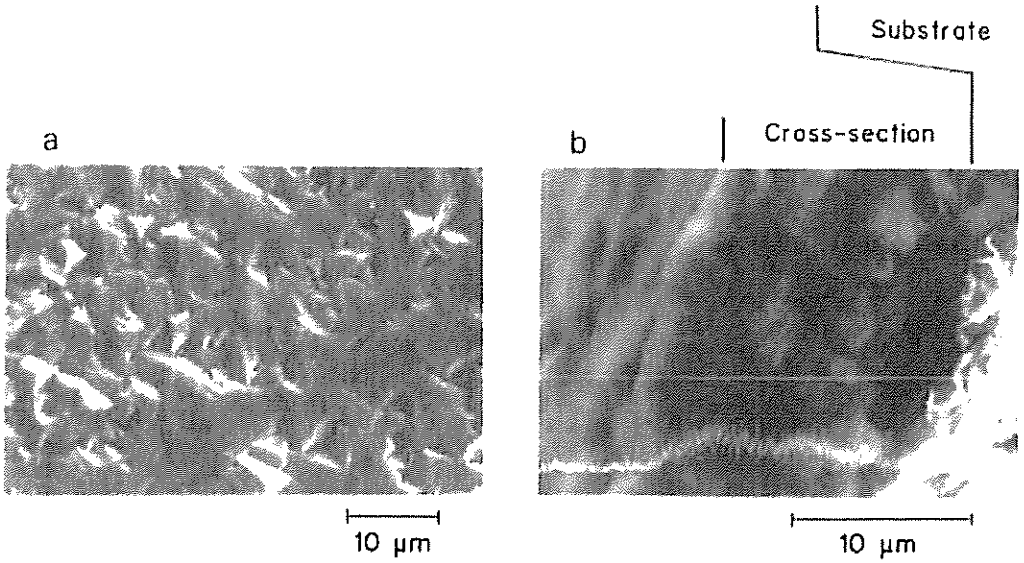

Fig. 3.5. Scanning electron micrographs of (a) surface and (b) fracture cross-section of the porous CSZ substrate deposited with platinum after VED process (Zr X-ray line is also shown).

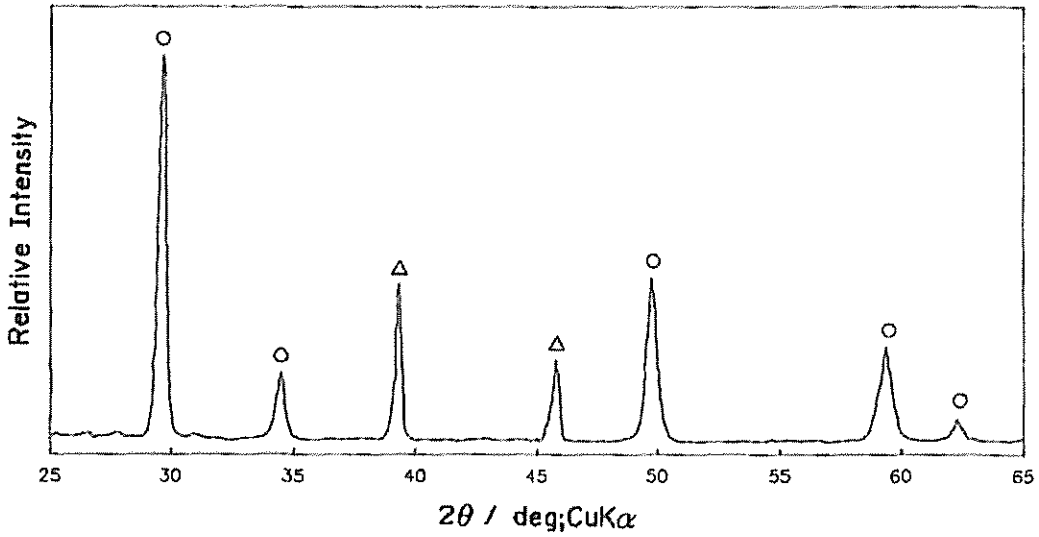

Fig. 3.6. X-ray diffraction patterns of porous CSZ substrate deposited with platinum after VED process: (○) stabilized zirconia; (△) platinum.

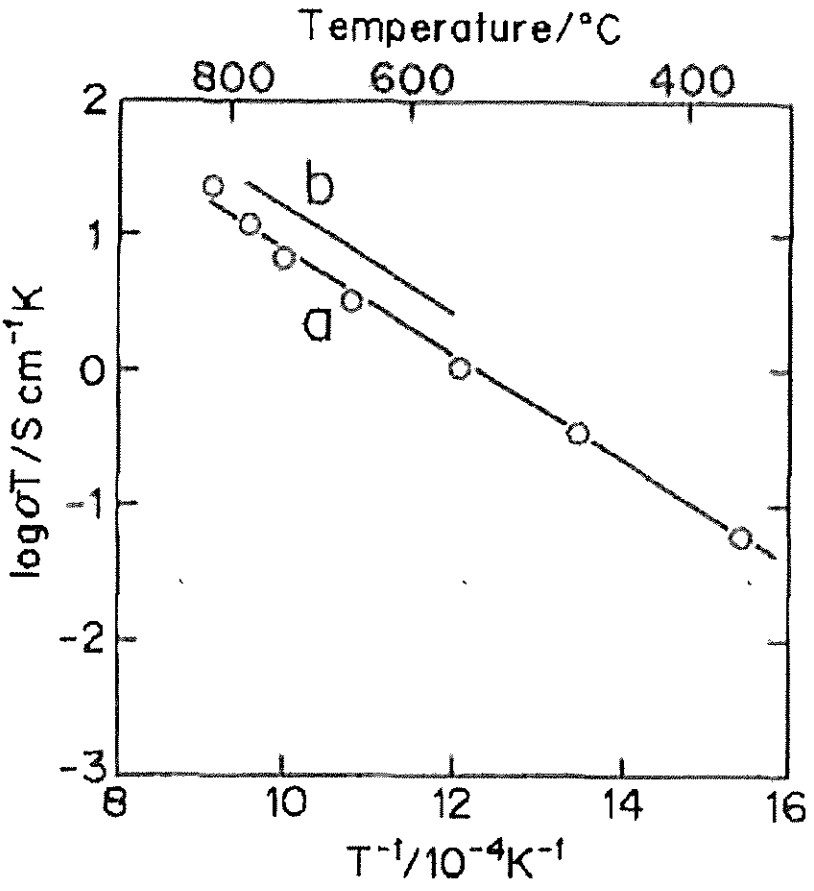

Fig. 3.7. Temperature dependence of conductivity of YSZ films: (a) YSZ thin film prepared by VED method; (b) YSZ (7 mol% Y_2O_3) by ref. [18].

Chapter 4. Investigation of Cathodic Reaction in Solid Oxide Fuel Cells by Operando X-Ray Absorption Spectroscopy

4.1. Introduction

High temperature electrochemical devices using solid-state ionic conductors, such as solid oxide fuel cells (SOFCs), gas sensors and electrochemical gas separation systems, have been intensively investigated during the last decades from their industrial and environmental importance [1-4]. To effectively improve and optimize the performance of these devices, it is essential to understand their electrode reaction mechanism. The electrochemical reactions of gases at elevated temperatures are considered to be rate-controlled, in many cases, by reactions at the electrode surface, such as adsorption and/or dissociation of gases [3,5,6]. However, this rate-determining step has not been directly observed by electrochemical experiments and remains a matter of scientific discussion. One main reason for the poor understanding of high-temperature electrochemical reactions is that conventional analytical techniques, including electrochemical methods such as current-voltage measurements and AC impedance measurements, can provide only indirect and phenomenological information. Thus, it is crucial to develop in situ and *operando* analytical techniques that allow direct observation of the physical/chemical states of electrodes and electrolytes under the operating conditions. To this end, in situ spectroscopic studies have been performed since 2000 to investigate high-temperature electrochemical reactions [7-10]. Although some studies successfully observed the physical/chemical states of electrodes and electrolytes, the reaction mechanisms could not be directly clarified because the applied analytical techniques required impractical experimental conditions (e.g., high-vacuum conditions) or provided only limited information. Recently, X-ray diffraction [11] and X-ray absorption techniques [12,13] have been used to analyze cathode reactions in high-temperature and high-voltage applications. When hard X-rays with energy of >5000 eV are used, the measurements do not require any specific experimental conditions, e.g., high vacuum and low temperature; thus, X-ray based techniques are considered to be suitable for in situ analysis of high-temperature electrochemical devices. However, each study focused on a representative electrode material and identified surface reactions as the rate-determining step. Although some impedance studies reported oxide ion diffusion as a rate-limiting step under high oxygen partial pressure for Sr-doped $LaMnO_3$ [14-16] and $LaNi_{0.6}Co_{0.4}O_{3-\delta}$, [17] no study has shown that diffusion was the rate-limiting step by using spectroscopic methods. To our knowledge, spectroscopic data on surface-limited and diffusion-limited reactions have not yet been compared.

This study examines three representative cathode materials used in SOFCs by *operando* X-ray absorption spectroscopy (XAS). Dense thin-film electrodes of $La_{0.6}Sr_{0.4}CoO_{3-\delta}$ (LSC) on a $Ce_{0.9}Gd_{0.1}O_{1.95}$ (GDC) electrolyte, $La_{0.6}Sr_{0.4}Co_{0.8}Fe_{0.2}O_{3-\delta}$ (LSCF) on a $Y_{0.1}Ce_{0.9}O_{1.95}$ (YDC) electrolyte, and $La_{0.9}Sr_{0.1}MnO_{3\pm\delta}$ (LSM) on a $Zr_{0.92}Y_{0.08}O_{1.96}$ (YSZ) electrolyte are investigated. The

oxygen chemical potential of the cathode films with and without polarization are evaluated directly, and the rate-determining step is clarified.

4.2. Experimental

4.2.1. Preparation of thin-film electrodes

Dense thin-film electrodes of LSC, LSCF, and LSM were prepared by pulsed laser deposition (PLD). Sintered stoichiometric LSC, LSCF, and LSM pellets were used as targets for PLD. GDC, YDC, and YSZ pellets were mirror polished with diamond paste and used as the substrate. PLD of the LSC thin films was performed under an oxygen partial pressure [$p(O_2)$] of 1 Pa at 973 K using a XeCl laser (λ=308 nm, approximately 150–170 mJ cm^{-2}). To prepare the LSCF and LSM thin films, a YAG laser (λ = 256 nm, pulse energy = 0.15 W) was used, and deposition was performed at $p(O_2)$ of 1 Pa and at 1073 K. After the thin films were deposited, the specimens were annealed at $p(O_2)$ of 10^5 Pa for 30 min before cooling. The film thickness was estimated using a stylus surface profiler (Dektak-3).

4.2.2. High temperature electrochemical *operando* XAS apparatus

An *operando* apparatus capable of XAS measurements at elevated temperatures under a controlled atmosphere by applying an electrical current was constructed. Figure 4.1(a) shows a photograph of the apparatus mounted on the beamline at the synchrotron radiation facility. An X-ray beam is passed through an ionization chamber (I_0 detector), which monitors the intensity of the incident beam, and the fluorescent X-rays emitted from a specimen are monitored by a semiconductor detector (I_F detector). The apparatus was placed inside a stainless-steel chamber with Al-deposited Kapton film windows for incoming and outgoing X-rays. An O_2/N_2 gas mixture was introduced into the chamber so that the atmosphere around the specimen was maintained at the desired oxygen partial pressure.

Figure 4.1(b) shows a photograph of the specimen holder and the *operando* electrochemical cell. The specimen was placed on the holder, and a Kanthal heater was placed near the electrochemical cell to heat it to a high temperature. Electrochemical measurements were performed by a three-electrode method using an impedance analyzer and a potentiostat (Solartron 1260 and 1287, respectively). A schematic illustration of the electrode geometry is presented in Fig. 4.2. The counter electrode was a porous composite of the cathode material and platinum, and the reference electrode was porous platinum. All the electrodes were exposed to the same atmospheric conditions.

When a beam of monochromatic X-rays irradiates a sample, both absorption and diffraction of X-rays can occur. To reduce spurious signals due to diffraction, the sample orientation was averaged over time [18]. For this purpose, the specimen holder was continuously oscillated along two perpendicular axes, both perpendicular to the incident beam, by a gimbal mechanism. The specimen

was at the center so that the incident X-rays always struck it. It was confirmed that XAS measurements without diffraction features could be obtained by specimen oscillation.

4.2.3. *Operando* XAS measurements

XAS spectra at Mn, Fe, and Co *K*-edge were measured in a fluorescence mode using synchrotron radiation at beamline BL01B at SPring-8, JASRI, Japan, and beamline 7C at the Photon Factory, KEK, Japan. All *operando* XAS measurements in this study were performed at 1073 K. For the measurements under open-circuit conditions, $p(O_2)$ was controlled between 10 and 10^5 Pa. For the XAS measurements under polarization, an electrical voltage was applied while the $p(O_2)$ value was maintained. Before the XAS measurements began, polarization was applied for 10 min. Considering the reported chemical diffusion coefficients, we expect that steady state was reached at the retention time before the XAS measurements. Therefore, all the results of this study were obtained at steady state. The electrolyte resistance was evaluated by AC impedance analysis, and the overpotential was calculated as the difference between the applied electrical voltage and the *IR* drop due to the electrolyte resistance. This paper discusses small absorption edge shifts depending on $p(O_2)$ and the overpotential. Therefore, to support the accuracy of the edge energy, we confirmed that the position of the absorption edge for Co metal was constant during the beamtime.

4.3. Results and discussion

4.3.1. *Operando* XAS measurements

To discuss the rate-limiting step for the cathodic reaction of oxygen gas in an SOFC, the model electrode must be dense to avoid the effects of the morphology of porous electrodes [5]. The prepared LSC, LSCF, and LSM thin films contained a single phase, as confirmed by X-ray diffraction analysis (Figs. S4.1–S4.3). Scanning electron microscopy images showed that each thin film was dense, and the thicknesses of the LSC, LSCF, and LSM films were estimated to be approximately 400, 300, and 80 nm, respectively (Figs. S4.4–S4.6).

The XAS results provide information about the oxygen chemical potential of the electrodes, which can indicate the rate-limiting step of the cathodic reaction of oxygen gas. Figure 4.3(a) shows the Co *K*-edge X-ray absorption near-edge structure (XANES) for the LSC thin-film electrode under open-circuit conditions at 1073 K as $p(O_2)$ was varied from 10 to 10^5 Pa. The absorption edge clearly shifted toward higher energy with increasing $p(O_2)$. This behavior is consistent with the result of ex situ Co *K*-edge XANES of $La_{0.6}Sr_{0.4}CoO_{3-\delta}$ annealed under various $p(O_2)$ [19]. The position of the absorption edge is sensitive to the changes in the electronic state of a transition metal atom, which are closely correlated with its average oxidation state, and the edge shifts to a higher energy at a higher average valence [19-22]. Consequently, the results in Fig. 4.3(a) show that the average effective charge on Co increased with increasing $p(O_2)$. $La_{1-x}Sr_xCoO_{3-\delta}$ is known to exhibit oxygen deficiency depending on

$p(O_2)$, that is, the oxygen chemical potential (μ_O) [23]. Oxygen deficiency in this oxide is simply interpreted as the formation of oxygen vacancies accompanied by the partial reduction of Co as following Kröger-Vink notation:

$$\frac{1}{2}O_O^{\times} + Co_{Co}^{\bullet} \leftrightarrow \frac{1}{2}V_O^{\bullet\bullet} + Co_{Co}^{\times} + \frac{1}{4}O_2(g) \tag{4.1}$$

where $O_O^{\times}$, $V_O^{\bullet\bullet}$, $Co_{Co}^{\bullet}$ and $Co_{Co}^{\times}$ denote lattice oxide ions, oxygen vacancies, Co^{4+} and Co^{3+}, respectively. That is, there is a one-to-one correspondence between μ_O and the Co average valence; thus, the variation in the μ_O value of LSC can be evaluated by measuring the shift of the absorption edge in the Co *K*-edge XANES spectra. Based on the relationship between the μ_O value of LSC and the absorption edge energy in the Co *K*-edge XANES spectra, the μ_O value inside the LSC electrode can be directly determined.

Figure 4.3(b) presents the Co *K*-edge XANES spectra under applied electrical voltages at a constant $p(O_2)$ of 10^3 Pa. The absorption edge shifted again depending on the applied voltage. The absorption edge energy decreased when the electrode was cathodically polarized. By contrast, the absorption edge shifted toward higher energy when an anodic potential was applied to the electrode. These results clearly indicate that cathodic and anodic polarization decrease and increase the Co average valence, that is, decrease and increase μ_O inside the electrode, respectively.

4.3.2. Electrochemical reactions on LSC, LSCF, and LSM

To quantitatively discuss the absorption edge shifts under polarization, we consider the μ_O value inside the LSC electrode. The overpotential (η) of an electrode on an oxide ion conductor can be determined by calculating the difference between the μ_O value at the electrolyte/electrode interface ($\mu_{O,int}$) and that in the equilibrium state ($\mu_{O,gas}$) assuming the existence of local equilibrium in the electrode and electrolyte [24].

$$2F\eta = \mu_{O,int} - \mu_{O,gas} \tag{4.2}$$

where F is the Faraday constant. The electrochemical oxygen reduction in SOFCs is considered to occur by several elementary reaction processes such as gas diffusion, adsorption and dissociation, surface/bulk diffusion, and ion transfer, as shown in Fig. 4.4 (a). The μ_O profile of the electrode depends significantly on the process that determines the reaction rate. When surface reactions are the rate-determining step, μ_O changes from $\mu_{O,gas}$ to $\mu_{O,int}$, mainly at the electrode surface, as shown by the solid line (ii) in Fig. 4.4 (b). In this case, μ_O is uniform throughout the electrode; thus, the effective

oxygen potential ($\mu_{O,eff}$) in LSC is equal to $\mu_{O,int}$. When the reaction is rate-controlled by diffusion in the electrode, μ_O gradually changes from $\mu_{O,gas}$ to $\mu_{O,int}$ throughout the electrode, as shown by the line (iii) in Fig. 4.4 (b). In this case, $\mu_{O,eff}$ varies with the applied electrical voltage, but $\mu_{O,eff}$ is higher than $\mu_{O,int}$ and lower than $\mu_{O,gas}$. When charge transfer at the interface between the electrode and electrolyte is the rate-determining step, μ_O changes from $\mu_{O,gas}$ to $\mu_{O,int}$, mainly at the interface, as shown by the line (iv) in Fig. 4.4, indicating that $\mu_{O,eff}$ is equal to $\mu_{O,gas}$ and is independent of the applied electrical voltage.

Figure 4.5 shows the absorption edge energy for the Co *K*-edge as a function of the effective oxygen partial pressure, $p(O_2)_{eff}$. Under polarization, $p(O_2)_{eff}$ is defined as the effective oxygen partial pressure corresponding to the overpotential:

$$p(O_2)_{eff} = \exp\left\{\frac{2\mu_{O,eff}}{RT}\right\} = p(O_2)\exp\left\{\frac{4F\eta}{RT}\right\} \quad (4.3)$$

where R is the gas constant. Under open-circuit conditions ($\eta = 0$), $p(O_2)_{eff}$ is equivalent to $p(O_2)$ in the atmosphere. As shown in Fig. 4.5, the shifts in the absorption edge energy caused by polarization were in fairly good agreement with those caused by the corresponding $p(O_2)$ change under open-circuit conditions. The measured XANES reflects information on the oxygen chemical potential of the entire thin-film electrode without the electrolyte. These results revealed that the change in μ_O due to polarization was generated primarily on the electrode surface [solid line (ii) in Fig. 4.4 (b)]. That is, it was experimentally demonstrated that the electrochemical reaction with the LSC electrode is rate-controlled by surface reactions. Several studies using electrochemical and isotope penetration measurements have suggested that the rate-determining step for an LSC thin-film electrode is surface reactions [5, 25-28]. The results in Fig. 4.5 directly and clearly confirm this suggestion. They also show experimentally that local equilibrium holds in the electrodes of high-temperature electrochemical systems. The concept of local equilibrium is widely accepted [24], although there has been no clear experimental evidence to date. The results reported in this work provide decisive evidence confirming this concept.

LSCF, which is in practical use in SOFC cathodes, also exhibits nonstoichiometry depending on $p(O_2)$ [29-32]. Decreasing the oxygen content of LSCF causes decreases in the Co/Fe mean valence owing to charge compensation. We previously reported XANES and extended X-ray absorption fine structure studies of bulk $La_{0.6}Sr_{0.4}Co_{0.8}Fe_{0.2}O_{3-\delta}$ with various oxygen contents [22]. In that study, we found that the charge was preferentially compensated by changes in the formal valence of Co and that oxygen vacancies appeared selectively around Fe atoms when oxygen vacancies were introduced into $La_{0.6}Sr_{0.4}Co_{0.8}Fe_{0.2}O_{3-\delta}$. The shifts in the Co *K*-edge and Fe *K*-edge XANES spectra in this study (Fig. S4.7) also correspond to the changes in the formal valence of Co and in the ligand environment around

the Fe ions, respectively.

Because the absorption edge shift at the Co *K*-edge corresponds to the change in the oxygen potential of the electrode overall (Fig. 4.6), a similar change under polarizations and under various $p(O_2)$ indicates that the μ_O value under polarization changes significantly at the gas/electrode interface, as shown by (ii) in Fig. 4.4. Therefore, we conclude that surface reactions such as oxygen adsorption or ionization are the rate-determining step for the LSCF/YDC model electrode. This conclusion is also reasonable agreement with the previous study [33], which implied surface reaction limitation in LSCF thin films based on the impedance analysis.

The XANES shift of the LSM electrode under polarization exhibits a trend different from that observed in the XANES shifts of the LSC and LSFC electrodes. Because the absorption edge shift as a function of oxygen nonstoichiometry in LSM has not been reported, we determined the linear relationship between the absorption energy and Mn mean valence (Figs. S4.8 and S4.9). When similar La, Sr, and Mn contents are used, the oxygen nonstoichiometry can be evaluated from the energy shift in the Mn *K*-edge XANES spectra.

The absorption edge shift of the Mn *K*-edge XANES of LSM under electrode polarization and the change in the oxygen potential profile under equivalent oxygen partial pressures (Fig. S4.10) are plotted in Fig. 4.7. The shift of the absorption edge in Fig. 4.7 corresponds to the change in the oxygen chemical potential estimated from the Mn *K*-edge XANES. The shift of the absorption edge under various electrode polarizations differs from the oxygen potential changes under open-circuit conditions. The discrepancy between the results under electrode polarization and under various oxygen partial pressures indicates that under polarization, the oxygen potential changes inside the electrode, as shown by (iii) in Fig. 4.4. This result proves that the rate-determining step for the LSM thin film/YSZ model electrode is oxide ion diffusion in the electrode, which includes bulk and grain boundary diffusion. From the impedance analysis of LSM thin-film electrodes, such diffusion limitation of cathode reaction was also expected [14-16]. On the other hand, when the charge transfer at the electrode/electrolyte interface is rate-controlled as shown in (iv) of Fig. 4.4, the oxygen chemical potential in the electrode is assumed to be equal to the gas phase. In this case, the energy at the absorption edge is assumed to be unchanged by the cathodic polarization.

Because the rate-determining step for the LSM-YSZ model electrode is identified as the diffusion reaction from the absorption energy shift of the Mn *K*-edge XANES under electrode polarization, we can estimate the oxygen potential profile using the oxide ionic and electrical conductivity. Under an oxygen chemical gradient along the *x* axis, the oxide ion fluxes in the LSM p-type semiconductor are expressed as follows: [34]

$$j_{O^{2-}} = -\frac{RT}{8F^2}\frac{\sigma_{O^{2-}} \times \sigma_{h^+}}{\sigma_{O^{2-}} + \sigma_{h^+}}\frac{d\mu_O}{dx} \tag{4.4}$$

where j is the flux and σ is the conductivity of each carrier (O^{2-}: oxide ions, h^+: holes) (see the

Appendix in the supporting information). For the electrical properties of LSM [35], the oxide ionic and electrical conductivity are described by the following equations:

$$\sigma_{O^{2-}} = c_1 p(O_2)^{-\frac{1}{c_2}} \tag{4.5}$$

$$\sigma_{h^+} = const = c_3 \tag{4.6}$$

The total flux is obtained by integrating Eq. (6):

$$j_{O^{2-}}(x) = -\frac{RT}{8F^2}\int_{\ln p(O_2)(0)}^{\ln p(O_2)(x)} \frac{\sigma_{O^{2-}} \times \sigma_{h^+}}{\sigma_{O^{2-}}+\sigma_{h^+}} d\ln p\,(O_2)$$

$$= \frac{RT}{8F^2}\, c_2 c_3 \ln \frac{c_3 + c_1 p(O_2)(x)^{-\frac{1}{c_2}}}{c_3 + c_1 p(O_2)(0)^{-\frac{1}{c_2}}}$$

$$= \frac{RT}{8F^2} c_2 c_3 \ln \frac{\sigma_{tot}(x)}{\sigma_{tot}(0)} \tag{4.7}$$

where $p(O_2)(x)$ is the oxygen partial pressure at a given x, and $\sigma_{tot}(x)$ is the total conductivity corresponding to $c_3 + c_1 p(O_2)(x)^{-\frac{1}{c_2}}$. Therefore, $p(O_2)(x)$, is determined as follows:

$$\frac{x}{L} = \frac{\ln \frac{\sigma_{tot}(x)}{\sigma_{tot}(0)}}{\ln \frac{\sigma_{tot}(L)}{\sigma_{tot}(0)}} \tag{4.8}$$

where $x = 0$ and $x = L$ correspond to the electrode/electrolyte interface and the electrode/gas interface, respectively. For the oxide ionic conductivity of LSM calculated from the oxygen tracer diffusion coefficient by Yasuda *et al* [36] and the oxygen nonstoichiometry reported by Mizusaki *et al.* [37], the oxygen potential profile of the LSM thin-film electrode can be estimated as shown in Fig. 4.8. For this estimation, we set the oxygen potential at $x = 0$ and L to that at the electrode surface and electrode/electrolyte interface, respectively. Most of the differences in $p(O_2)_{eff}$ can be attributed to the change near the electrode/electrolyte interface. Therefore, the oxygen potential profile of the dense LSM electrode under polarization is changed primarily near the electrode/electrolyte interface, as shown in Fig. 4.9. Although this potential profile is not a strict representation owing to the oxygen excess in LSM caused by cation deficiency, the observed result roughly indicates the oxygen potential change under diffusion-limited conditions [35].

All of the experiment was measured at 1073 K, but the effect of temperature variation on the oxygen chemical potential may vary depending on the temperature. When the rate-limiting process does not change, the profile of the oxygen chemical potential remains unchanged and is identical to that shown in Fig. 4.4. However, as shown in Eq. (4.3), the absolute value of the oxygen potential change depends on temperatures, which shifts $\mu_{O,int}$ with temperature. In the case of LSM where oxide ion diffusion is rate-limiting, the potential profile inside electrodes is changed, which depends on the ratio of oxide

ion conduction to hole conduction with temperatures, according to Eqs. (4.7) and (4.8). However, at high-temperature conditions, the temperature dependence is quite small due to the dominance of the hole conduction in LSM.

4.4. Conclusion

We developed a high-temperature electrochemical *operando* XAS technique and applied it to investigate the electrochemical oxygen reduction of a dense thin-film LSC electrode on a GDC electrolyte, an LSCF electrode on a YDC electrolyte, and an LSM electrode on a YSZ electrolyte. The change in the μ_O value of the electrode due to polarization was experimentally clarified; the results demonstrated that local equilibrium was obtained, and surface reactions such as oxygen adsorption or ionization were the rate-determining step for the LSC and LSCF electrodes. By contrast, the rate-determining step for the LSM electrode was the diffusion of oxide ions in the electrode, including bulk and grain boundary diffusion. The oxygen potential profile in the LSM electrode changed mainly near the electrode/electrolyte interface. It was demonstrated that the developed *operando* XAS technique makes it possible to directly correlate the phenomenological behavior of a high-temperature electrode with its chemical states under operating conditions and to provide useful information that was previously inaccessible.

Acknowledgement

This work was supported by the "New Frontiers of Hetero-Interface Modification for High Temperature Application Based on Nanoionics Principles" of MEXT (No. 439), Japan.

REFERENCES

[1] J.B. Goodenough, *Nature*, **404**, 821-823 (2000).

[2] B.C.H. Steele, A. Heinzel, *Nature*, **414**, 345-352 (2001).

[3] S.B. Adler, *Chem. Rev.*, **104**, 4791-4844 (2004).

[4] N. Yamazoe, *Sens. Actuators B Chem.*, **108**, 2-14 (2005).

[5] T. Kawada, J. Suzuki, M. Sase, A. Kaimai, K. Yashiro, Y. Nigara, J. Mizusaki, K. Kawamura, H. Yugami, *J. Electrochem. Soc.*, **149**, E252-E259 (2002).

[6] Y.P. Cao, M.J. Gadre, A.T. Ngo, S.B. Adler, D.D. Morgan, *Nature Comm.*, **10**, 1346 (2019).

[7] M. Rösch, G. Reinhardt, W. Göpel, *Solid State Ionics*, **136-137**, 791-799 (2000).

[8] X. Lu, P.W. Faguy, M. Liu, *J. Electrochem. Soc.*, **149**, A1293 (2002).

[9] B. Luerßen, J. Janek, S. Günther, M. Kiskinova, R. Imbihl, *Phys. Chem. Chem. Phys.*, **4**, 2673-2679 (2002).

[10] T. Murai, K. Yashiro, A. Kaimai, T. Otake, H. Matsumoto, T. Kawada, J. Mizusaki, *Solid State Ionics*, **176**, 2399-2403 (2005).

[11] Q.Y. Lu, B. Yildiz, *Nano Lett.*, **16**, 1186-1193 (2016).

[12] Y. Orikasa, T. Ina, K. Yamamoto, T. Nakao, A. Mineshige, K. Amezawa, T. Kawada, H. Tanida, T. Uruga, Y. Uchimoto, *Electrochemistry*, **82**, 897-900 (2014).

[13] T. Nakamura, R. Oike, Y. Kimura, Y. Tamenori, T. Kawada, K. Amezawa, *Chemsuschem*, **10**, 2008-2014 (2017).

[14] T. Ioroi, T. Hara, Y. Uchimoto, O. Zempachi, Z.-i. Takehara, *J. Electrochem. Soc.*, **144**, 1362 (1997).

[15] J. Fleig, H.-R. Kim, J. Jamnik, J. Maier, *Fuel Cells*, **8**, 330-337 (2008).

[16] G.J. la O', Y. Shao-Horn, *Electrochem. Solid-State Lett.*, **12**, B82 (2009).

[17] R.A. Budiman, Y. Uzumaki, S. Hashimoto, T. Nakamura, K. Yashiro, K.D. Bagarinao, H. Kishimoto, K. Yamaji, T. Horita, K. Amezawa, T. Kawada, *J. Solid State Electrochem.*, **22**, 2227-2235 (2018).

[18] J. Pant, T.M. Hayes, *Rev. Sci. Instrum.*, **65**, 3389-3392 (1994).

[19] Y. Orikasa, T. Ina, T. Nakao, A. Mineshige, K. Amezawa, M. Oishi, H. Arai, Z. Ogumi, Y. Uchimoto, *J. Phys. Chem. C*, **115**, 16433-16438 (2011).

[20] C.H. Booth, F. Bridges, G.H. Kwei, J.M. Lawrence, A.L. Cornelius, J.J. Neumeier, *Phys. Rev. B*, **57**, 10440-10454 (1998).

[21] T. Shibata, B.A. Bunker, J.F. Mitchell, *Phys. Rev. B*, **68**, 024103 (2003).

[22] Y. Orikasa, T. Ina, T. Nakao, A. Mineshige, K. Amezawa, M. Oishi, H. Arai, Z. Ogumi, Y. Uchimoto, *Phys. Chem. Chem. Phys.*, **13**, 16637-16643 (2011).

[23] J. Mizusaki, Y. Mima, S. Yamauchi, K. Fueki, H. Tagawa, *J. Solid State Chem.*, **80**, 102-111 (1989).

[24] J. Mizusaki, K. Amano, S. Yamauchi, K. Fueki, *Solid State Ionics*, **22**, 313-322 (1987).

[25] T. Kawada, K. Masuda, J. Suzuki, A. Kaimai, K. Kawamura, Y. Nigara, J. Mizusaki, H. Yugami, H. Arashi, N. Sakai, H. Yokokawa, *Solid State Ionics*, **121**, 271-279 (1999).

[26] A. Endo, H. Fukunaga, C. Wen, K. Yamada, *Solid State Ionics*, **135**, 353-358 (2000).

[27] A. Ringuedé, J. Fouletier, *Solid State Ionics*, **139**, 167-177 (2001).

[28] S. Miyoshi, A. Takeshita, S. Okada, S. Yamaguchi, *Solid State Ionics*, **285**, 202-208 (2016).

[29] M.H.R. Lankhorst, J.E. ten Elshof, *J. Solid State Chem.*, **130**, 302-310 (1997).

[30] D. Mantzavinos, A. Hartley, I.S. Metcalfe, M. Sahibzada, *Solid State Ionics*, **134**, 103-109 (2000).

[31] M. Katsuki, S. Wang, M. Dokiya, T. Hashimoto, *Solid State Ionics*, **156**, 453-461 (2003).

[32] E. Bucher, W. Sitte, G.B. Caraman, V.A. Cherepanov, T.V. Aksenova, M.V. Ananyev, *Solid State Ionics*, **177**, 3109-3115 (2006).

[33] F.S. Baumann, J. Fleig, H.-U. Habermeier, J. Maier, *Solid State Ionics*, **177**, 1071-1081 (2006).

[34] A. Mineshige, M. Inaba, S. Nakanishi, M. Kobune, T. Yazawa, K. Kikuchi, Z. Ogumi, *J. Electrochem. Soc.*, **153**, A975 (2006).

[35] J. Mizusaki, N. Mori, H. Takai, Y. Yonemura, H. Minamiue, H. Tagawa, M. Dokiya, H. Inaba, K. Naraya, T. Sasamoto, T. Hashimoto, *Solid State Ionics*, **129**, 163-177 (2000).

[36] I. Yasuda, K. Ogasawara, M. Hishinuma, T. Kawada, M. Dokiya, *Solid State Ionics*, **86-88**, 1197-1201 (1996).

[37] J. Mizusaki, *Solid State Ionics*, **52**, 79-91 (1992).

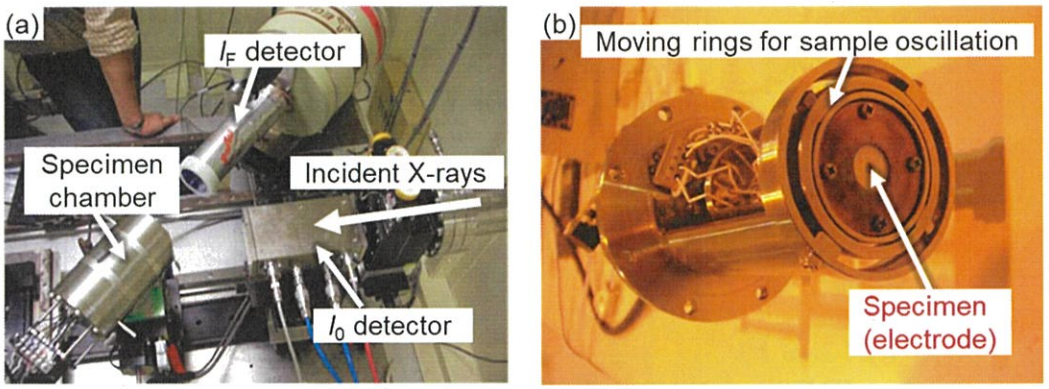

Figure 4.1. High-temperature electrochemical *operando* XAS apparatus: (a) apparatus on the beamline at the synchrotron facility and (b) specimen holder.

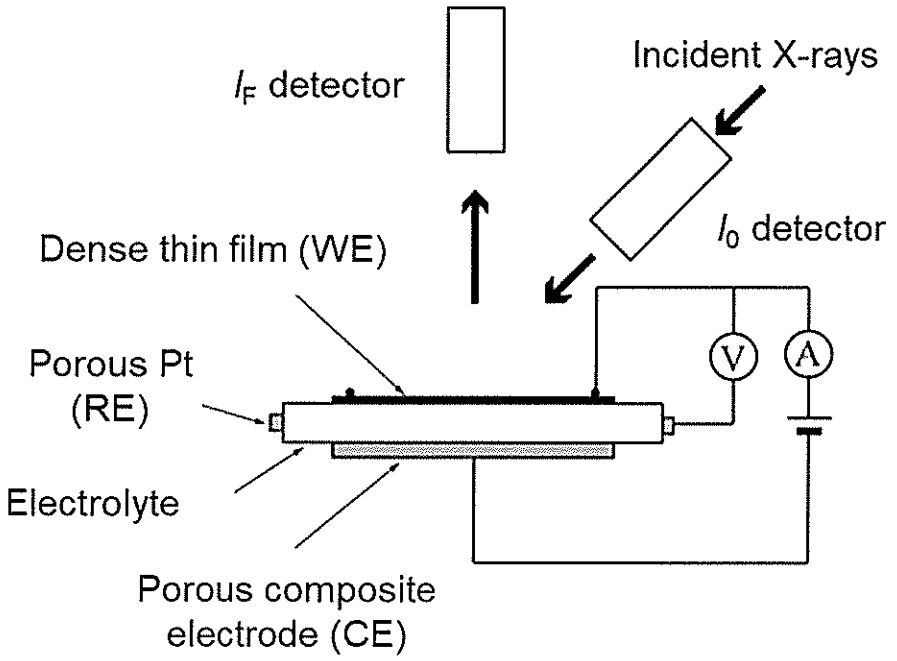

Figure 4.2. Schematic illustration of the electrode geometry in the *operando* electrochemical XAS cell.

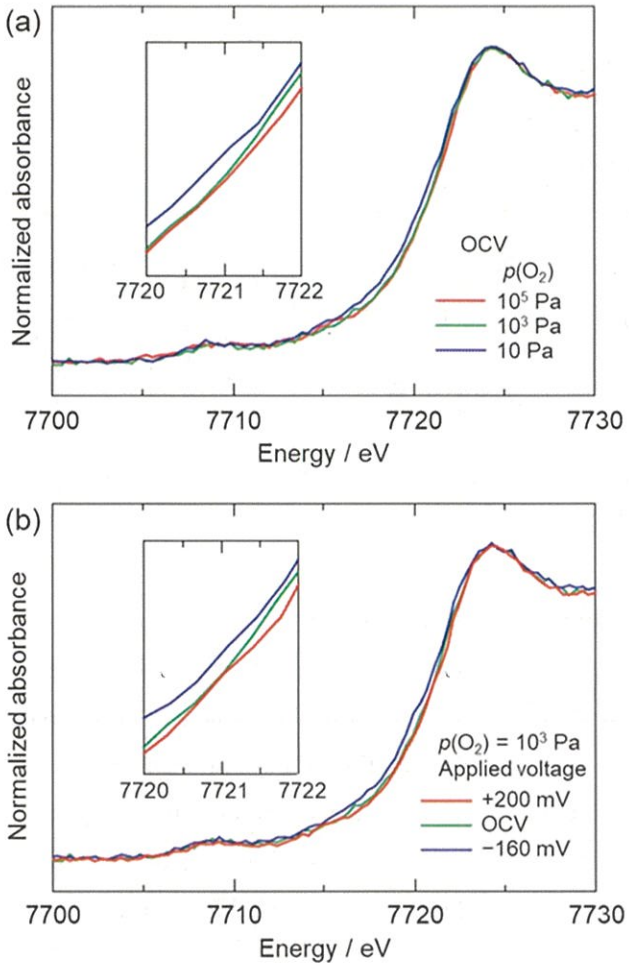

Figure 4.3. *Operando* Co *K*-edge XANES spectra of the dense thin-film LSC electrode on the GDC electrolyte at 1073 K (a) under open-circuit conditions at $p(O_2)$ = 10, 10^3, and 10^5 Pa and (b) under applied voltages of +200, 0 and −160 mV at $p(O_2) = 10^3$ Pa. OCV: Open-circuit voltage.

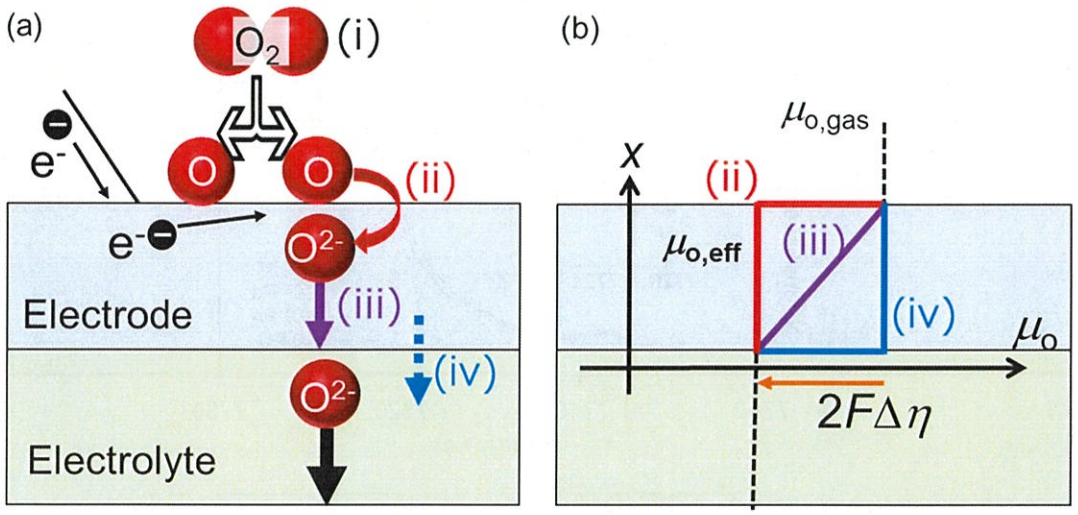

Figure 4.4. (a) Schematic illustration of elementary electrode reactions at the dense electrode/electrolyte interface for oxygen reduction on high-temperature electrochemical devices. The processes (i), (ii), (iii), and (iv) represent gas diffusion, surface reactions, bulk diffusion, and boundary transfer, respectively. (b) Schematic illustration of oxygen chemical potential profiles around dense electrodes. When a voltage is applied to the electrodes, the oxygen chemical potential at the electrode/electrolyte interface shifts. (ii), (iii), and (iv) correspond to the oxygen potential changes when the rate-determining step is surface reactions, bulk diffusion, and boundary transfer, respectively.

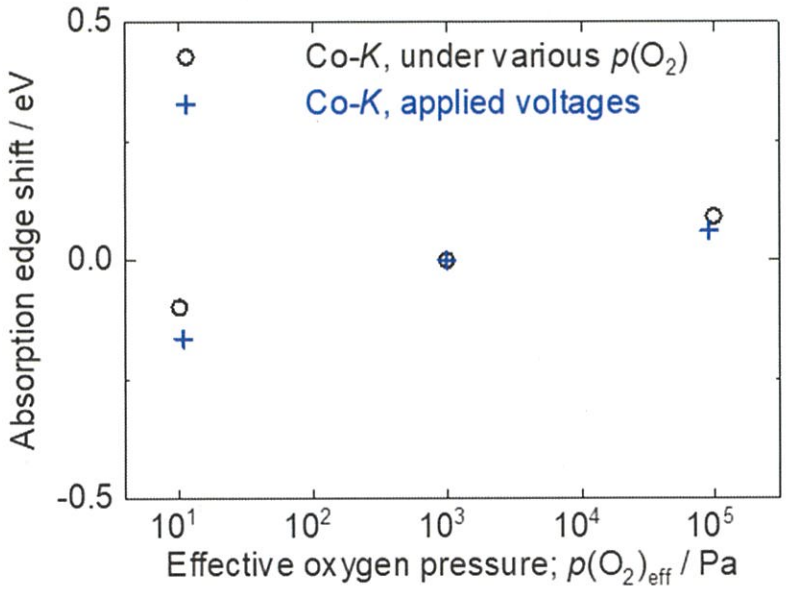

Figure 4.5. Absorption edge shift in Co K-edge XANES spectrum of LSC as a function of effective oxygen pressure at 1073 K. Open circles show the edge energy measured at various $p(O_2)$ under open-circuit conditions. Crosses show the edge energy measured under various applied DC biases at $p(O_2) = 10^3$ Pa.

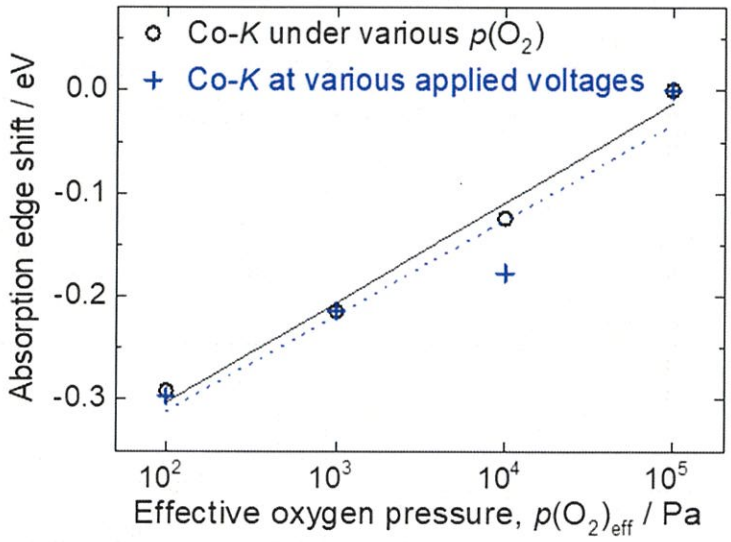

Figure 4.6. Absorption edge shift in Co K-edge XANES spectrum of LSCF as a function of effective oxygen pressure at 1073 K. Open circles show the shift measured at various $p(O_2)$ under open-circuit conditions. Crosses show the shift measured under various applied DC biases at $p(O_2) = 10^5$ Pa.

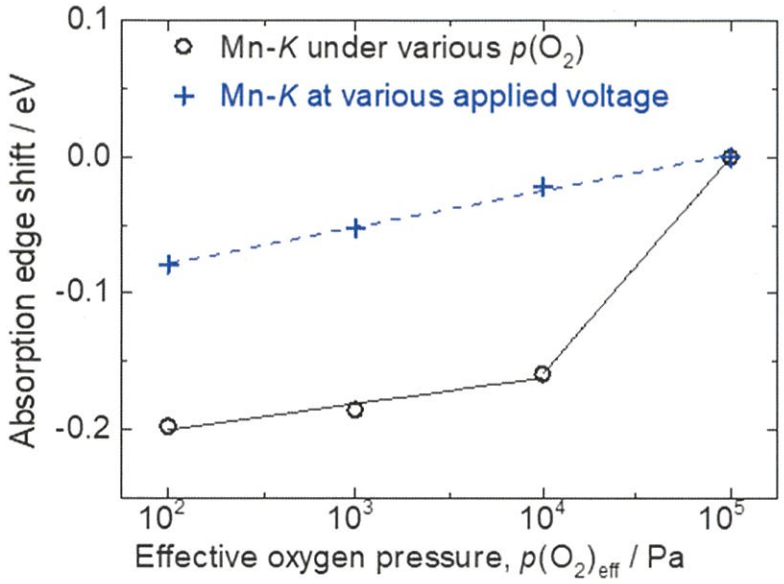

Figure 4.7. Absorption edge shift in Mn *K*-edge XANES spectrum of LSM as a function of effective oxygen potential at 1073 K Open circles show the shift measured under various $p(O_2)$ under open-circuit conditions. Crosses show the shift measured under various applied DC biases at $p(O_2) = 10^5$ Pa.

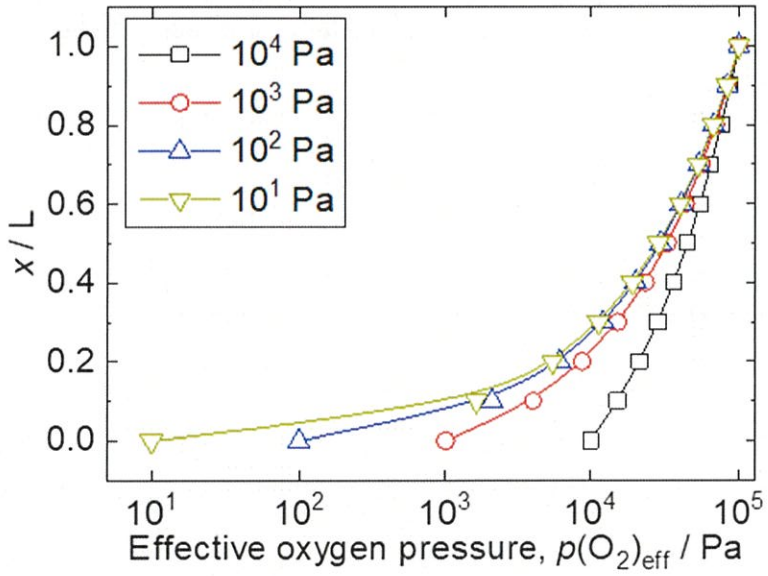

Figure 4.8. Normalized distance from the electrode/electrolyte interface vs. oxygen chemical potential of the LSM thin-film electrode. L and x are the electrode thickness and the position of an arbitrary point on the electrode, respectively. x/L = 1.0 and 0 correspond to the electrode surface and electrode/electrolyte interface, respectively.

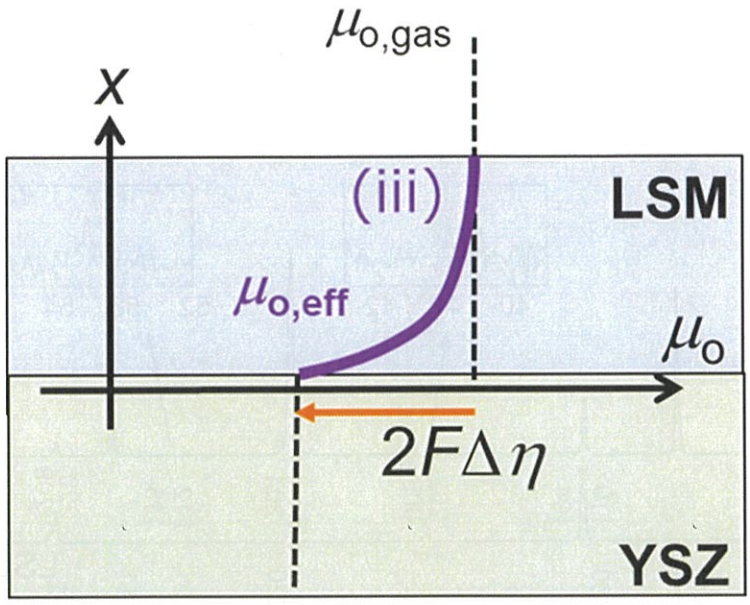

Figure 4.9. Schematic illustration of oxygen chemical potential profiles in the dense LSM cathode on the YSZ electrolyte. When a voltage is applied to the electrode, the oxygen chemical potential exhibits a parabolic profile. (iii) corresponds to the line in Fig 4.4(b).

Supporting Data

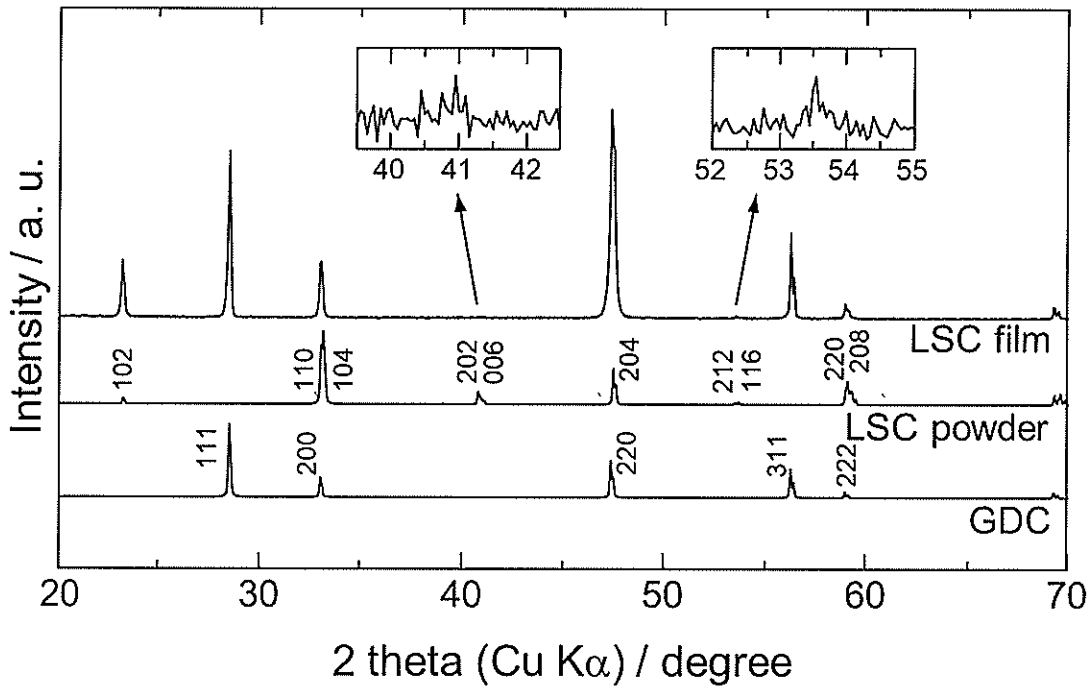

Figure S4.1. X-ray diffraction patterns of the LSC thin-film electrode deposited on the $Ce_{0.9}Gd_{0.1}O_{1.95}$ electrolyte, $La_{0.6}Sr_{0.4}CoO_{3-\delta}$ powder, and $Ce_{0.9}Gd_{0.1}O_{1.95}$.

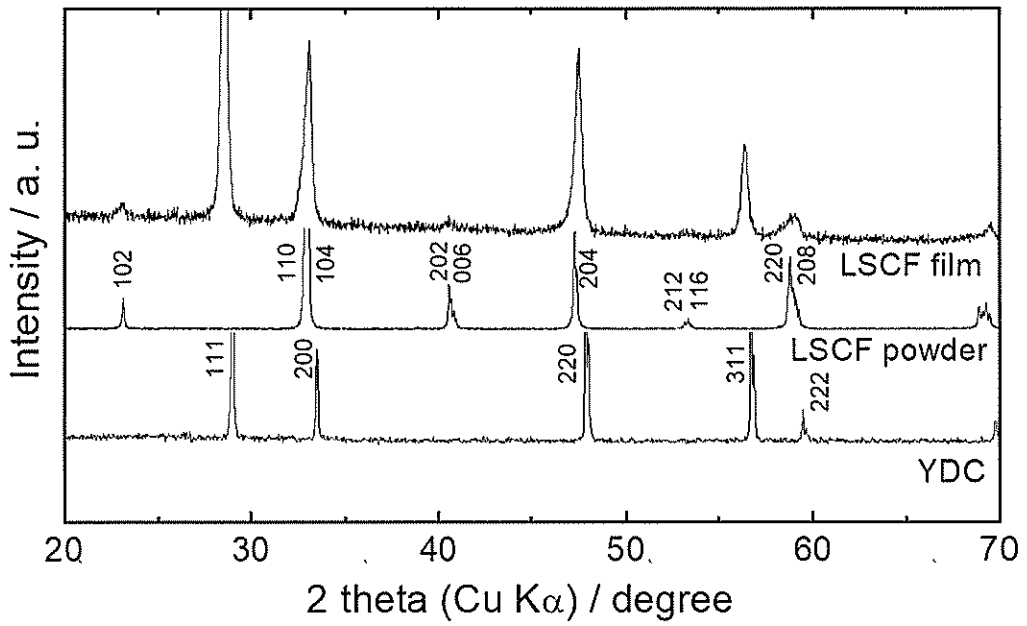

Figure S4.2. X-ray diffraction patterns of the LSCF thin-film electrode deposited on $Ce_{0.9}Y_{0.1}O_{1.95}$, $La_{0.6}Sr_{0.4}Co_{0.8}Fe_{0.2}O_{3-\delta}$ powder, and $Ce_{0.9}Y_{0.1}O_{1.95}$.

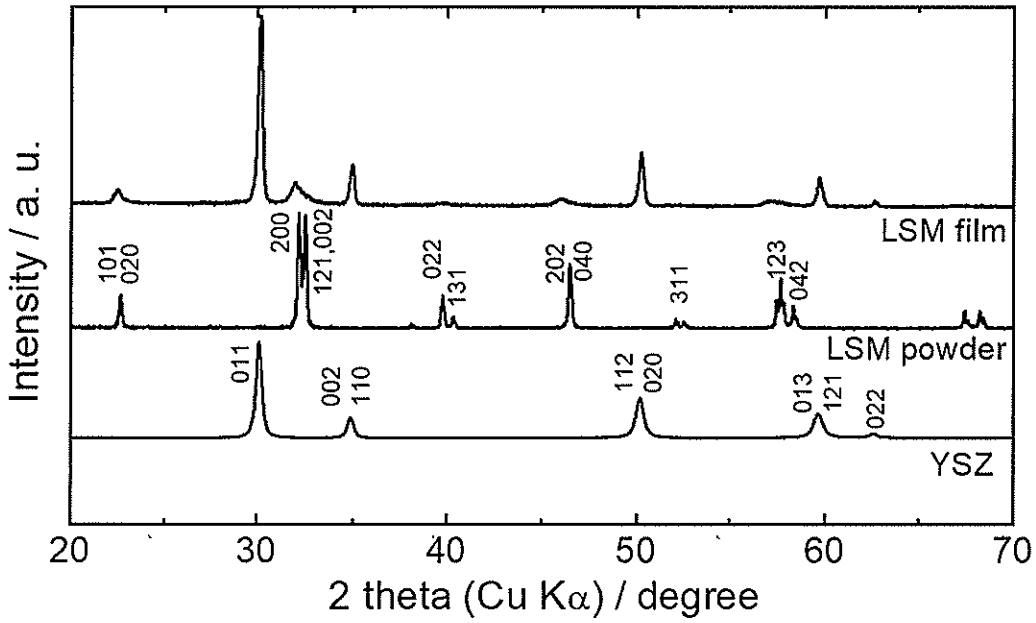

Figure S4.3. X-ray diffraction patterns of the $La_{0.9}Sr_{0.1}MnO_{3\pm\delta}$ thin film deposited on the YSZ substrate, $La_{0.9}Sr_{0.1}MnO_{3\pm\delta}$ powder, and the YSZ.

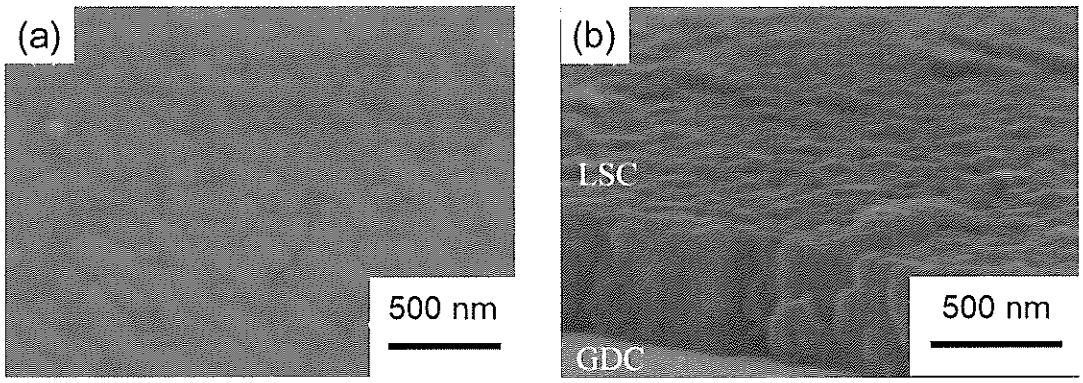

Figure S4.4. SEM images of (a) the surface and (b) the cross section of the LSC thin-film electrode deposited on the $Ce_{0.9}Gd_{0.1}O_{1.95}$ electrolyte.

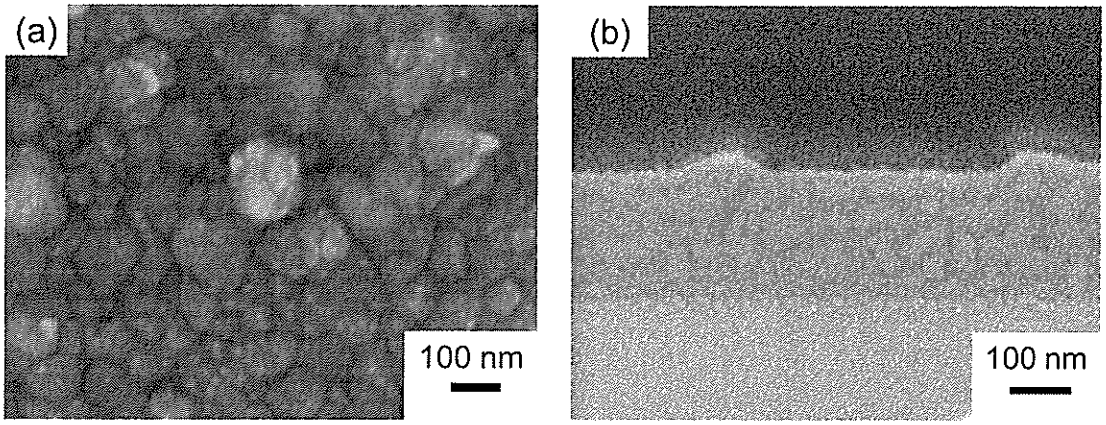

Figure S4.5. SEM images of (a) the surface and (b) the cross section of the LSCF thin-film electrode deposited on the $Ce_{0.9}Y_{0.1}O_{1.95}$ electrolyte.

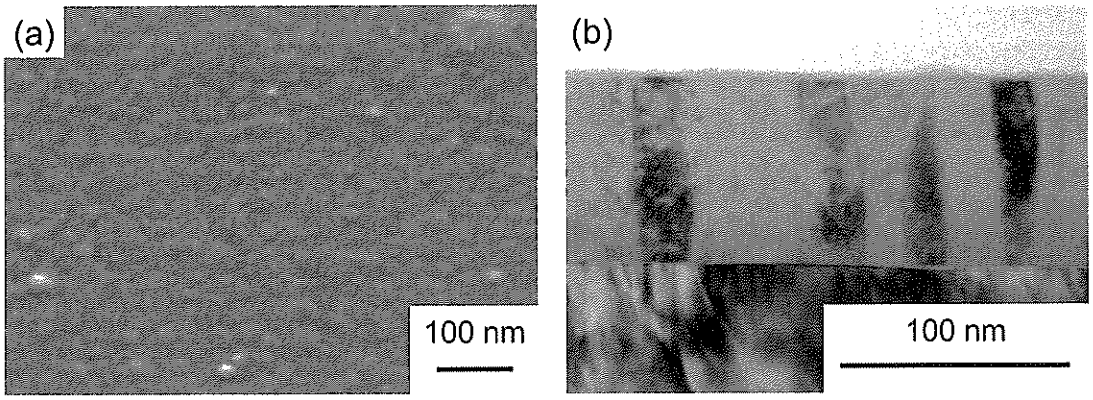

Figure S4.6. (a) SEM image of the surface of the LSM thin-film electrode deposited on YSZ electrolyte. (b) TEM image of the cross section of the dense LSM thin film / YSZ electrolyte.

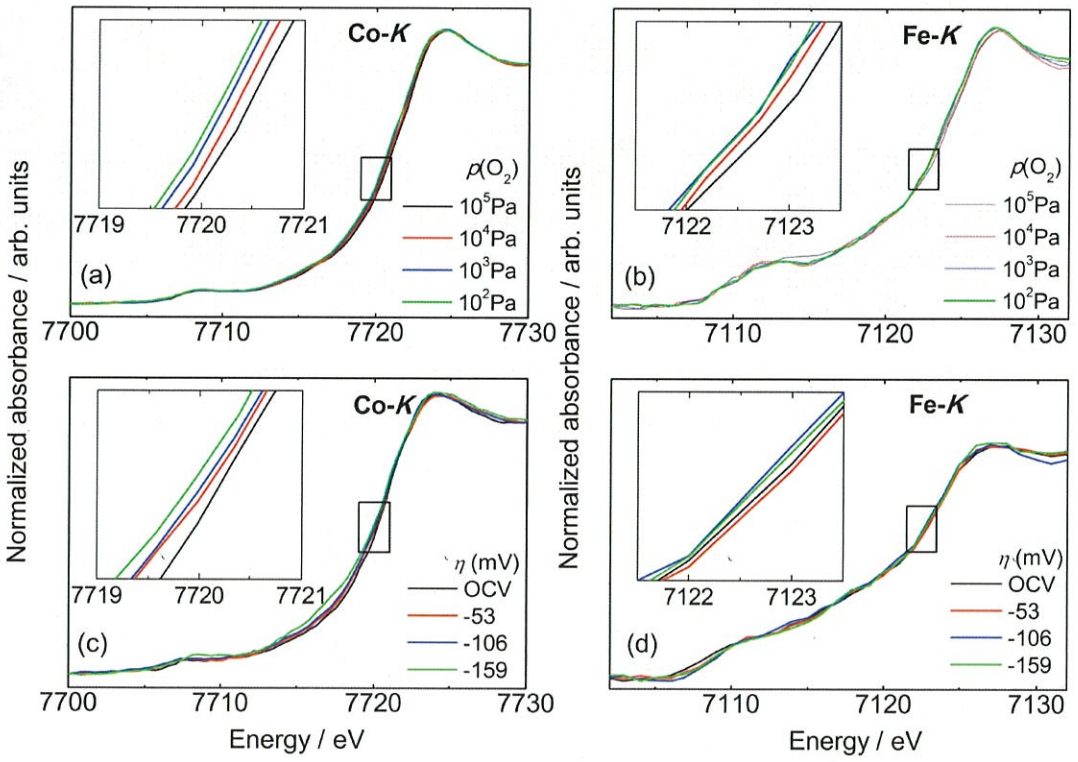

Figure S4.7. XANES spectra at the (a) Co and (b) Fe *K*-edges of the LSCF/YDC model electrode measured under various oxygen partial pressures in the open circuit condition at 1073 K. XANES spectra measured after applying various biases at an oxygen partial pressure of 10^5 Pa at 1073 K at the (c) Co or (d) Fe *K*-edge.

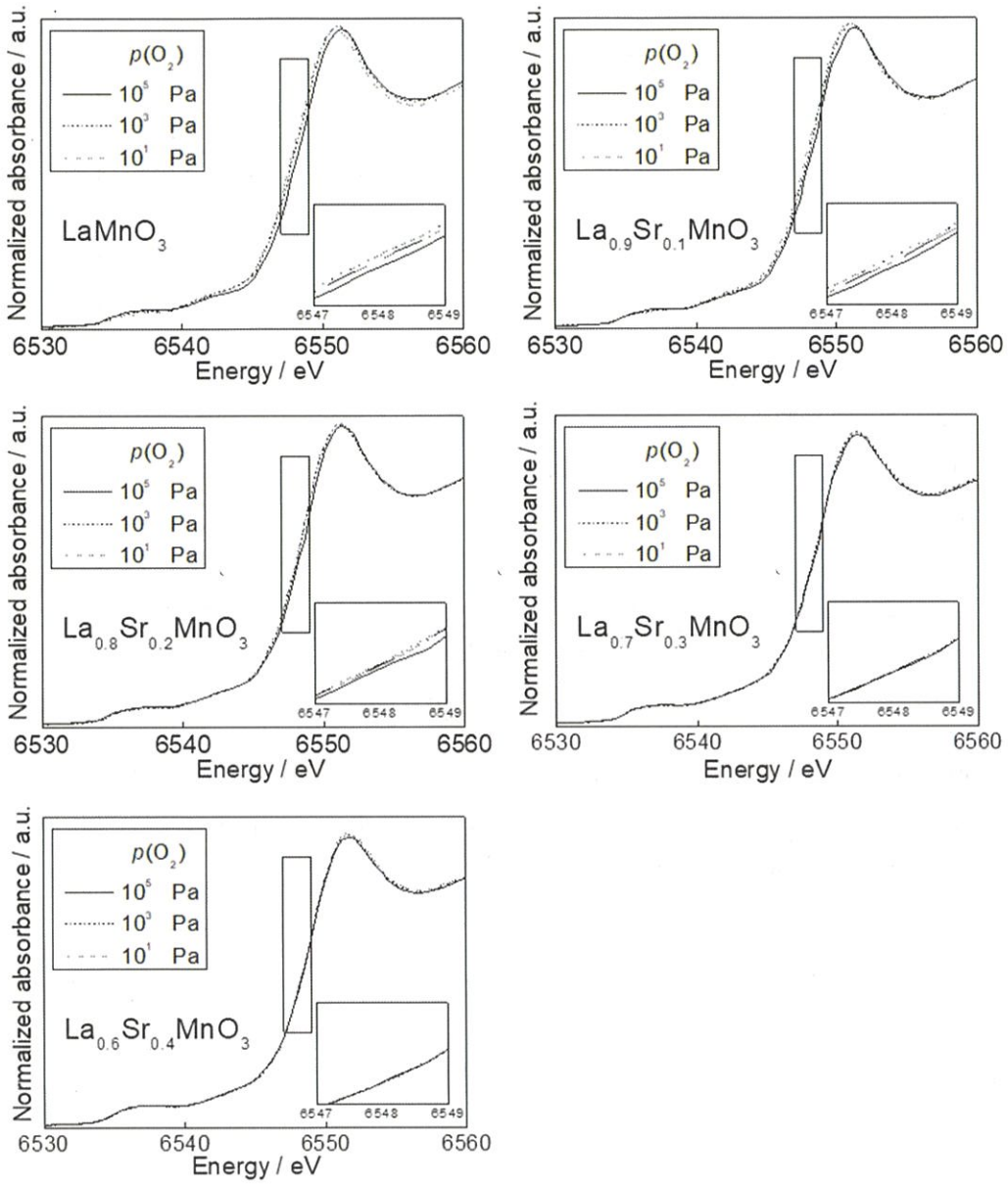

Figure S4.8. Mn *K*-edge XANES spectra of $La_{1-x}Sr_xMnO_{3\pm\delta}$ (x = 0.0, 0.1, 0.2, 0.3, 0.4) annealed under various oxygen partial pressures at 1073 K. The inset shows an expanded view around the absorption edge.

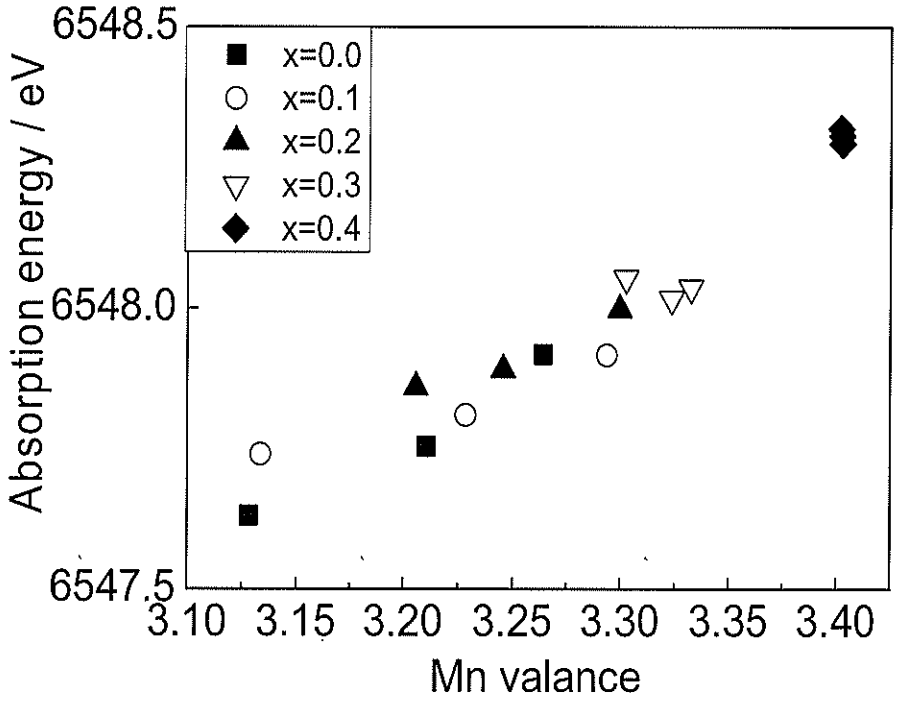

Figure S4.9. Mn *K*-edge absorption edge energy of $La_{1-x}Sr_xMnO_{3\pm\delta}$ (x = 0.0, 0.1, 0.2, 0.3, 0.4) annealed under various oxygen partial pressures at 1073 K as a function of the Mn mean valance estimated by iodometric titrations.

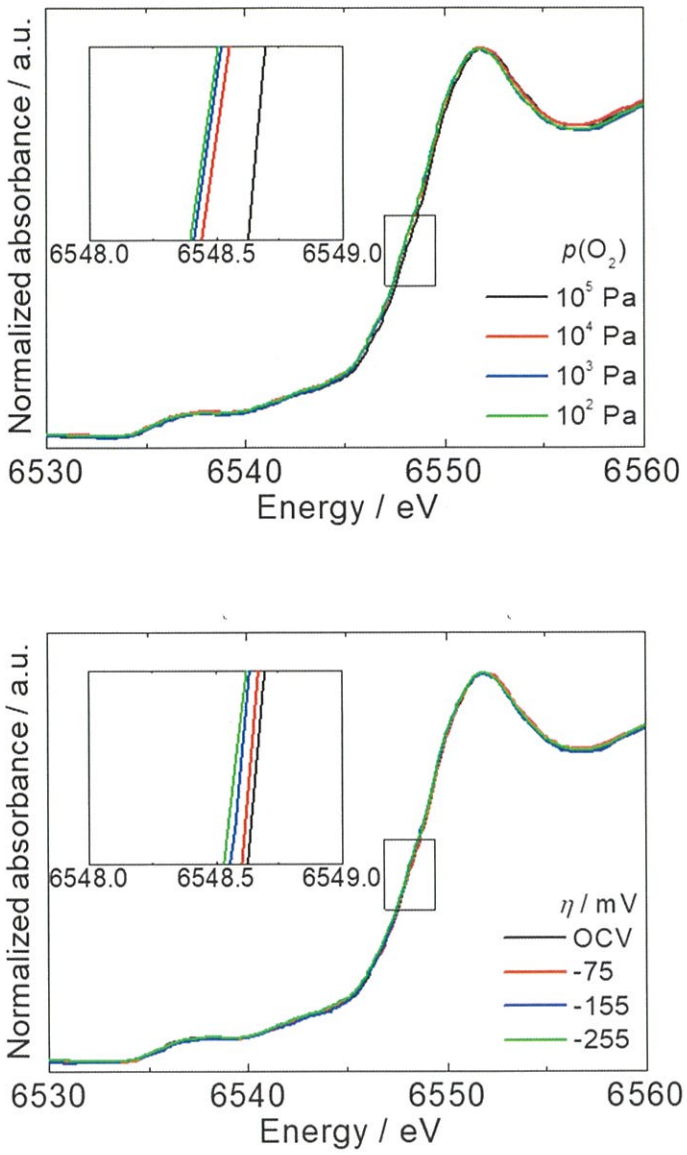

Figure S4.10. (a) XANES spectra at the Mn *K*-edge of the LSM/YSZ model electrode measured under various oxygen partial pressures in the open circuit condition at 1073 K. (b) XANES spectra at the Mn *K*-edge measured after applying various biases at an oxygen partial pressure of 10^5 Pa at 1073 K.

Appendix: Calculation of Oxygen Chemical Potential Through Thin Films

Under the oxygen chemical gradient along an x axis, the fluxes of charge carriers in the oxide are described as follows:

$$j_{O^{2-}} = -\frac{\sigma_{O^{2-}}}{4F^2}\frac{d\eta_{O^{2-}}}{dx} \quad \text{(S4.1)}$$

$$j_{e^-} = -\frac{\sigma_{e^-}}{F^2}\frac{d\eta_{e^-}}{dx} \quad \text{(S4.2)}$$

$$j_{h^+} = -\frac{\sigma_{h^+}}{F^2}\frac{d\eta_{h^+}}{dx} \quad \text{(S4.3)}$$

where j is the flux, σ the electrical conductivity, and η the electrochemical potential of each carrier (O^{2-} : oxide ion, e^-: electron, and h^+: hole), respectively, and F is the Faraday constant. Under the open-circuit conditions, these fluxes on p-type electronic and ionic conductivity are related as the following equation,

$$2\,j_{O^{2-}} - j_{h^+} = 0 \quad \text{(S4.4)}$$

The equilibrium condition at gas/electrode interface is expressed as the following equations:

$$\frac{1}{2}O_2 = O^{2-} + 2\,h^+ \quad \text{(S4.5)}$$

$$\frac{1}{2}\mu_O = \eta_{O^{2-}} + 2\eta_{h^+} \quad \text{(S4.6)}$$

where μ_O is the oxygen chemical potential. From Eq. (S4.1), (S4.3), (S4.4), and (S4.6), $j_{O^{2-}}$ and j_{h^+} are expressed as follows.

$$j_{O^{2-}} = -\frac{\sigma_{O^{2-}}}{8F^2}\frac{d\mu_O}{dx} + \frac{\sigma_{O^{2-}}}{2F^2}\frac{d\eta_{h^+}}{dx} \quad \text{(S4.7)}$$

$$j_{h^+} = 2\,j_{O^{2-}} = -\frac{\sigma_{h^+}}{F^2}\frac{d\eta_{h^+}}{dx} \quad \text{(S4.8)}$$

From Eq. (S7) and (S8), the following equation is derived:

$$j_{O^{2-}} = -\frac{RT}{8F^2}\frac{\sigma_{O^{2-}} \times \sigma_{h^+}}{\sigma_{O^{2-}} + \sigma_{h^+}}\frac{d\mu_O}{dx} \quad \text{(S4.9)}$$

Chapter 5. Surface Analysis of Lanthanum Strontium Cobalt Oxides under Cathodic Polarization at High Temperature through *Operando* Total-reflection X-ray Absorption and X-ray Fluorescence Spectroscopy

5.1. Introduction

Reducing the operating temperature of solid oxide fuel cells (SOFCs) is advantageous because it reduces the cell operating cost and improves durability, which can broaden the practical applications of SOFCs [1]. However, kinetics of the cathode reaction considering the conversion of the oxygen gas to the oxide ion, and the subsequent ion transport into the electrolyte, is diminished at low temperature [2]. In order to enhance cathode kinetics, the cathode reaction mechanism at high temperature must be elucidated. Oxygen reduction on the electrode surface is one of the primary reactions that occur in the SOFC cathodes [3]. For cathode reactions using typical perovskite or Ruddlesden-Popper oxide cathodes, except for lanthanum manganese oxides, oxygen reduction including adsorption and ionization is the rate-limiting step [4-8]. The importance of cathode surface reactions in SOFCs motivated us to investigate the surface chemistry of cathode materials. Because such surface phenomena are considered to be specific under high temperature conditions, *in situ* or *operando* observation of the nanosurface can lead to a novel approach for understanding cathode reactions [9].

$La_{1-x}Sr_xCoO_{3-\delta}$ and their related perovskite oxides are representative cathode materials and have been considered as potential cathode materials for SOFCs because of their high ionic and electric conductivity properties [10, 11]. Previous studies related to the surface analysis of perovskite oxides have identified the formation of a Sr-enriched phase (i.e., Sr segregation) at high temperature [12-23], which induces compositional changes in cathode materials and impedes the kinetics of cathode reactions. During SOFC operation, the cathodic polarization of the electrodes also influences the surface chemistry. Sr segregation reduction is an efficient path to enhance the surface cathode reactions. Since the enhanced oxygen exchange reaction at the heterostructured oxide interface between $La_{1-x}Sr_xCoO_{3-\delta}$ and $La_{2-x}Sr_xCoO_{4\pm\delta}$ was found [24], the improved kinetics of the cathode reaction using $La_{1-x}Sr_xCoO_{3-\delta}$–$La_{2-x}Sr_xCoO_{4\pm\delta}$ mixed composite perovskite [25, 26], $La_{1-x}Sr_xCoO_{3-\delta}$ thin films decorated with strontium oxide, and $La_{2-x}Sr_xCoO_{4\pm\delta}$ have been reported [12-15, 27]. Studies based on the thin-film interface model between $La_{1-x}Sr_xCoO_{3-\delta}$ and $La_{2-x}Sr_xCoO_{4\pm\delta}$ have reported the presence of a stable phase of $La_{2-x}Sr_xCoO_{4\pm\delta}$ on the surface at high temperature and the observation of a large number of active sites for oxygen dissociation–incorporation under cathodic polarization [19]. These surface mechanisms are commonly explained by X-ray photoemission spectroscopy, because it is a surface-sensitive analytical technique. Considering the oxygen potential profile under cathodic polarization at high temperature [4], the oxygen nonstoichiometry and oxidation state of cations in the electrode bulk change significantly [28], which is considered to influence the electrode surface.

Moreover, the chemical analysis of cations combined with surface analysis can elucidate the mechanism of the oxygen reduction reaction (ORR) at high temperature.

To determine the oxidation state of transition metals, X-ray absorption spectroscopy (XAS) is an effective technique that provides information on the electronic and local structures of absorbance atoms [9]. It is possible to analyze the chemical state of target atoms, because XAS data are related to specific atoms. In addition, spectra in the hard X-ray region can be obtained even in the presence of oxygen gas. Therefore, XAS has been used for *in situ* analysis of SOFC cathodes under high temperature and pressure conditions [6, 7, 29-35]. Although standard XAS reflects bulk information, the use of geometry setups including grazing incident X-ray diffraction [36] or low-angle X-ray fluorescence [37, 38] can provide surface-sensitive spectra. We have previously detected oxidation changes related to the surface segregation phenomena of $La_{0.8}Sr_{0.2}CoO_3$ thin films at high temperature by depth-resolved XAS [39].

In this study, the surface oxidation state of transition metals in lanthanum strontium cobalt oxides (LSC) was determined during cathodic polarization and compared with that of the bulk state. $La_{0.6}Sr_{0.4}CoO_{3-\delta}$ thin-film electrodes on yttrium-stabilized zirconium (YSZ)-poly crystalline substrates with a gadolinium-doped ceria interlayer were prepared by pulse laser deposition (PLD), followed by decoration with $(La_{0.5}Sr_{0.5})_2CoO_{4\pm\delta}$ of various thicknesses. Oxygen reduction kinetics for the electrodes were examined by electrochemical polarization and impedance measurements. The surface oxidation state was analyzed using *operando* total-reflection fluorescence X-ray absorption spectroscopy (TRF-XAS), which integrates the fluorescence yield obtained under total reflection and allows the investigation of surface reactions at the nanoscale under cathodic polarization. Furthermore, by conducting *operando* (TRF-XAS)-based XRF analysis, elemental analysis of LSC was performed under the operating conditions. Through the combination of these techniques, the electronic structure and elemental content change that occurred on the electrode surface of the LSC thin-film electrode were determined.

5.2. Experimental

5.2.1. Sample preparation

LSC [$La_{0.6}Sr_{0.4}CoO_{3-\delta}$ and $(La_{0.5}Sr_{0.5})_2CoO_{4\pm\delta}$] thin films (the oxides are defined as LSC_{113} and LSC_{214}, respectively) were prepared by PLD with a YAG laser (λ = 256 nm). The target samples were synthesized through a conventional solid-state reaction and a complex polymerization process. To prepare LSC_{113}, stoichiometric amounts of La_2O_3, CoO, and $Sr(NO_3)_2$ (Wako Pure Chemical) were mixed in a mortar. Subsequently, calcination was performed at 1423 K for 5 h. The resulting LSC_{113} powder was pressed into pellets and sintered at 1523 K for 10 h under air. To prepare LSC_{214}, La_2O_3 (Kojundo Chemical) was pre-dried at 1273 K under air and dissolved in nitric acid. Then, stoichiometric amounts of $Co(NO_3)_2 \cdot 6H_2O$ and $Sr(NO_3)_2$ (Wako Pure Chemical) were added until

dissolved. Citric acid and ethylene glycol were added in excess to the solution. The solution was gradually fired at 423 K to obtain a gel. Organic residuals were removed by heating at 673 K, and this precursor was calcined at 1273 K for 10 h. Gadolinium-doped ceria (GDC, Rhodia, Japan) was used as the buffer layer. GDC powder was pressed into pellets and sintered at 1473 K for 10 h under air. Separately, YSZ powder was pressed into pellets and sintered at 1773 K for 10 h under air. The sintered YSZ pellets were mirror-polished and used as the substrate; the base pressure in the chamber was $<10^{-5}$ Pa. Deposition under 10 Hz repetition was performed for 5 min using a GDC target and for 15 min for the LSC_{113} thin film at a substrate temperature of 1173 K. Decorated deposition of LSC_{214} was performed on LSC_{113} through numerous pulses (25–2700 pulses) at a substrate temperature of 1173 K. All film samples were characterized by X-ray diffraction (XRD, Rigaku RINT2200) with Cu-K_α (40 kV, 40 mA). To perform *operando* TRF-XAS and XRF, an (110)-oriented YSZ single crystal was used as a substrate for PLD because a thin film sample with a flat and smooth surface was required. The PLD preparation conditions were similar for each thin film when using a polycrystalline YSZ substrate, and the LSC_{214} thin film obtained with 900 pulses was selected because it showed the highest ORR activity. The thin films prepared on (110)-oriented YSZ single-crystal substrates were characterized by XRD, atomic force microscopy (AFM), and transmission electron microscopy (TEM).

5.2.2. Electrochemical testing

A three-electrode cell was constructed to determine the electrochemical performance (Fig. S5.1) at 1073 K and under the open circuit condition (OCV) at oxygen partial pressure [$p(O_2)$] of 10^5 Pa. The working electrode (WE) consisted of LSC_{113} decorated with LSC_{214}. The counter electrode (CE) and reference electrode were porous platinum. Electrochemical impedance spectroscopy (EIS) data and direct current (DC) polarization of the film electrodes were respectively conducted using an impedance analyzer and a potentiostat (Solartron 1255 and 1287, respectively). Impedance measurements were conducted over the frequency range from 1 MHz to 0.1 Hz with an amplitude alternating current voltage of 10 mV.

5.2.3. *Operando* XAS and XRF analysis

A three-electrode cell using thin films was prepared to perform *operando* TRF-XAS and XRF at the BL01B1 beamline (SPring-8, JASRI, Japan). Co *K*-edge X-ray absorption near-edge spectroscopy (XANES) was conducted under the fluorescence mode using a 19-element Ge solid-state detector (SSD). A schematic of the TRF-XAS setup of the cell is shown in Fig. 5.1a. XAS and XRF measurements were performed at 773 K and $p(O_2)$ of 10^5 Pa under OCV. In addition, the measurements under constant polarizations of −100 and −900 mV (WE–CE) were conducted. Figs. 5.1b and c show the fluorescence detector counts as a function of the incident angle for LSC_{113} and LSC_{113} with 3 nm of LSC_{214} decoration (denoted as $LSC_{113/214}$). The calculated critical angle of total reflection (θ_c) for

LSC_{113} was 0.375°. The highest count was observed at 0.40° and 0.38° for LSC_{113} and $LSC_{113/214}$, respectively, which was consistent with the calculated angle. Because the incident angle for the surface region of the sample was required to be smaller than θ_c, we set half of the SSD counts of the highest counts as the surface measurement angle. When the incident angle was set at 0.30°, the penetration depth was estimated to be ~5 nm (denoted as "surface" in Figs. 5.1b and c). The bulk information was obtained by setting the incident angle at 2.3°; under that condition, the penetration depth was estimated to be >100 nm. Considering that the thickness of LSC_{113} was ~60 nm, information regarding this film could be obtained. XRF spectra were also collected at an incident energy of 16.5 eV.

5.3. Results and discussion

The crystal structures of each prepared thin film on a SiO_2 glass substrate were characterized. XRD patterns of GDC (the buffer layer) and LSC_{113} and LSC_{214} thin films on SiO_2 are shown in Fig. S5.2. All peaks were identified on the basis of the reported crystal structures for GDC, LSC_{113}, and LSC_{214}. The lattice constants of the thin films were consistent with the database (Table S5.1). We confirmed the formation of an LSC_{113} phase for the LSC_{113} thin film at the (110) YSZ plane, as shown in Fig. S5.3. AFM analysis demonstrated that LSC_{113} and $LSC_{113/214}$ films at the (110) YSZ plane had a small surface roughness with root-mean-square values of ~1.32 and ~3.01 nm, respectively (Fig. S5.4). The cross-sectional TEM images of the thin films are shown in Fig. S5.5; dense film layers with thicknesses of 60, 3, and 25 nm were obtained for LSC_{113}, LSC_{214}, and GDC, respectively. These results confirmed that the prepared thin films could be used as model electrodes to investigate their surface phenomena via *operando* TRF-XAS.

Previous studies have reported enhanced ORR kinetics through the decoration of LSC_{113} with LSC_{214} [13, 16]. Similarly, in our thin film study, this kinetics enhancement using LSC_{214} decoration was also observed through EIS and DC polarization measurements. Fig. 5.2 shows Nyquist plots and the calculated area specific conductivity obtained from EIS measured at 1073 K and $p(O_2)$ of 10^5 Pa. It can be observed that LSC_{214} decoration decreased the resistance related to the semicircle up to 3 nm (900 pulses of LSC_{214} deposition) and increased at 10 nm (2700 pulses). This represents an enhancement approximately three orders of magnitude higher for the decoration of 3 nm LSC_{214} compared to that for bare LSC_{113}. However, electrode kinetics slightly decreased to 10 nm for LSC_{214}. The enhanced kinetics could also be confirmed through the DC polarization measurements for the bare LSC_{113} and the LSC_{113} with a 3 nm LSC_{214} deposition, at 1073 K and $p(O_2)$ of 10^5 Pa (Fig. 5.3). As shown in Fig. 5.3, the current density for $LSC_{113/214}$ significantly increased. These trends were consistent with those reported in previous studies [13, 16]. We will discuss the surface chemistry from the results obtained by TRF-XAS and XRF using the bare LSC_{113} and the 3 nm LSC_{214} decoration on LSC_{113} sample ($LSC_{113/214}$).

Operando Co K-edge XANES of LSC thin films enables us to determine the oxidation state

obtained from electrochemical cathodic polarization. In addition, the TRF setup provides surface-sensitive information, which is compared with the bulk information. Fig. 5.4 shows the normalized Co K-edge XANES spectra for LSC_{113} and $LSC_{113/214}$ under different applied potentials at 773 K and $p(O_2)$ of 10^5 Pa. Bulk information for LSC_{113} and $LSC_{113/214}$ from the standard fluorescence XAS spectra is depicted in Figs. 5.4a and b, respectively. When cathodic polarization increased, the absorption edge observed at 7720 eV shifted toward the lower energy side. The absorption energy of Co K-edge XANES in LSC corresponded to the oxidation state of cobalt in the electrodes, which was determined by oxygen nonstoichiometry [40]. The low energy shift observed in LSC_{113} and $LSC_{113/214}$ indicated that cathodic polarization induced oxygen vacancy in LSC and decreased the oxygen chemical potential, which will be further discussed quantitatively in the following section. The surface-sensitive XANES spectra for LSC_{113} and $LSC_{113/214}$ from the TRF measurements are illustrated in Figs. 5.4 c and d, respectively. It should be noticed that even at low cathodic polarization, a drastic profile change was induced in the Co K-edge XANES spectra for LSC_{113}, while a continuous energy shift was observed in the bulk XANES data. Compared with the Co K-edge XANES spectra under OCV, the XANES spectra measured at 100 mV broadened and located at lower energy. This structural change is related to the Sr enrichment in the LSC phase because of the similarity with the corresponding XANES spectra for $Sr_6Co_5O_{15}$, which is a Sr-rich and non-stoichiometric compound [39]. In addition, the XANES spectra for $LSC_{113/214}$ showed a gradual increase in edge inclination, implying that Sr-rich phase formation was suppressed at low cathodic polarization. The surface XANES spectra significantly changed upon potential application. As the bulk XANES spectra showed negligible differences between LSC_{113} and $LSC_{113/214}$ upon potential application, the structural difference is the nanoscale ordered phenomena at the surface, which cannot be explained by conventional techniques in order to analyze bulk materials. The estimated edge energy shift as a function of the applied voltage is provided in Fig. S6 in the supporting information.

The edge energy shift, which is an indicator of the oxidation state, was further analyzed as a function of the effective oxygen partial pressure, $p(O_2)_{eff}$. The electrode polarization potentials, η, were calculated using the following expression:

$$\eta = V_{apply} - R_{bulk} I \tag{5.1}$$

where V_{apply}, R_{bulk}, and I are the voltage applied to the cell, electrolyte resistance, and current, respectively. Under polarization conditions, $p(O_2)_{eff}$ is defined in terms of η as follows:

$$p(O_2)_{eff} = \exp\left\{\frac{2\mu_{O,eff}}{RT}\right\} = p(O_2)\exp\left\{\frac{4F\eta}{RT}\right\} \tag{5.2}$$

where R is the gas constant and F is the Faraday constant. Under OCV, (η = 0), $p(O_2)_{eff}$ is equivalent to $p(O_2)$. In this study, the application of −400 mV between the two electrodes (WE–CE) corresponded to $p(O_2)_{eff}$ that was approximately four orders of magnitude high. The energy shift

calculated from Co K-edge XANES spectra as a function of $p(O_2)_{eff}$ is shown in Fig. 5a. For bulk XANES, there was no difference between the spectral results for LSC_{113} and $LSC_{113/214}$. This demonstrated that the oxygen potential change induced by cathodic polarization is similar for LSC_{113} and $LSC_{113/214}$; thus, these LSC had the same rate-determining step in the reaction mechanism (probably surface reaction limitation as in previously reported studies [4]). The surface oxidation state exhibited an evident difference between LSC_{113} and $LSC_{113/214}$. While the energy shift on the LSC_{113} surface was induced under small polarization, a gradual energy shift was observed for $LSC_{113/214}$. The energy shift for $LSC_{113/214}$ even at $p(O_2)_{eff}$ of 10 Pa was lower than that for LSC_{113} at $p(O_2)_{eff}$ of 10^4 Pa. As mentioned previously, the energy shift was related to Sr enrichment in the LSC phase. The difference in the edge energy shifts confirmed the suppression of that Sr enrichment by LSC_{214} decoration. Previous reports using XPS have not clearly distinguished the surface secondary phase and LSC phases [14, 16]. Because the Co K-edge TRF-XAS results directly corresponded to the oxidation state of cobalt oxides, the *operando* XAS results confirmed the Sr enrichment in LSC phases and the suppression effect of LSC_{214} decoration.

To investigate the phenomena related to Sr enrichment in LSC phases, the elemental analysis of for LSC_{113} and $LSC_{113/214}$ was conducted through *operando* TRF-XRF. The XRF spectra are provided in Fig. S7 in the supporting information. The scattered X-ray was observed at 16.5 keV. The peaks observed at approximately 4.5, 6.9, and 14.1 keV can be assigned to La-L, Co-K, and Sr-K, respectively. In addition to these peaks from LSC phases, other fluorescence peaks were detected at 7.9 and 9.1 keV. These peaks can be assigned to Hf-L from the YSZ substrates because the YSZ single crystals contain a few weight percent of Hf impurity [41]. Even for the surface-sensitive TRF configuration, the peaks from Hf-L also appeared. This is because the scattered X-ray spreads in all directions, which induces the fluorescence from the substrates. To compare the changes of the relative intensity of Sr fluorescence for LSC_{113} and $LSC_{113/214}$ on the surface and bulk as a function of $p(O_2)_{eff}$, the peak areas of Sr normalized by Co were plotted in Fig. 5b. We note that the higher Sr ratio of LSC_{113} bulk than $LSC_{113/214}$ bulk is within the experimental error. However, compared to the experimental error, we observed a more than twofold change in the area ratio with the bias applied for the surface spectra. While the peak areas of Sr at the surface for LSC_{113} and $LSC_{113/214}$ increased under cathodic polarization, the peaks of the bulk did not change under polarization. For LSC_{113}, the amount of Sr on the surface remarkably increased, which demonstrated Sr enrichment in the LSC phase because XRF detects La and Co simultaneously. Although an increase in Sr fluorescence intensity at the surface was also observed for $LSC_{113/214}$, the amount of enriched Sr significantly decreased, which is also in agreement with the energy shift of *operando* Co K-edge XANES spectra.

The experimental results provided insights into the surface mechanism under cathodic polarization at high temperature, as shown in Fig. 5.6. Although the *operando* XAS and XRF measurements were performed at 773 K due to the limitation of thermal insulation properties of the cell, the observed

phenomena are expected to be also happen at higher temperature condition. The cathodic polarization of LSC_{113} induced the predominant Sr enrichment on the surface, which decreased ORR activity due to deviation from the ideal electronic state, such as the O p-band center [42]. The driving force of Sr enrichment is the high temperature and/or electrochemically derived reducing conditions at the electrode surface. These essential factors cannot be avoided, and the subsequent Sr migration can be disturbed by surface modification of the secondary phase such LSC_{214}. Compared to LSC_{113}, the amount of oxygen nonstoichiometry for LSC_{214} was considerably low [43, 44], which hindered the atomic configuration change in the crystal. When the LSC_{214} phase was decorated on the LSC_{113} surface, this inertial property of LSC_{214} prevented Sr from moving toward the surface of LSC_{113}, which preserved the ideal band structure of LSC_{113}.

5.4. Conclusion

Dense LSC_{113} and $LSC_{113/214}$ thin film electrodes on the YSZ substrate with a GDC interlayer were prepared. From the results, it can be concluded that LSC_{214} decoration on LSC_{113} enhanced ORR activity by more than two orders of magnitude at high temperature. *Operando* TRF-XAS and XRF under cathodic polarization were performed. The predominant surface reduction of Co ions with Sr enrichment under cathodic polarization was observed for LSC_{113}. This was suppressed by LSC_{214} decoration, which improved ORR activity of the as-prepared electrode.

Acknowledgement

This work was supported by JSPS KAKENHI Grant Number JP25810134 and JP18H03929. The synchrotron radiation experiments were performed at SPring-8 with the approval of the Japan Synchrotron Radiation Research Institute (JASRI).

REFERENCES

[1] E.D. Wachsman, K.T. Lee, Lowering the Temperature of Solid Oxide Fuel Cells, *Science* **334** (2011) 935-939.

[2] D.J.L. Brett, A. Atkinson, N.P. Brandon, S.J. Skinner, Intermediate temperature solid oxide fuel cells, *Chem. Soc. Rev.* **37** (2008) 1568-1578.

[3] J. Mizusaki, K. Amano, S. Yamauchi, K. Fueki, Electrode reaction at Pt, O_2(g)/stabilized zirconia interfaces. Part I: Theoretical consideration of reaction model, *Solid State Ionics* **22** (1987) 313-322.

[4] T. Kawada, J. Suzuki, M. Sase, A. Kaimai, K. Yashiro, Y. Nigara, J. Mizusaki, K. Kawamura, H. Yugami, Determination of Oxygen Vacancy Concentration in a Thin Film of $La_{0.6}Sr_{0.4}CoO_{3-\delta}$ by an

Electrochemical Method, *J. Electrochem. Soc.* **149** (2002) E252-E259.

[5] S.B. Adler, Factors governing oxygen reduction in solid oxide fuel cell cathodes, *Chem. Rev.* **104** (2004) 4791-4843.

[6] Y. Orikasa, T. Ina, K. Yamamoto, T. Nakao, A. Mineshige, K. Amezawa, T. Kawada, H. Tanida, T. Uruga, Y. Uchimoto, Direct Observation of Rate Determining Step for Nd_2NiO_{4+d} SOFC Cathode Reaction by operando Electrochemical XAS, *Electrochemistry* **82** (2014) 897-900.

[7] T. Nakamura, R. Oike, Y. Kimura, Y. Tamenori, T. Kawada, K. Amezawa, Operando Soft X-ray Absorption Spectroscopic Study on a Solid Oxide Fuel Cell Cathode during Electrochemical Oxygen Reduction, *Chemsuschem* **10** (2017) 2008-2014.

[8] Y. Tsuji, K. Amezawa, T. Nakao, T. Ina, T. Kawada, K. Yamamoto, Y. Uchimoto, Y. Orikasa, Investigation of Cathodic Reaction Mechanism in Solid Oxide Fuel Cells by Operando X-Ray Absorption Spectroscopy, *Electrochemistry submitted.*

[9] Amezawa, X-ray absorption spectroscopic studies on solid oxide fuel cells and proton-conducting ceramic fuel cells, *Current Opinion in Electrochemistry* **21** (2020) 250-256.

[10] Y. Ohno, S. Nagata, H. Sato, Effect of electrode materials on the properties of high-temperature solid electrolyte fuel cells, *Solid State Ionics* **3-4** (1981) 439-442.

[11] N. Teiji, M. Makoto, Y. Yukio, Reduction-oxidation and Catalytic Properties of Perovskite-type Mixed Oxide Catalysis ($La_{1-x}Sr_xCoO_3$), *Chem. Lett.* **10** (1981) 1589-1592.

[12] E.J. Crumlin, E. Mutoro, S.J. Ahn, G.J. la O, D.N. Leonard, A. Borisevich, M.D. Biegalski, H.M. Christen, Y. Shao-Horn, Oxygen Reduction Kinetics Enhancement on a Heterostructured Oxide Surface for Solid Oxide Fuel Cells, *J. Phys. Chem. Lett.* **1** (2010) 3149-3155.

[13] E. Mutoro, E.J. Crumlin, M.D. Biegalski, H.M. Christen, Y. Shao-Horn, Enhanced oxygen reduction activity on surface-decorated perovskite thin films for solid oxide fuel cells, *Energy Environ. Sci.* **4** (2011) 3689-3696.

[14] E.J. Crumlin, E. Mutoro, Z. Liu, M.E. Grass, M.D. Biegalski, Y.-L. Lee, D. Morgan, H.M. Christen, H. Bluhm, Y. Shao-Horn, Surface strontium enrichment on highly active perovskites for oxygen electrocatalysis in solid oxide fuel cells, *Energy Environ. Sci.* **5** (2012) 6081-6088.

[15] E. Mutoro, E.J. Crumlin, H. Pöpke, B. Luerssen, M. Amati, M.K. Abyaneh, M.D. Biegalski, H.M. Christen, L. Gregoratti, J. Janek, Y. Shao-Horn, Reversible Compositional Control of Oxide Surfaces by Electrochemical Potentials, *J. Phys. Chem. Lett.* **3** (2012) 40-44.

[16] E.J. Crumlin, E. Mutoro, W.T. Hong, M.D. Biegalski, H.M. Christen, Z. Liu, H. Bluhm, S.H. Yang, In Situ Ambient Pressure X-ray Photoelectron Spectroscopy of Cobalt Perovskite Surfaces under Cathodic Polarization at High Temperatures, *J. Phys. Chem. C* **117** (2013) 16087-16094.

[17] Z. Feng, E.J. Crumlin, W.T. Hong, D. Lee, E. Mutoro, M.D. Biegalski, H. Zhou, H. Bluhm, H.M. Christen, Y. Shao-Horn, In Situ Studies of the Temperature-Dependent Surface Structure and Chemistry of Single-Crystalline (001)-Oriented $La_{0.8}Sr_{0.2}CoO_{3-\delta}$ Perovskite Thin Films, *J. Phys.*

Chem. Lett. **4** (2013) 1512-1518.

[18] Z. Feng, Y. Yacoby, M.J. Gadre, Y.-L. Lee, W.T. Hong, H. Zhou, M.D. Biegalski, H.M. Christen, S.B. Adler, D. Morgan, Y. Shao-Horn, Anomalous Interface and Surface Strontium Segregation in $(La_{1-y}Sr_y)_2CoO_{4\pm\delta}/La_{1-x}Sr_xCoO_{3-\delta}$ Heterostructured Thin Films, *J. Phys. Chem. Lett.* **5** (2014) 1027-1034.

[19] E.J. Crumlin, Z. Liu, H. Bluhm, W. Yang, J. Guo, Z. Hussain, X-ray spectroscopy of energy materials under in situ/operando conditions, *J. Electron. Spectrosc. Relat. Phenom.* **200** (2015) 264-273.

[20] W.T. Hong, K.A. Stoerzinger, E.J. Crumlin, E. Mutoro, H. Jeen, H.N. Lee, Y. Shao-Horn, Near-Ambient Pressure XPS of High-Temperature Surface Chemistry in $Sr_2Co_2O_5$ Thin Films, *Top. Catal.* **59** (2016) 574-582.

[21] Y. Yu, A.Y. Nikiforov, T.C. Kaspar, J.C. Woicik, K.F. Ludwig, S. Gopalan, U.B. Pal, S.N. Basu, Chemical characterization of surface precipitates in $La_{0.7}Sr_{0.3}Co_{0.2}Fe_{0.8}O_{3-\delta}$ as cathode material for solid oxide fuel cells, *J. Power Sources* **333** (2016) 247-253.

[22] M. Rohnke, K. Schaepe, A.K. Bachmann, M. Laenger, J. Janek, In situ ToF-SIMS monitoring of SOFC cathodes – A case study of $La_{0.74}Sr_{0.17}Mn_{1.01}O_{2.9}$ model electrodes, *Appl. Surf. Sci.* **422** (2017) 817-827.

[23] M. Niania, R. Podor, T.B. Britton, C. Li, S.J. Cooper, N. Svetkov, S. Skinner, J. Kilner, In situ study of strontium segregation in $La_{0.6}Sr_{0.4}Co_{0.2}Fe_{0.8}O_{3-\delta}$ in ambient atmospheres using high-temperature environmental scanning electron microscopy, *J. Mater. Chem. A* **6** (2018) 14120-14135.

[24] M. Sase, F. Hermes, K. Yashiro, K. Sato, J. Mizusaki, T. Kawada, N. Sakai, H. Yokokawa, Enhancement of oxygen surface exchange at the hetero-interface of $(La,Sr)CoO_3/(La,Sr)_2CoO_4$ with PLD-Layered films, *J. Electrochem. Soc.* **155** (2008) B793-B797.

[25] M. Sase, K. Yashiro, K. Sato, J. Mizusaki, T. Kawada, N. Sakai, K. Yamaji, T. Horita, H. Yokokawa, Enhancement of oxygen exchange at the hetero interface of $(La,Sr)CoO_3/(La,Sr)_2CoO_4$ in composite ceramics, *Solid State Ionics* **178** (2008) 1843-1852.

[26] K. Yashiro, T. Nakamura, M. Sase, F. Hermes, K. Sato, T. Kawada, J. Mizusaki, Composite Cathode of Perovskite-Related Oxides, $(La,Sr)CoO_{3-\delta}/(La,Sr)_2CoO_{4-\delta}$, for Solid Oxide Fuel Cells, *Electrochem Solid St* **12** (2009) B135-B137.

[27] J.W. Han, B. Yildiz, Mechanism for enhanced oxygen reduction kinetics at the $(La,Sr)CoO_{3-\delta}/(La,Sr)_2CoO_{4+\delta}$ hetero-interface, *Energy Environ. Sci.* **5** (2012) 8598-8607.

[28] J. Mizusaki, Y. Mima, S. Yamauchi, K. Fueki, H. Tagawa, Nonstoichiometry of the perovskite-type oxides $La_{1-x}Sr_xCoO_{3-\delta}$, *J. Solid State Chem.* **80** (1989) 102-111.

[29] K. Amezawa, Y. Orikasa, T. Ina, A. Unemoto, M. Sase, H. Watanabe, T. Fukutsuka, T. Kawada, Y. Terada, Y. Uchimoto, Electronic and Local Structures of $La_{1-x}Sr_xCoO_{3-\delta}$ Studied by In-Situ Micro XAS Measurements, *ECS Transactions* **13** (2008) 161-164.

[30] A. Hagen, M.L. Traulsen, W.R. Kiebach, B.S. Johansen, Spectroelectrochemical cell for in situ studies of solid oxide fuel cells, *J. Synchrotron Rad.* **19** (2012) 400-407.

[31] Y. Fujimaki, H. Watanabe, Y. Terada, T. Nakamura, K. Yashiro, S.i. Hashimoto, T. Kawada, K. Amezawa, Direct Evaluation of Oxygen Chemical Potential Distribution in an SOFC Cathode by In Situ X-Ray Absorption Spectroscopy, *ECS Transactions* **57** (2013) 1925-1932.

[32] R.J. Woolley, M.P. Ryan, S.J. Skinner, In Situ Measurements on Solid Oxide Fuel Cell Cathodes – Simultaneous X-Ray Absorption and AC Impedance Spectroscopy on Symmetrical Cells, *Fuel Cells* **13** (2013) 1080-1087.

[33] S.Y. Lai, D. Ding, M. Liu, M. Liu, F.M. Alamgir, Operando and In situ X-ray Spectroscopies of Degradation in $La_{0.6}Sr_{0.4}Co_{0.2}Fe_{0.8}O_{3-\delta}$ Thin Film Cathodes in Fuel Cells, *ChemSusChem* **7** (2014) 3078-3087.

[34] B.C. Eigenbrodt, A.M. Young, T.G. Howell, C.U. Segre, T.L. Reitz, High-Temperature, In Situ X-ray Absorption Study of Sr_2MgMoO_6 Solid-Oxide Fuel-Cell Anode Materials, *ChemElectroChem* **2** (2015) 1568-1575.

[35] R. Oike, Y. Okamoto, T. Tokushima, T. Nakamura, K. Amezawa, In-situ Simultaneous Soft X-ray Absorption and Emission Spectroscopy under Controlled Atmosphere and Temperature, *Electrochemistry* **84** (2016) 793-796.

[36] D. Takamatsu, Y. Koyama, Y. Orikasa, S. Mori, T. Nakatsutsumi, T. Hirano, H. Tanida, H. Arai, Y. Uchimoto, Z. Ogumi, First In Situ Observation of the $LiCoO_2$ Electrode/Electrolyte Interface by Total-Reflection X-ray Absorption Spectroscopy, *Angew. Chem. Int. Ed.* **51** (2012) 11597-11601.

[37] T. Okumura, T. Nakatsutsumi, T. Ina, Y. Orikasa, H. Arai, T. Fukutsuka, Y. Iriyama, T. Uruga, H. Tanida, Y. Uchimoto, Z. Ogumi, Depth-resolved X-ray absorption spectroscopic study on nanoscale observation of the electrode–solid electrolyte interface for all solid state lithium ion batteries, *J. Mater. Chem.* **21** (2011) 10051-10060.

[38] D. Takamatsu, T. Nakatsutsumi, S. Mori, Y. Orikasa, M. Mogi, H. Yamashige, K. Sato, T. Fujimoto, Y. Takanashi, H. Murayama, M. Oishi, H. Tanida, T. Uruga, H. Arai, Y. Uchimoto, Z. Ogumi, Nanoscale Observation of the Electronic and Local Structures of $LiCoO_2$ Thin Film Electrode by Depth-Resolved X-ray Absorption Spectroscopy, *J. Phys. Chem. Lett.* **2** (2011) 2511-2514.

[39] Y. Orikasa, E.J. Crumlin, S. Sako, K. Amezawa, T. Uruga, M.D. Biegalski, H.M. Christen, Y. Uchimoto, Y. Shao-Horn, Surface Strontium Segregation of Solid Oxide Fuel Cell Cathodes Proved by In Situ Depth-Resolved X-ray Absorption Spectroscopy, *ECS Electrochemistry Letters* **3** (2014) F23-F26.

[40] Y. Orikasa, T. Ina, T. Nakao, A. Mineshige, K. Amezawa, M. Oishi, H. Arai, Z. Ogumi, Y. Uchimoto, X-ray Absorption Spectroscopic Study on $La_{0.6}Sr_{0.4}CoO_{3-\delta}$ Cathode Materials Related with Oxygen Vacancy Formation, *J. Phys. Chem. C* **115** (2011) 16433-16438.

[41] T. Andersen, K.V. Hansen, M. Mogensen, I. Chorkendorff, Electrochemical removal of segregated silicon dioxide impurities from yttria stabilized zirconia surfaces at elevated temperatures, *Solid State Ionics* **190** (2011) 60-66.
[42] Y.-L. Lee, J. Kleis, J. Rossmeisl, Y. Shao-Horn, D. Morgan, Prediction of solid oxide fuel cell cathode activity with first-principles descriptors, *Energy Environ. Sci.* **4** (2011) 3966-3970.
[43] T. Nitadori, M. Muramatsu, M. Misono, Valence control, reactivity of oxygen, and catalytic activity of lanthanum strontium cobalt oxide ($La_{2-x}Sr_xCoO_4$), *Chem. Mater.* **1** (1989) 215-220.
[44] A. Unemoto, K. Nagao, T. Tairako, K. Amezawa, T. Kawada, Oxygen Reduction at the Surface and the Hetero-Interface of La-Sr-Co-O-Oxides, *ECS Transactions* **28** (2010) 59-70.

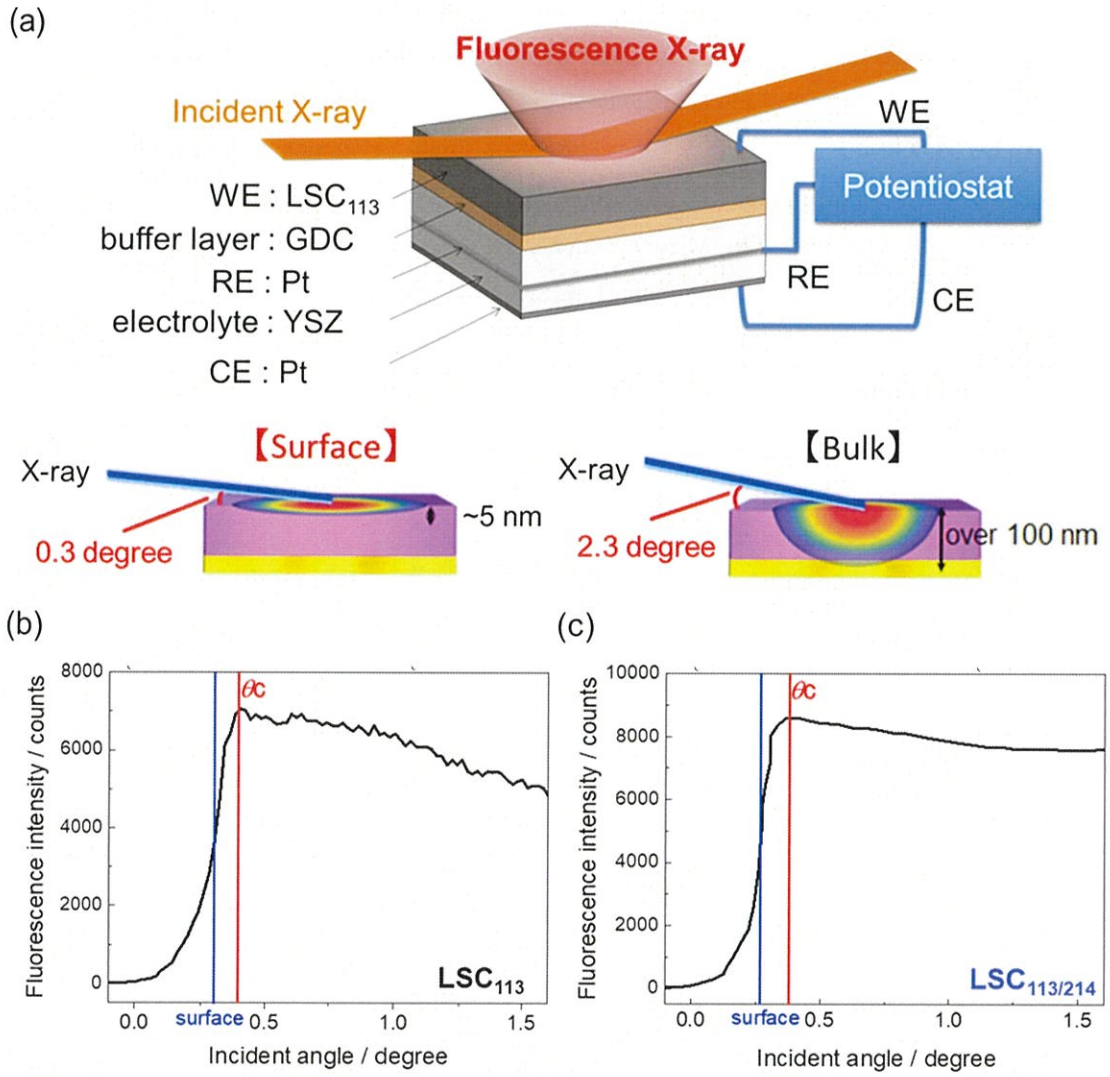

Figure 5.1. (a) Schematic of the setup for data collection in the *operando* total-reflection XAS cell. Fluorescence counts as a function of incident angle of (b) LSC_{113} and (c) $LSC_{113/214}$. The penetration depth was denoted as "surface" (blue font).

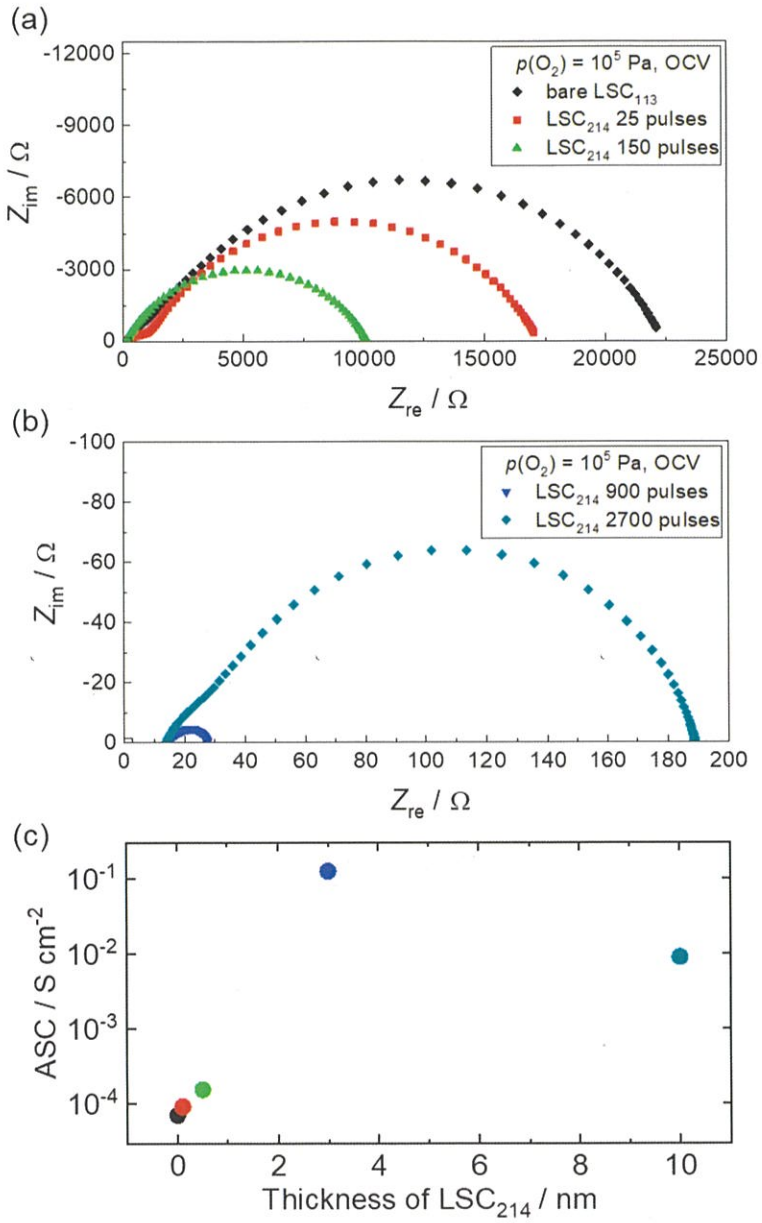

Figure 5.2. Nyquist plot from EIS at 1073 K and $p(O_2)$ of 10^5 Pa for (a) bare LSC_{113} and LSC_{214}-decorated LSC_{113} (25 and 150 pulses); (b) LSC_{214}-decorated LSC_{113} (900 and 2700 pulses). (c) Area specific interfacial conductivity as a function of LSC_{214} layer thickness.

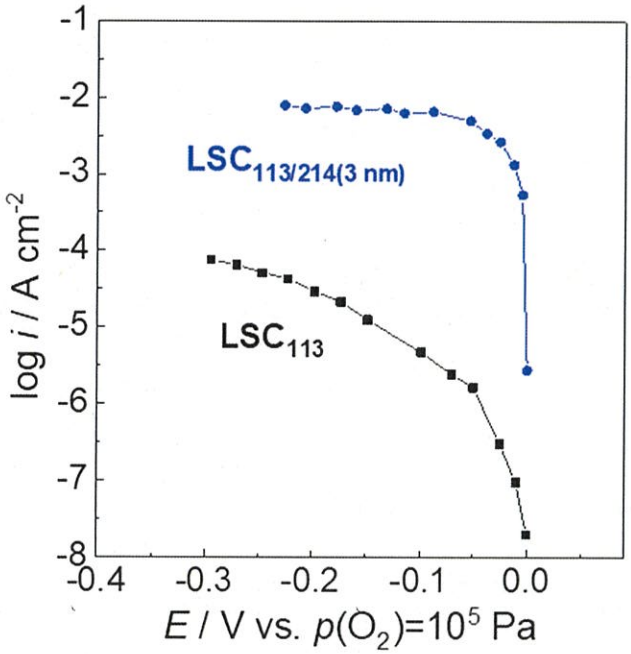

Figure 5.3. Current-potential curve for LSC_{113} and $LSC_{113/214}$ on YSZ at 1073 K and $p(O_2)$ of 10^5 Pa.

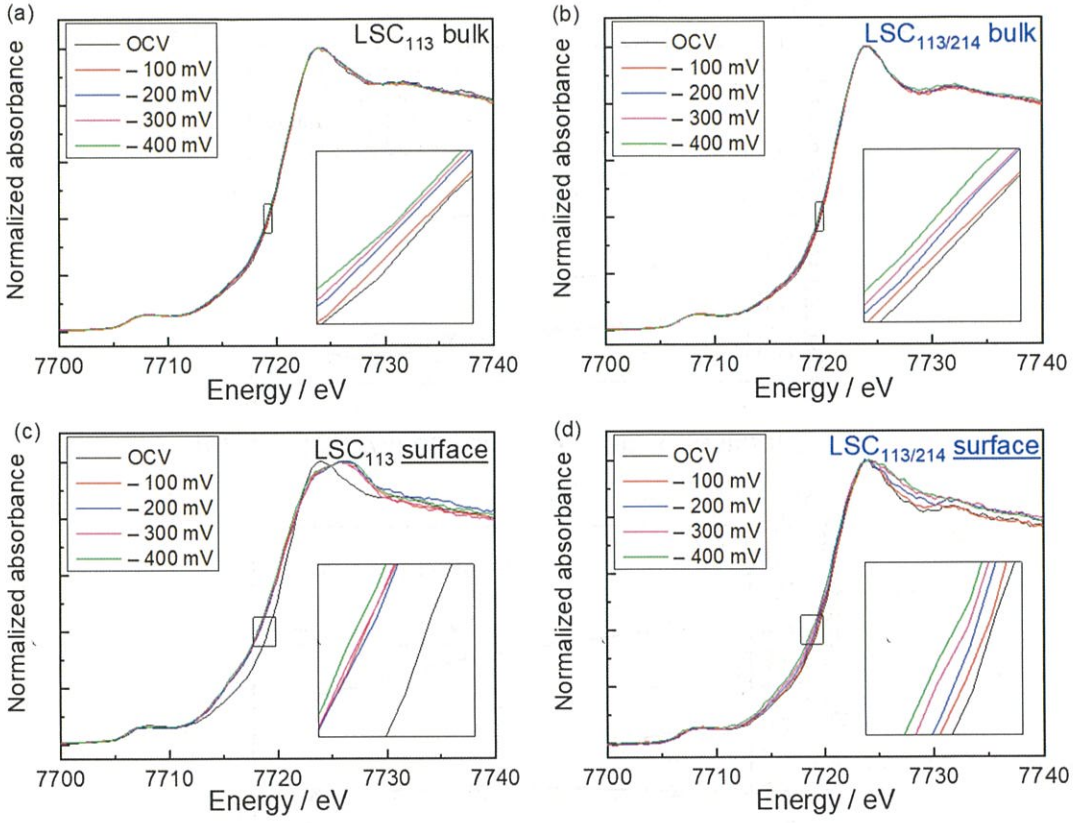

Figure 5.4. Co K-edge XANES spectra from *operando* TRF-XAS for (a, c) LSC_{113} and (b, d) $LSC_{113/214}$, measured under cathodic polarization at 773 K and $p(O_2)$ of 10^5 Pa. (a, b) Bulk information from the standard fluorescence XAS and (c, d) surface information under the TRF condition.

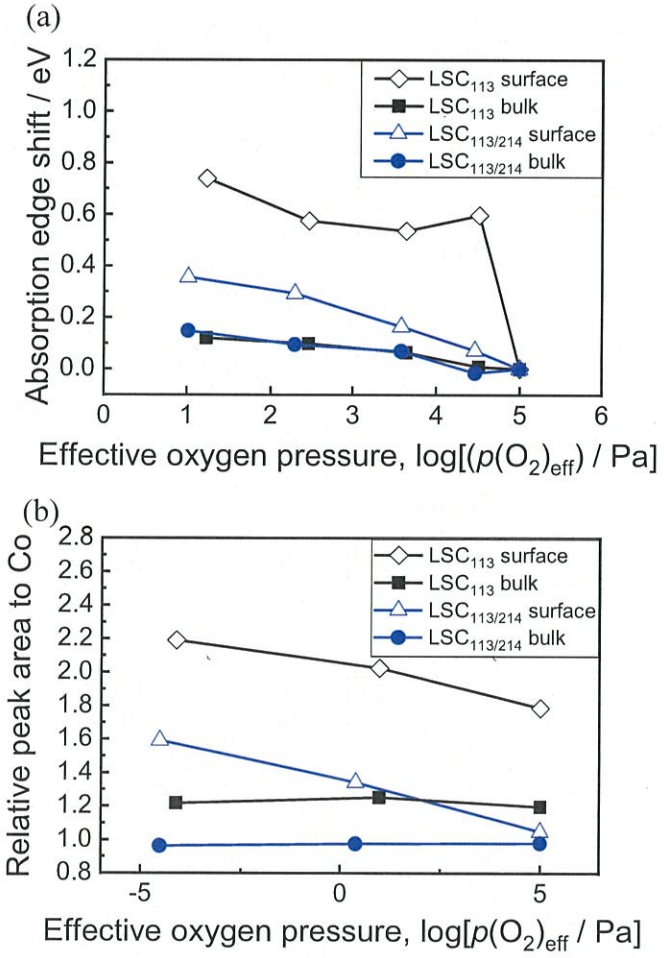

Figure 5.5. (a) Absorption edge shift at the Co K-edge as a function of effective oxygen pa rtial pressure for the *operando* TRF-XAS. (b) Relative peak area changes of Sr-K normalize d by the peak area of Co-K for the *operando* TRF-XR. Open squares denote the shift meas ured under various $p(O_2)$ under OCV. Cross symbols represent the shift measured when appl ying different DC biases at $p(O_2)$ of 10^5 Pa.

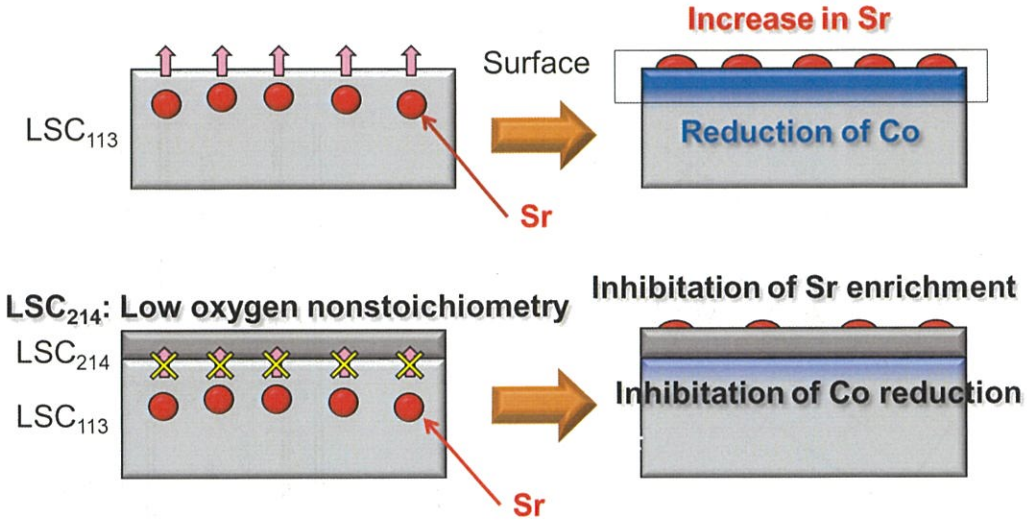

Figure 5.6. Schematic of the surface mechanism of LSC_{113} and $LSC_{113/214}$ cathodic polarization at high temperature.

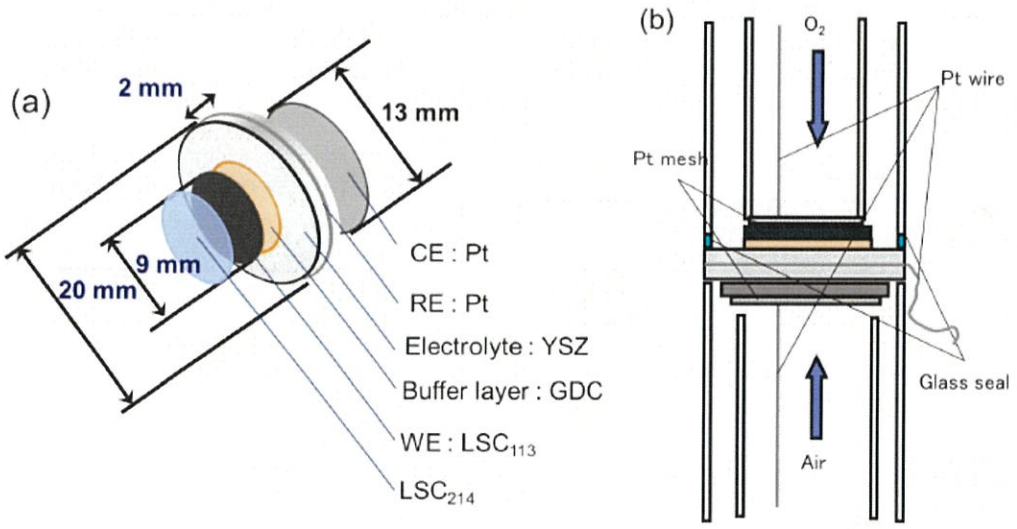

Figure S5.1. Schematic illustration of (a) thin film electrodes and (b) measurement configuration in this study.

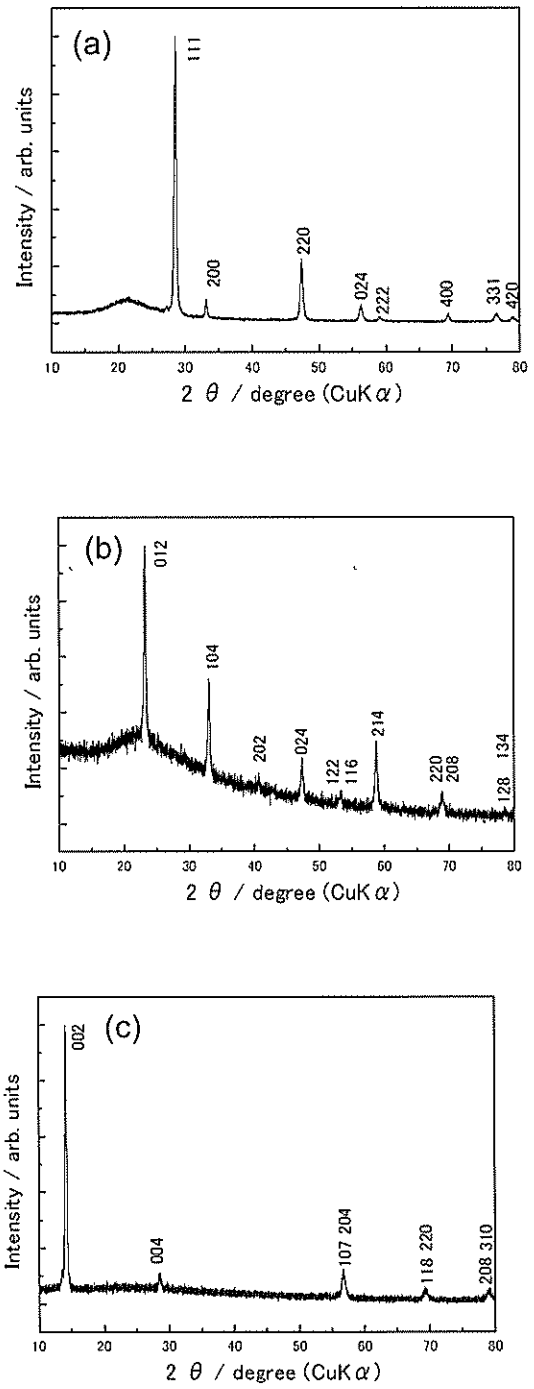

Figure S5.2. XRD patterns of the (a) GDC (gadolinium doped ceria), (b) LSC_{113} ($La_{0.6}Sr_{0.4}CoO_{3-\delta}$) and (c) LSC_{214} ($(La_{0.5}Sr_{0.5})_2CoO_{4\pm\delta}$) thin film on the mirror polished silica glass.

Table S5.1. The crystal structure of GDC, LSC_{113} and LSC_{214} thin films prepared by PLD method.

Thin film	GDC	LSC_{113}	LSC_{214}
Space group	*Fm3m*	$R\bar{3}c$	*I4/mmm*
Lattice constant	a = 5.415(7) Å	a = 5.48(1) Å c = 13.354(8) Å	a = 3.8033(1) Å c =12.4782(6) Å
Database	a = 5.418 Å [1]	a = 5.452 Å c = 13.257 Å [2]	a = 3.807 Å c = 12.507 Å [3]

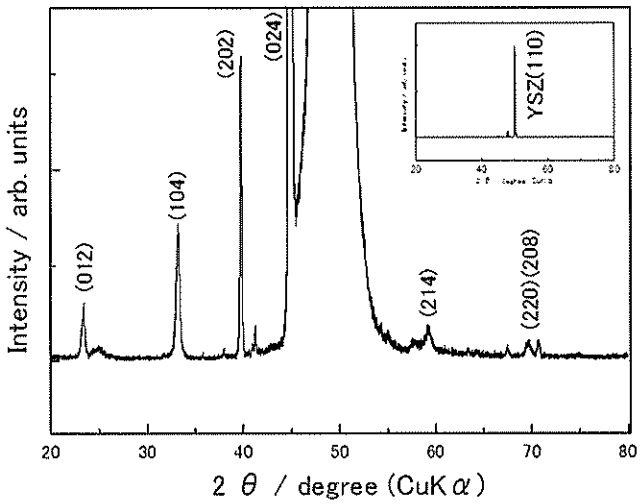

Figure S5.3. XRD pattern of LSC_{113} thin film on YSZ (110) single crystal substrate.

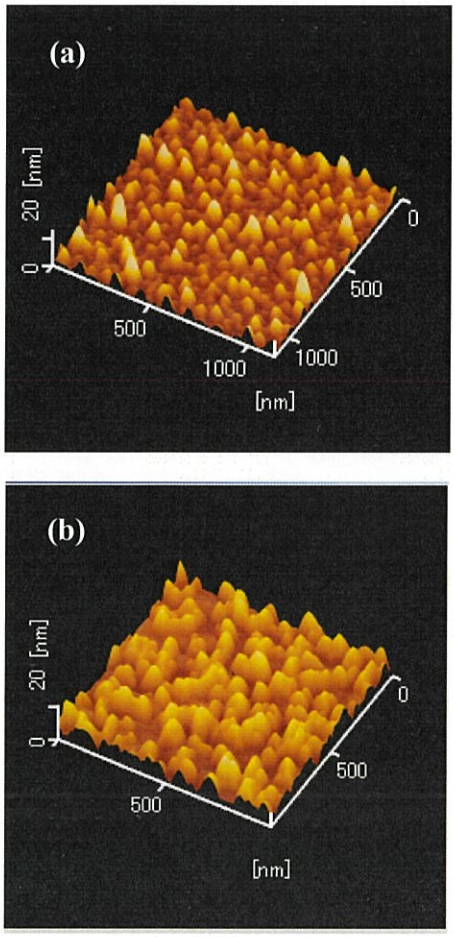

Figure S5.4. AFM image of (a) LSC_{113} and (b) $LSC_{113/214}$ films on YSZ (110). AFM measurements revealed surface RMS roughness of ~1.32 nm and ~3.01 nm, respectively.

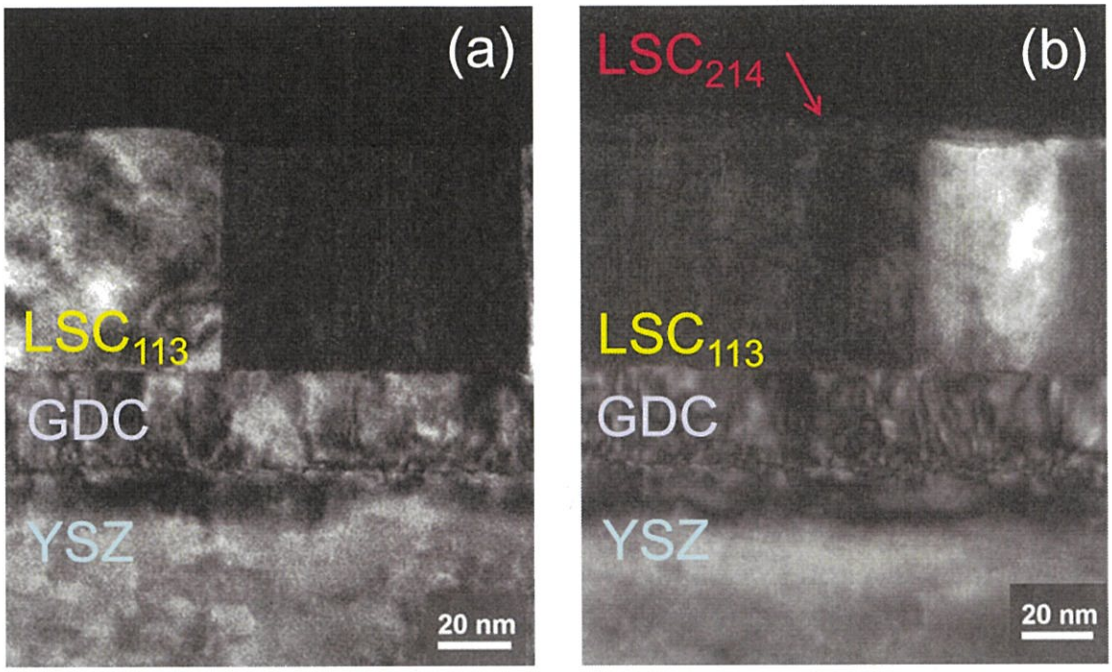

Figure S5.5. Cross-sectional TEM images of (a) LSC_{113} and (b) $LSC_{113/214}$ films on YSZ (110). The thickness of each film is LSC_{113}: 60 nm, GDC: 25 nm and LSC_{214}: 3 nm. The existence of darkness color in LSC_{113} layer suggests that the LSC_{113} films on YSZ (110) single-crystal substrate were poly-crystalline phase.

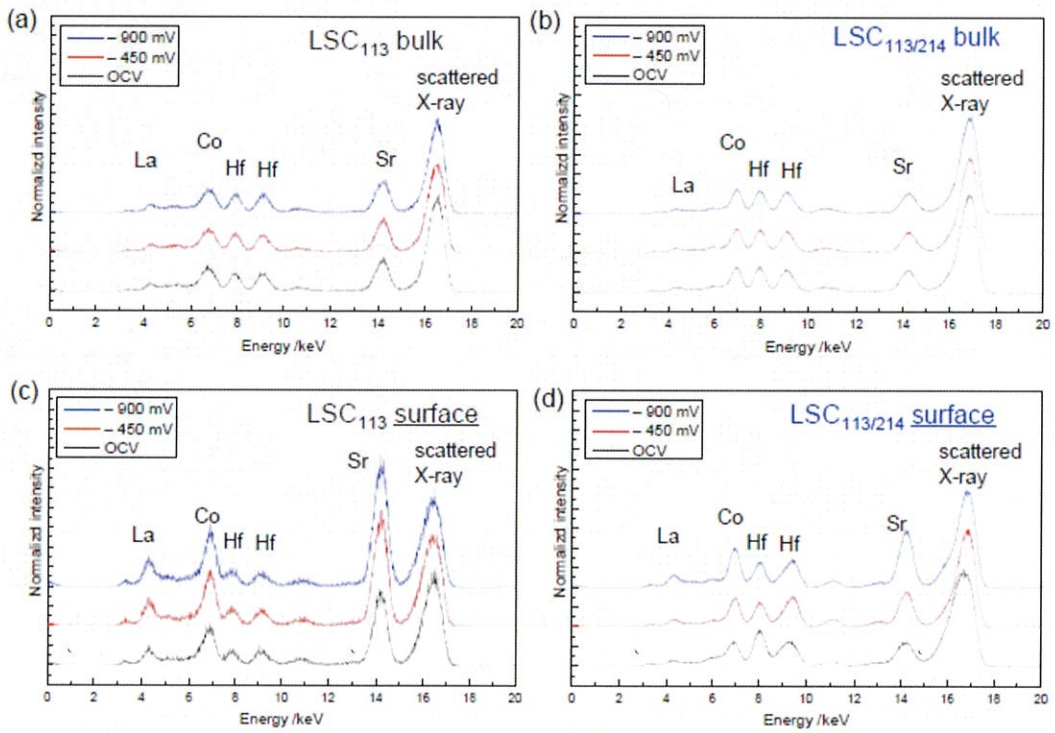

Figure S5.6. X-ray fluorescence spectra of (a, c) LSC_{113} and (b, d) $LSC_{113/214}$ measured at 773 K under cathodic polarization and $p(O_2) = 10^5$ Pa.

References:

[1] G. Brauer, H. Gradinger, Über heterotype Mischphasen bei Seltenerdoxyden. I, *Z. Anorg. Allg. Chem.* **276** (1954) 209-226.

[2] R. Sonntag, S. Neov, V. Kozhukharov, D. Neov, J.E. ten Elshof, Crystal and magnetic structure of substituted lanthanum cobalitites, *Physica B: Condensed Matter* **241-243** (1997) 393-396.

[3] M. James, A. Tedesco, D. Cassidy, M. Colella, P.J. Smythe, The phase diagram and crystal chemistry of strontium-doped rare earth cobaltates: Ln2−xSrxCoO4+δ (Ln=La–Dy), *J. Alloys Compd.* **419** (2006) 201-207.

Chapter 6. General Conclusion

In this work, we studied a new film formation process that realizes thinner electrolyte membranes for higher efficiency solid oxide fuel cells. In addition, we developed an in-situ analysis method for the chemistry and electronic states of electrode materials to analyze the cathode reaction mechanism and investigated the relationship between surface state changes and electrode activity in various cathode materials.

Chapters 2 and 3 focused on YSZ as the SOFC electrolyte and studied new thin film preparation process to reduce the IR loss of the electrolyte.

In Chapter 2, we verified the electrolysis process in the gas phase, which is a new thin film fabrication process. This process differs from other vapor deposition methods in that a DC bias circuit separate from the plasma generation circuit is used for the electrodeposition process. The YSZ layer was electrodeposited from $ZrCl_4$ and YCl_3 on a non-porous calcia stabilized zirconia substrate. Scanning electron microscopy, electron probe microanalysis, electron spectroscopy for chemical analysis, and X-ray diffraction measurements confirmed the electrodeposition of a smooth, pinhole-free yttria-stabilized zirconia film with a thickness of about 3 μm. From this, the possibility of thin film preparation by vapor phase electrolysis was shown.

In Chapter 3, we analyzed the deposition process of YSZ thin film by the vapor phase electrolysis method established in Chapter 2.

The deposition rate by vapor phase electrolysis was 7 μm / h at 1100 ° C, about 4 times faster than the CVD-EVD process under the same conditions. YSZ thin films prepared by vapor phase electrolysis was pinhole-free, and their ionic conductivity was almost the same as that of sintered YSZ.

In Chapter 4, a noble in situ analytical technique, which enables us x-ray absorption spectroscopy measurements at elevated temperature while controlling atmospheric conditions and passing electrical current, was developed, and was applied to investigate the cathodic reaction for solid oxide fuel cells (SOFCs). Dense thin-film electrodes of $La_{0.6}Sr_{0.4}CoO_{3-\delta}$ (LSC) on a $Ce_{0.9}Gd_{0.1}O_{1.95}$ (GDC) electrolyte, $La_{0.9}Sr_{0.1}MnO_{3\pm\delta}$ (LSM) on a $Zr_{0.92}Y_{0.08}O_{1.96}$ (YSZ) electrolyte, and $La_{0.6}Sr_{0.4}Co_{0.8}Fe_{0.2}O_{3-\delta}$ (LSCF) on $Y_{0.1}Ce_{0.9}O_{1.95}$ (YDC) electrolyte were chosen as model SOFC cathodes in this study. Variations in oxygen chemical potential in the electrode with and without cathodic polarization could be experimentally evaluated from the energy shift of the transition metal K-edge absorption such as Co, Fe and Mn. In the case of LSC and LSCF, it was found that the oxygen chemical potential in the electrode was reduced by applying the cathodic potential and that such a change in oxygen chemical potential was occurred mainly at the electrode surface. This directly demonstrated that the electrochemical oxygen reduction on the cathode is rate-controlled by surface reactions. On the other hand, LSM showed oxygen potential change in electrode / gas interface and the rate-determining step of the lanthanum strontium manganite / YSZ model electrode is the diffusion reaction in the electrode.

This study reveals the rate determining step of electrode reaction for SOFC spectroscopically for the first time.

In Chapter 5, a noble in situ analytical technique, which enables us x-ray absorption spectroscopy measurements at elevated temperature while controlling atmospheric conditions and passing electrical current, was developed, and was applied to investigate the cathodic reaction for solid oxide fuel cells (SOFCs). Dense thin-film electrodes of $La_{0.6}Sr_{0.4}CoO_3$ (LSC_{113}) on a $Zr_{0.92}Y_{0.08}O_{1.96}$ (YSZ) electrolyte was chosen as model SOFC cathodes in this study. In situ TRF-XAS, XRF measurement showed the change of electronic structure (the reduction of Co ions) and Sr enrichment at the surface of LSC_{113} thin film under operating conditions of SOFCs, while the changes of the bulk were not similar. The decorating $(La_{0.5}Sr_{0.5})_2CoO_4$ (LSC_{214}) with LSC_{113} causes the enhancement of ORR activity. $LSC_{113/214}$ thin film which shows higher ORR activity than LSC_{113} prevented the change of surface electronic structure and Sr enrichment.

List of Publications

Chapter 2

Zempachi Ogumi, Yoshiharu Uchimoto, Yoichiro Tsuji, and Zen-ichiro Takehara

"Electrodeposition of thin yttria-stabilized zirconia layers using glow-discharge plasma"

Journal of Applied Physics, Volume 72, Issue 4, pp 1577-1582 (1992)

Chapter 3

Zempachi Ogumi, Yoshiharu Uchimoto, Yoichiro Tsuji and Zen-ichiro Takehara

"Preparation of thin yttria-stabilized zirconia films by vapor-phase electrolytic deposition"

Solid State ionics, Volume 58, Issue 3-4, pp 345-350 (1992)

Chapter 4

Yoichiro Tsuji, Koji Amezawa, Takayuki Nakao, Toshiaki Ina, Tatsuya Kawada, Kentaro Yamamoto, Yoshiharu Uchimoto, Yuki Orikasa

"Investigation of Cathodic Reaction Mechanism in Solid Oxide Fuel Cells by Operando X-Ray Absorption Spectroscopy"

Electrochemistry, Volume 88, Issue 6, pp 1-6 (2020)

Chapter 5

Yoichiro Tsuji, Shinnosuke Sako, Kiyofumi Nitta, Kentaro Yamamoto, Yang Shao-horn, Yoshiharu Uchimoto, and Yuki Orikasa

"Surface Analysis of Lanthanum Strontium Cobalt Oxides under Cathodic Polarization at High Temperature through Operando Total-reflection X-ray Absorption and X-ray Fluorescence Spectroscopy"

Solid State Ionics, printing Volume 357 (2020)

Acknowledgment

The study on this thesis has been carried out at Graduate School of Human and Environmental Studies, Kyoto University.

First of all, I would like to wish to express my special gratitude to Professor Yoshiharu Uchimoto at Graduate School of Human and Environmental Studies, Kyoto University, for his precise indications and valuable advices. I am also grateful to Associate Professor Yuki Orikasa at Graduate School of College of Life Sciences Department of Applied Chemistry, Ritsumeikan University, for his kind instructions and many meaningful advices.

I would like to express deep gratitude to Professor Zen-ichiro Takehara at Kyoto University, Professor Zempachi Ogumi at Kyoto University and Professor Koji Amezawa at Graduate School of Environmental Studies, Tohoku University, for their effective suggestions and helpful advices.

I would like to express special gratitude to Assistant Professor Kentaro Yamamoto and Assistant Professor Tomoki Uchiyama at Graduate School of Human and Environmental Studies, Kyoto University, for their valuable advices.

I would like to thank to all the members of Professor Uchimoto's laboratory for their helps, discussions and encouragement throughout this study.

Finally, I would like to appreciate my families for their understanding, support, and encouragement.

Kyoto, Japan, 2020 Yoichiro Tsuji

著作権等